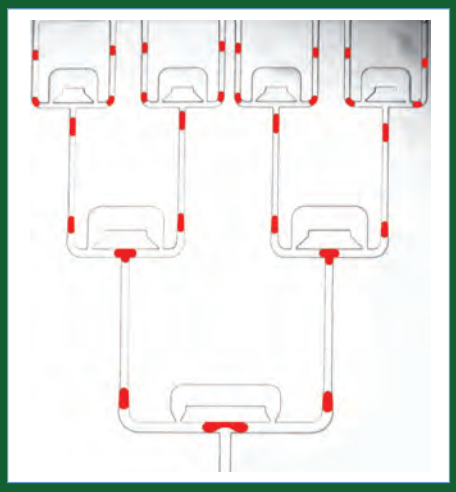

Duong Anh Hoang

Breakup of confined droplets in microfluidics

Duong Anh HOANG

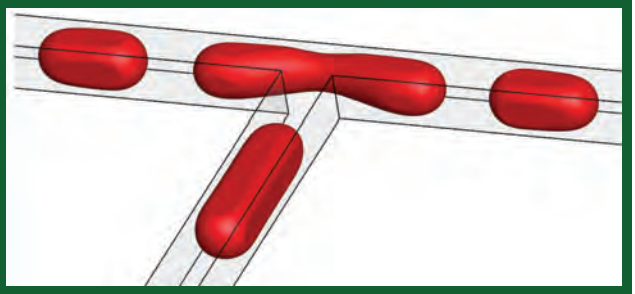

Breakup of confined droplets in microfluidics

ISBN 978-94-6186-225-9

Breakup of confined droplets in microfluidics

PROEFSCHRIFT

ter verkrijging van de graad van doctor
aan de Technische Universtiteit Delft,
op gezag van de Rector Magnificus prof. ir. K.C.A.M. Luyben,
voorzitter van het College van Promoties,
in het openbaar te verdedigen op
woensdag, 16 oktober 2013, om 10:00 uur
door

Duong Anh HOANG

Master of Engineering
van Gyeongsang National University, Zuid-Korea
geboren te Quang Tri, Vietnam

Dit proefschrift is goedgekeurd door de promotoren:
Prof. dr. ir. C.R. Kleijn
Prof. dr. ir. M.T. Kreutzer

Samenstelling promotiecommissie:

Rector Magnificus	voorzitter
Prof. dr. ir. C.R. Kleijn	Technische Universiteit Delft, promotor
Prof. dr. ir. M.T. Kreutzer	Technische Universiteit Delft, promotor
Prof. dr. ir. J. Westerweel	Technische Universiteit Delft
Prof. dr. ir. C. Vuik	Technische Universiteit Delft
Prof. dr. ir. J.M.J. den Toonder	Technische Universiteit Eindhoven
Prof. dr. ir. C.G.P.H. Schroën	Wageningen University
Dr. ir. J.H. Snoeijer	Universiteit Twente

Dr. Ir. Volkert van Steijn en Dr. Eng. Luis M. Portela hebben in belangrijke mate aan de totstandkoming van dit proefschrift bijgedragen.

This work was carried out within the context of the DeMIR (Design of Micro/Milli-Reactors for Large Scale Processing) project which is funded by the Dutch Technology Foundation (STW) and the Industrial Advisory Board (IROP) of the Netherlands Research School in Process Technology (OSPT).

Printed by: Sieca Repro

ISBN 978-94-6186-225-9

Author email: haduong83@gmail.com

To vo iu, mom, dad and sister

Contents

Summary

Segmented-flow microreactors have emerged as an attractive tool for fine chemical synthesis and (bio)chemical analysis, owing to their high heat and mass transfer rate, low axial dispersion, as well as rapid mixing. A key challenge for the use of segmented-flow microreactors in large-scale processing is their low throughput. This can be overcome by applying the concept of numbering-up in which several microreactors are placed and operated in parallel. A challenging aspect of this approach is to distribute segmented flows over those parallel microreactors with a high uniformity in the size and the speed of the fluid compartments. In this thesis, we propose to use a bubble-splitting distributor where a single stream of fluid compartments is recursively split into smaller ones via a series of T-junctions.

The design of the bubble-splitting distributor requires a thorough understanding of and a mechanistic insight into the breakup phenomena. We used Computational Fluid Dynamics (CFD) as a primary tool to study the breakup behavior, as it can provide detailed temporally and spatially resolved information on the flow. To model the fluid interface, we employed the Volume of Fluid (VOF) method, as implemented in the open-source CFD package OpenFOAM-1.6. An extensive analysis of the accuracy and efficiency of the employed VOF method, along with three test cases, validated by experiments, form a rigorous set of benchmarks for the ability of the employed CFD code to model segmented microflows. Based on this analysis, we propose optimal numerical settings, allowing for the dynamical behavior of droplets to be predicted in excellent agreement with experiments.

We then present a numerical study on the breakup of confined droplets in a T-junction, using the validated VOF code. Our simulations revealed that there are two distinct phases during the breakup process: (i) a quasi-steady deformation owing to the external flow, and (ii) a rapid pinching driven by surface tension. With stop-flow simulations, we found that once the droplet enters the rapid pinching phase, the breakup is inevitable and will continue even if the external driving force is removed. Analogously to unconfined droplets, the autonomous pinching of confined droplets starts when, in the channel mid-plane, the curvature at the neck is larger than the curvature

everywhere else. The difference in the curvature along the droplet surface creates a flow reversal towards the neck, which accelerates the pinching rate. The onset of the rapid pinching depends strongly on the aspect ratio of the channel and slightly on the capillary number and the viscosity ratio.

Being able to explain the mechanism of the droplet breakup leads us to another important question, *i.e.* whether the droplet breaks or not. In agreement with earlier findings in literature, we observed numerically and experimentally that there exists a critical capillary number below which the droplet does not break but, due to perturbations which result from asymmetries in the flow and geometry, drifts away into one branch of the T-junction. The competition between two timescales, viz. those for breaking and drifting, determines this critical condition. In this thesis, we presented an extensive analysis of the dynamical behavior of the droplet approaching the critical condition and the variation of these two timescales. In zero-perturbation simulations, we found that the breakup time increases towards infinity as the capillary number decreases towards the critical value. For the drifting, we identified three phases during the drifting: a first phase in which the displacement of the droplet grows exponentially in time, a transition phase, and a phase in which the droplet moves with the bulk liquid velocity. The drifting time is controlled mainly by the first phase and depends linearly on the capillary number. Owing to the drifting, the critical capillary number may increase by more than 10% compared to the critical capillary number obtained in the zero-perturbation system. Moreover, we found that symmetric breakup can only be obtained when the breakup time is at least approximately two times smaller than the drifting time.

The last part of this thesis describes the design strategies for and characterization of a bubble-splitting distributor based on our understanding of the fundamental physics of the breakup behavior. We present theoretical and experimental analyses of the uniformity of the distribution of bubbles/droplets using the proposed distributor for different flow conditions. We identified three primary sources of the nonuniformity: (i) nonuniformity in the size of bubbles fed to the distributor, (ii) the presence of non-breaking bubbles, and (iii) asymmetric bubble breakup. We formulated two guidelines to operate the bubble-splitting distributor: (i) the operating capillary number should be well above its a critical value at all junctions to ensure that all bubbles break, and (ii) the distance between the bubbles should be sufficiently large to ensure that all bubbles break symmetrically. Furthermore, we found that a pressure equalizer applied between two branches of the T-junction is beneficial, only when the fabrication tolerances of the device are large.

The thesis ends with a discussion on how some of our main findings can be generalized: 1) surface-tension-driven pinching, 2) differences between 2D and 3D breakup, 3) the role of CFD in unraveling the breakup phenomena and 4) scale-up of segmented flow microreactors. We then conclude the thesis by proposing some opportunities for future research.

Samenvatting

"Segmented-flow" microreactors zijn uitgegroeid tot een aantrekkelijke methode voor fijn-chemische synthese en (bio)chemische analyse. Dit is te te danken aan de hoge warmte- en massatransportsnelheden, lage axiale dispersie en snelle menging. Een belangrijke uitdaging voor het gebruik van de "segmented-flow" microreactors voor processen op grote schaal is dat de productiesnelheid laag ligt. Dit kan opgevangen worden via het concept van uitschalen, waarbij verschillende microreactoren parallel toegepast worden. In het uitschalen is het van groot belang om de vloeistof-compartimenten met gelijke snelheid en grootte over alle parallele microreactoren te verdelen. In dit proefschrift hebben we een verdeler toegepast die een enkele stroom van vloeistof- en gascompartimenten in steeds kleinere compartimenten opsplitst door middel van een serie T-splitsingen.

Het ontwerp van de verdeler vereist een gedetailleerd begrip van het mechanisme voor het opbreken van de compartimenten. We hebben hoofdzakelijk "Computational Fluid Dynamics" (CFD) gebruikt om het opbreekgedrag te bestuderen, omdat CFD een hoge mate van detail geeft, zoveel ruimtelijk als in de tijd. Voor het modelleren van het vloeistofoppervlak hebben we de "Volume of Fluid" (VOF) methode toegepast die standaard beschikbaar is in het CFD-pakket OpenFOAM-1.6. Een uitgebreide analyse van de nauwkeurigheid en efficiëntie van de gebruikte VOF methode, in combinatie met drie testcases, allen gevalideerd met experimenten en experimenteel gevalideerde modellen, vormen een betrouwbare set van ijkpunten voor het vermogen van de CFD code om segmented microstromingen te modelleren. Op basis van deze analyse hebben we de optimale numerieke instellingen geselecteerd en daarmee het dynamische gedrag van de druppel voorspeld, in uitstekende overeenstemming met experimenten.

Vervolgens hebben we een numerieke studie van het opbreken van druppels in een T-splitsing uitgevoerd met de gevalideerde VOF code. Onze simulaties tonen aan dat er twee fasen te onderscheiden zijn in het opbreekproces: (i) een quasi-constante vervorming door de externe stroming, en (ii) een snelle insnoering veroorzaakt door de oppervlaktespanning. Met "stop-flow" simulaties hebben we uitgevonden dat zodra de snelle insnoering begonnen is, het opbreken onvermijdelijk wordt en vóórtduurt

zelfs nadat de externe drijvende kracht is weggenomen. Analoog met druppels in een oneindig medium, begint het insnoeren van de druppels in een microkanaal zodra, in het midden van het kanaal, de kromming van de nek groter wordt dan de kromming op andere plaatsen. Het verschil in kroming over het druppeloppervlak zorgt voor een omkering van de stroming in de richting van de nek, waardoor het insnoeren versnelt. Het moment van de snelle insnoering hangt sterk af van de aspectratio van het kanaal en is zwak afhankelijk van het capillairgetal en de viscositeitsratio.

Uit het begrip van het mechanisme voor het opbreken van druppels volgt een andere belangrijke vraag, namelijk óf de druppel zal breken of niet. Experimenteel en numeriek hebben we vastgesteld dat er een kritisch capillairgetal bestaat waaronder een druppel niet opbreekt maar wegdrijft in één van de benen van de T-splitsing onder invloed van stromingsperturbaties ten gevolge van asymmetrieën in de stroming en de geometrie. De competitie tussen twee tijdschalen, opbreken en wegdrijven, bepaalt de kritische conditie. In dit proefschrift presenteren we een uitgebreide analyse van het dynamisch gedrag van de druppel en de variatie van de twee tijdschalen als de druppel de kritische conditie nadert. Met verstoringsvrije simulaties vinden we dat de opbreektijd naar oneindig gaat als het capillairgetal de kritische waarde nadert. Voor het wegdrijven identificeren we drie fasen: een eerste fase waarin de verplaatsing van de druppel exponentieel toe neemt in de tijd, een overgangsfase, en een fase waarin de druppel beweegt met de snelheid van de bulkvloeistof. De wegdrijftijd wordt met name bepaald door de eerste fase en hangt lineair van het capillairgetal af. Door het wegdrijven neemt het kritische capillairgetal met meer dan 10% toe ten opzichte van het kritische getal in systemen zonder verstoring. Bovendien vinden we dat het symmetrisch opbreken van de druppel alleen mogelijk is als de opbreektijd minimaal ongeveer twee keer kleiner is dan de wegdrijftijd.

Het laatste deel van dit proefschrift beschrijft een ontwerpstrategie voor en de analyse van een verdeler gebaseerd op ons begrip van de fundamentele fysica van het opbreekgedrag. We presenteren theoretische en experimentele analyses van de gelijkmatigheid van de verdeling van bellen/druppels in de voorgestelde verdeler bij verschillende stromingscondities. We identificeren drie primaire oorzaken voor ongelijkmatigheid: (i) ongelijkmatigheid in het formaat van de druppels die de verdeler ingevoerd worden, (ii) bellen die niet opbreken, en (iii) asymmetrisch opbreken van bellen. We hebben twee aanbevelingen geformuleerd voor het gebruik van de verdeler: (i) het capillairgetal tijdens gebruik moet groter zijn dan de kritische waarde bij alle splitsingen om verzekerd te zijn van opbreken, en (ii) de afstand tussen de bellen moet voldoende groot zijn om alle bellen symmetrisch op te laten breken. Verder hebben we gevonden dat het toepassen van een passieve drukregeling tussen de twee benen van de T-splitsing alleen nuttig is als de fabricagetoleranties van het apparaat groot zijn.

Dit proefschrift eindigt met een discussie van de meer algemene toepasbaarheid van onze belangrijkste bevindingen: 1) oppervlaktespanning gedreven insnoeren, 2) 3D

versus 2D, 3) de rol van CFD in het bestuderen van de opbreekverschijnselen en 4) het opschalen van “segmented flow"microreactoren. We sluiten het hoofdstuk af met een voorstel voor toekomstig onderzoek.

1. Introduction

1.1 Microfluidics

Microfluidics is the field of science and technology that deals with the control and manipulation of fluids in channels with typical dimensions of tens to hundreds of micrometers [1,2]. One of the ideas behind having such small length scales is to increase the surface-area-to-volume ratio. As a consequence, high heat and mass transfer rates can be achieved in microfluidic systems, leading to many applications in micro-reactor technology [3–5]. Scaling down volumes and channel sizes also allows small sample volumes, thus cost-effective and low-risk analysis that can provide high-throughput screening in drug discovery [6–8], biotechnology [9,10] and chemical analysis [11,12].

In a microfluidic device, such as the one depicted in figure 1.1(a), fluids typically flow at low Reynolds number, Re, defined as the ratio between the inertial forces and the viscous forces ($Re = \rho d U/\mu$, where ρ is the fluid density, d the dimension of the channel, U the fluid velocity and μ the viscosity). Single-phase flow in this regime is laminar and has a parabolic velocity profile with zero velocity at the walls. This leads to some undesired effects. First, mixing is solely due to molecular diffusion, which is a rather slow process [12]. Second, there is much dispersion along the channel, leading to wide residence time distribution [13].

1.2 Droplet microfluidics

A simple way to reduce axial dispersion and enhance mixing in microfluidic systems is to introduce a second, immiscible fluid that compartmentalizes the flow [14]. The bubbles or droplets in such a segmented flow [15] almost span the cross section of the microchannels as shown in figure 1.1(b). Consequently, reagents are confined inside the compartments with limited or no exchange between the different compartments [16,17]. Besides the reduction in axial dispersion, the presence of bubbles or droplets induces a circular flow pattern both inside and outside the bubbles or droplets, resulting in rapid mixing [18,19]. Due to these advantages, droplet microfluidics has appeared in several applications, such as lab-on-a-chip [20–22], chemical synthesis, and high-throughput screening [23–25].

A key remaining challenge for the use of segmented-flow microfluidic systems in production of chemicals is to increase the production rate.

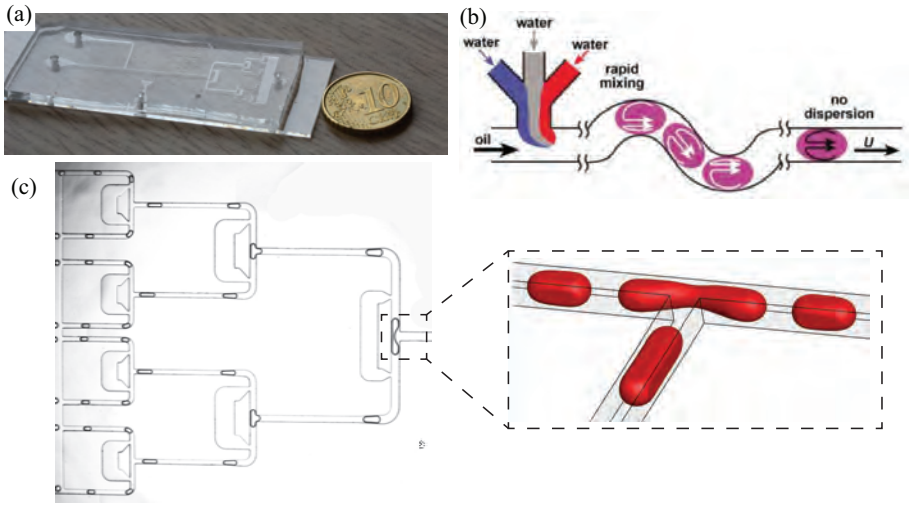

Figure 1.1 (a) Illustration of a microfluidic device. (b) Schematic of droplet microfluidics [11]. (c) Illustration of a bubble-splitting distributor and an enlarged view of the breakup process in a single T-junction.

1.3 Context of PhD work: Droplet microfluidics in commercial-scale processing

The research presented in this thesis is part of a project funded by the Dutch Technology Foundation (STW) and the Industrial Advisory Board (IROP) of the Netherlands Research School in Process Technology (OSPT) under the name: "Design of Micro/Milli-Reactors for Large Scale Processing" - DeMiR. The project aims for the development of a generic methodology to select and design the best scale of reactor operation, either at the micro-scale or at the milli-scale, in case of G/L and L/L catalytic reactions and multiphase food processing systems.

An important part in this project is to scale-up the production rate of multiphase micro/milli reactors. This can be achieved through the concept of numbering-up, in which several production units are placed and operated in parallel. An important advantage of this approach is that it avoids scale-up/scale-down issues, because the characteristics of the designed system do not change when the production increases.

A challenging aspect of the DeMiR project is to develop a robust method to distribute segmented flow over a network of parallel microchannels, with a high uniformity in the size of the compartments to avoid differences in the reaction rate as well as heat and mass transfer among production units. Previous attempts have been carried out to uni-

formly and stably distribute bubbles/droplets over a network of microchannels[26–31]. One approach is to produce droplets or bubbles in each individual channel[26–28]. This approach requires an identical supply of each phase to all these channels and a minimum cross-talk between the channels. These requirements can be satisfied by using resistive channels, which should roughly have a two orders of larger flow resistance than the reaction channels[26,27]. This works out to long ultra-small channels and the need of highly precise fabrication. An alternative approach studied in this thesis is to feed segmented flow into a microfluidic device and recursively split the bubbles or droplets into smaller ones[29–31]. Figure 1.1(c) shows an example of such a distributor. To understand how to distribute the bubbles or droplets equally over the downstream channels of such a distributor requires a deep understanding of the breakup of bubbles and droplets in microfluidic devices.

1.4 Bubble/droplet breakup

In comparison with continuous single-phase flow microfluidics, the physical behavior of droplet microfluidics is more complicated due to the presence of the fluid-fluid interface. Interfacial forces, which are proportional to the surface tension coefficient γ and the curvature κ of the interface, play an important role due to the small scale of the system. Important dimensionless numbers are the Reynolds number *Re*, the capillary number $Ca = \mu U/\gamma$ (i.e. the ratio between capillary and viscous time scales), the Weber number $We = Re\ Ca = \rho d U/\gamma$ (i.e. the ratio between capillary and inertial time scales) and the Bond number $Bo = \rho g d^2/\gamma$ (i.e. the ratio between inertial and capillary time scales). The fluid flow in droplet microfluidics is characterized by low Reynolds, capillary and Weber numbers. For example, in a channel with height $100\,\mu\mathrm{m}$, a flow of oil-water system ($\mu \sim 1\,\mathrm{mPa\,s}$, $\gamma \sim 10\,\mathrm{mN/m}$ and $\rho \sim 1000\,\mathrm{g/l}$) at a typical velocity of $1\,\mathrm{cm/s}$ has a Reynolds number of unity, a capillary number of 10^{-3}, a Weber number of 10^{-3} and a Bond number of 10^{-2}. Under such conditions, interfacial forces are much larger than viscous, inertial and gravitational forces.

The breakup of bubbles/droplets can occur under unconfined and confined geometric conditions, meaning that the fluid vessel is either large or comparable to the size of the bubbles/droplets. In both cases, a droplet experiences an external flow that deforms the droplet and finally breaks it apart. The fundamental difference between the two is that the shape of the unconfined droplet is a function of the strength of the external flow and its properties, while, besides the above factors, the shape of the confined droplet also strongly depends on the channel geometry.

Pioneering work on unconfined breakup was done in the early 1930's by Taylor[32], who showed that a droplet under steady extensional flow is stretched through a series of steady shapes until reaching maximum steady deformation below which the droplet deforms continuously until it breaks. There exists a critical capillary number

Ca, which corresponds to the critical length of the droplet. This critical capillary number depends only on the viscosity contrast $\lambda = \hat{\mu}/\mu$ of the fluids inside and outside the droplet. Stone et al.[33] experimentally reported a second critical droplet length, beyond which the droplets break autonomously, and below which droplets relax back to their equilibrium shape. These major accomplishments of Taylor[32] and Stone et al.[33] have inspired several subsequent studies on the breakup of unconfined droplets both numerically and experimentally[34–38].

Literature on confined breakup starts quite later, in the early 2000's, with the pioneering work by Link et al.[29]. They demonstrated that in confined breakup, there is also a critical droplet length, corresponding to a critical capillary number *Ca*. In confined flow, the channel geometries play an important role such that the boundary between breaking and non-breaking regimes depends not only on λ and *Ca* but also on the ratio between droplet length and channel width l/w. Link et al.[29] used stability arguments to predict this transition. More in the spirit of Taylor's analysis[32], Leshansky and Pismen[39] predicted the transition by calculating critical pseudo-steady droplet shapes using a two-dimensional model in which the capillary instability is not operative. Their theory successfully predicts, up to an $O(1)$ constant, whether droplets break. Subsequent experiments[40–42] have been carried out to construct the transition line between breaking and non-breaking regimes (i.e. the critical capillary number as a function of l/w), but none of them could provide a clear description on the mechanisms governing the dynamics of the droplet during breakup process.

1.5 The role of computational fluid dynamics (CFD) in the design process

Computational fluid dynamics is a branch of fluid mechanics that applies numerical methods and algorithms to solve the equations of fluid dynamics on digital computers. With the development of high performance computing, CFD has played an important role in the design process of flow systems in e.g. aeronautical, automotive, and chemical industries. With CFD, it is easy to vary the characteristics of the systems such as fluid properties, channel geometries and flow conditions, thus allowing broad parametric variations. This is important in the design process as it can provide a cheap and fast way to design and optimize the system. More importantly, CFD can provide detailed temporal and spatial flow information that is crucial to gain insights into the nature and underlying mechanisms of the flows. For droplet microfluidics, CFD allows to simultaneously extract both local and global information on three-dimensional shapes of the fluid interface and the flow variation. Moreover, experiments such as stop-flow experiments[33] and perturbation-free experiments, which are useful for the understanding of the flow behavior but difficult to perform physically in confined microfluidic systems, can be numerically performed without much effort. Hence, a complete picture of the

dynamical behavior of flows in microfluidic systems obtained with CFD simulations is very useful in revealing the fundamental understanding of the flows.

Various numerical methods has been proposed and used to model flows in droplet microfluidic systems [43–45], each having its own advantages and disadvantages. Therefore, a careful selection of numerical methods to be applied is crucial. An optimized computational setting can provide a big improvement, sometimes up to a hundred percent, in accuracy and efficiency of the numerical simulations.

1.6 Research questions

In this thesis, we present our work on the breakup of bubbles/droplets in microfluidic systems. We first report our findings on the fundamental physics of the splitting phenomena using three-dimensional CFD simulations. We then present the strategy to design a bubble-splitting distributor and its performance under different operating conditions.

1.6.1 Mechanistic insights of confined bubble/droplet breakup

The mechanism of the breakup of confined bubbles and droplets is currently debated in literature. There are two fundamentally different hypotheses on how a droplet breaks in a microchannel. The first one stated that the breakup of confined droplets is governed by a Rayleigh-Plateau-type instability [29]. In the second hypothesis, the droplet deforms through a set of pseudo-steady shapes that result from a balance of viscous and interfacial forces during the breakup process, and the Rayleigh-Plateau instability does not happen due to the confinement [39]. This motivated us to address a question *"What is the driving mechanism of the breakup of confined bubbles and droplets?"*.

Unraveling the mechanism of confined droplet breakup led us to another question associated with the previous one *"What is the relation between the breakup boundary and the timescales for breakup and drifting?"*. Available experiments showed that close to the boundary between breaking and non-breaking regimes, a droplet can either break or drift away under the same flow conditions [29,40,41]. Close to the this boundary, asymmetric breakup is observed even in a symmetric T-junction [42,46]. Studying the above question teaches us how, close to the breakup boundary, the time scale for breakup and the time scale for drifting become comparable, leading to the transition from breaking to non-breaking.

1.6.2 Bubble-splitting distributor

The technical motivation of this thesis is to design a bubble/droplet distributor that evenly distributes a segmented two-phase flow over a network of microreactors for commercial-scale processing. This can be achieved by splitting a single stream of bubbles/droplets repetitively in a cascade of such splitters that run into a large number of channels. Literature on this approach is limited to the concept of how to design this type of distributor[29–31]. Based on our understanding on the fundamental physics of the breakup phenomenon, we resolve a question *"How to uniformly distribute bubbles/droplets over a network of microchannels using the bubble-splitting distributor"* by studying the influence of important operational parameters on the uniformity of the final bubble/droplet size.

1.6.3 Optimization of numerical settings and validations

Modeling of bubbles/droplets flowing in microfluidic channels with the Volume of Fluid (VOF) method is well-known for its advantages in handling topological changes, conserving mass and rendering reasonably sharp interfaces[44,45]. However, there are important fine-tuning issues, that are crucial to set right for a successful simulation, when applying the VOF method to bubble/droplet flow in microchannels. They include (1) parasitic currents, (2) resolving the thin film that separates the bubbles/droplets from the channel walls and (3) the breakup of liquid threads. Validations of the VOF method, as implemented in the currently used CFD code OpenFOAM, on bubble/droplet flow are also limited in literature.

In this thesis, we address the question *"Can the VOF method accurately and efficiently model the dynamical behavior of bubble/droplet interfaces in microfluidic flows and what are the necessary measures to be taken in order to achieve this goal?"*. We resolve this question by presenting well-characterized benchmark cases that allows us to find optimal computational settings to apply the VOF method for the modeling of bubble/droplet breakup in microfluidic channels.

1.7 Outline

This thesis comprises a collection of papers. Each chapter is therefore self-contained, and addresses one of the research questions discussed in the previous section. In chapter 2, we report detailed information and validations of the employed CFD code (OpenFOAM-1.6). With the validated code, addressing the research question formulated in section 1.6.1, we present the mechanistic insights on the pinching of droplets at a T-junction in chapter 3. Chapter 4 is a study on the timescales for breakup and

drifting and how they vary close to the critical condition. This answers the research question from section 1.6.1 on the relation between the breakup boundary and these two timescales. The understanding on the droplet breakup presented in chapter 3 and 4 facilitates us to address the research question formulated in section 1.6.2 and to design a bubble-splitting distributor in chapter 5. We experimentally characterized the designed distributor, and show that uniform flow distribution is obtained for different flow conditions. The last part of this thesis, chapter 6, is a discussion of some of our main findings and their implications in a broader perspective.

Bibliography

[1] H.A. Stone, A.D. Stroock, and A. Ajdari. Engineering flows in small devices. *Annu. Rev. Fluid Mech.*, 36(1):381–411, 2004.

[2] G. M. Whitesides. The origins and the future of microfluidics. *Nature*, 442(7101):368–373, JUL 27 2006.

[3] K. F. Jensen. Microreaction engineering — is small better? *Chem. Eng. Sci.*, 56(2):293 – 303, 2001.

[4] A.I. Stankiewicz and J.A. Moulijn. Process intensification: Transforming chemical engineering. *Chem. Eng. Prog.*, 96(1):22–33, 2000.

[5] V. Hessel, B. Cortese, and M.H.J.M. de Croon. Novel process windows - concept, proposition and evaluation methodology, and intensified superheated processing. *Chem. Eng. Sci.*, 66(7):1426 – 1448, 2011.

[6] B.H. Weigl, R.L. Bardell, and C.R. Cabrera. Lab-on-a-chip for drug development. *Adv. Drug Deliv. Rev.*, 55(3):349–377, 2003.

[7] P.S. Dittrich and A. Manz. Lab-on-a-chip: Microfluidics in drug discovery. *Nat. Rev. Drug Discov.*, 5(3):210–218, 2006.

[8] M. Madou, J. Zoval, G. Jia, H. Kido, J. Kim, and N. Kim. Lab on a CD. *Annu. Rev. Biomed. Eng.*, 8:601–628, 2006.

[9] D. J. Beebe, G. A. Mensing, and G. M. Walker. Physics and applications of microfluidics in biology. *Annu. Rev. Biomed. Eng.*, 4(1):261–286, 2002.

[10] J. El-Ali, P.K. Sorger, and K.F. Jensen. Cells on chips. *Nature*, 442(7101):403–411, 2006.

[11] H. Song, J. D. Tice, and R. F. Isgmagilov. A microfluidic system for controlling reaction networks in time. *Angew. Chem. Int. Edit.*, 42:768–772, 2003.

[12] A. J. deMello. Control and detection of chemical reactions in microfluidic systems. *Nature*, 442 (7101):394–402, JUL 27 2006.

[13] G.I. Taylor. Dispersion of soluble matter in solvent flowing slowly through a tube. *Proc. R. Soc. Lond. A*, 219(1137):186–203, 1953.

[14] A. Günther and K. F. Jensen. Multiphase microfluidics: from flow characteristics to chemical and material synthesis. *Lab Chip*, 6:1487–1503, 2006.

[15] V. S. Ajaev and G.M. Homsy. Modeling shapes and dynamics of confined bubbles. *Annu. Rev. Fluid Mech.*, 38(1):277–307, 2006.

[16] M. T. Kreutzer, A. Gunther, and K. F. Jensen. Sample dispersion for segmented flow in microchannels with rectangular cross section. *Anal. Chem.*, 80(5):1558–67, 2008.

[17] R. Seemann, M. Brinkmann, T. Pfohl, and S. Herminghaus. Droplet based microfluidics. *Rep. Prog. Phys.*, 75:016601, 2012.

[18] J. D. Tice, H. Song, A. D. Lyon, and R. F. Ismagilov. Formation of droplets and mixing in multiphase microfluidics at low values of the reynolds and the capillary numbers. *Langmuir*, 19(22):9127–9133, 2003.

[19] H. Kinoshita, S. Kaneda, T. Fujii, and M. Oshima. Three-dimensional measurement and visualization of internal flow of a moving droplet using confocal micro-piv. *Lab Chip*, 7:338–346, 2007.

[20] M. Prakash and N. Gershenfeld. Microfluidic bubble logic. *Science*, 315(5813):832–5, 2007.

[21] B. T. Kelly, J. C. Baret, V. Talyab, and A. D. Griffiths. Miniaturizing chemistry and biology in microdroplets. *Chem. Commun.*, 18:1773 – 1788, 2007.

[22] S.-Y. Teh, R. Lin, L.-H. Hung, and A. P. Lee. Droplet microfluidics. *Lab Chip*, 8:198 – 220, 2008.

[23] B. Zheng, L. S. Roach, and R. F. Ismagilov. Screening of protein crystallization conditions on a microfluidic chip using nanoliter-size droplets. *J. Am. Chem. Soc.*, 125:11170–11171, 2003.

[24] M. T. Kreutzer, F. Kapteijn, J. A. Moulijn, and J. J. Heiszwolf. Multiphase monolith reactors: Chemical reaction engineering of segmented flow in microchannels. *Chem. Eng. Sci.*, 60(22):5895–5916, 2005.

[25] A. Huebner, S. Sharma, M. Srisa-Art, F. Hollfelder, J. B. Edel, and A. J. Demello. Microdroplets: A sea of applications? *Lab Chip*, 8:1244–1254, 2008.

[26] N. de Mas, A. Günther, T. Kraus, M. A. Schmidt, and K. F. Jensen. Scaled-out multilayer gas-liquid microreactor with integrated velocimetry sensors. *Ind. Eng. Chem. Res.*, 44(24):8997–9013, 2005.

[27] M. Al-Rawashdeh, F. Yu, T. A. Nijhuis, E. V. Rebrov, V. Hessel, and J. C. Schouten. Numbered-up gas-liquid micro/milli channels reactor with modular flow distributor. *Chem. Eng. J.*, 207(SI): 645–655, OCT 1 2012.

[28] T. Nisisako and T. Torii. Microfluidic large-scale integration on a chip for mass production of monodisperse droplets and particles. *Lab Chip*, 8(2):287–93, 2008.

[29] D. Link, S. Anna, D. Weitz, and H. Stone. Geometrically mediated breakup of drops in microfluidic devices. *Phys. Rev. Lett.*, 92(5), 2004.

[30] D. N. Adamson, D. Mustafi, J. X. J. Zhang, B. Zheng, and R. F. Ismagilov. Production of arrays of chemically distinct nanolitre plugs via repeated splitting in microfluidic devices. *Lab Chip*, 6: 1178–1186, 2006.

[31] A. R. Abate and D. A. Weitz. Faster multiple emulsification with drop splitting. *Lab Chip*, 11(11): 1911–5, 2011.

[32] G. I. Taylor. The formation of emulsions in definable fields of flow. *Proc. R. Soc. Lond. A*, 146 (A858):0501–0523, 1934.

[33] H. A. Stone, B. J. Bentley, and L. G. Leal. An experimental study of transient effects in the breakup of viscous drops. *J. Fluid Mech.*, 173:131–158, 1986.

[34] W.J. Milliken and L.G. Leal. Deformation and breakup of viscoelastic drops in planar extensional flows. *J. Non-Newtonian Fluid Mech.*, 40(3):355 – 379, 1991.

[35] H. A. Stone. Dynamics of drop deformation and breakup in viscous fluids. *Annu. Rev. Fluid Mech.*, 26:65–102, 1994.

[36] Y. Navot. Critical behavior of drop breakup in axisymmetric viscous flow. *Phys. Fluids*, 11(5): 990–996, 1999.

[37] J. Li, Y. Y. Renardy, and M. Renardy. Numerical simulation of breakup of a viscous drop in simple shear flow through a volume-of-fluid method. *Phys. Fluids*, 12(2):269–282, 2000.

[38] S. Quan, D. P. Schmidt, J. Hua, and J. Lou. A numerical study of the relaxation and breakup of an elongated drop in a viscous liquid. *J. Fluid Mech.*, 640:235–264, 11 2009.

[39] A. M. Leshansky and L. M. Pismen. Breakup of drops in a microfluidic T junction. *Phys. Fluids*, 21 (2):023303, 2009.

[40] M. C. Jullien, M. J. Tsang Mui Ching, C. Cohen, L. Menetrier, and P. Tabeling. Droplet breakup in microfluidic T-junctions at small capillary numbers. *Phys. Fluids*, 21(7):072001, 2009.

[41] T. Fu, M. Youguang, D. Funfschilling, and H. Z. Li. Dynamics of bubble breakup in a microfluidic T-junction divergence. *Chem. Eng. Sci.*, 66:4184ï£¡4195, 2011.

[42] Y. X. Zhang and L. Q. Wang. Nanoliter-droplet breakup in confined T-Shaped junctions. *Curr. Nanosci.*, 7(3):471–479, 2011.

[43] D. M. Anderson, G. B. McFadden, and A. A. Wheeler. Diffuse-interface methods in fluid mechanics. *Annu. Rev. Fluid Mech.*, 30(1):139–165, 1998.

[44] R. Scardovelli and S. Zaleski. Direct numerical simulation of free-surface and interfacial flow. *Annu. Rev. Fluid Mech.*, 31(1):567–603, 1999.

[45] M. Wörner. Numerical modeling of multiphase flows in microfluidics and micro process engineering: a review of methods and applications. *Microfluid. Nanofluid.*, pages 1–46, 2012.

[46] Y. Wu, T. Fu, C. Zhu, Y. Lu, Y. Ma, and H. Li. Asymmetrical breakup of bubbles at a microfluidic T-junction divergence: feedback effect of bubble collision. *Microfluid. Nanofluid.*, 13(5):723–733, 2012.

2. Benchmark numerical simulations of segmented two-phase flows in microchannels using the Volume of Fluid method[§]

We present an extensive analysis of the performance of the Volume of Fluid (VOF) method, as implemented in OpenFOAM, in modeling the flow of confined bubbles and droplets ("segmented flows") in microfluidics. A criterion for having a sufficient grid solution to capture the thin lubricating film surrounding non-wetting bubbles or droplets, and the precise moment of breakup or coalescence is provided. We analyze and propose optimal computational settings to obtain a sharp fluid interface and small parasitic currents. To show the usability of our computational rules, numerical simulations are presented for three benchmark cases, *viz.* the steady motion of bubbles in a straight two-dimensional channel, the formation of bubbles in two- and three-dimensional T-junctions, and the breakup of droplets in three-dimensional T-junctions. An error analysis on the accuracy of the computations is presented to probe the efficacy of the VOF method. The results are in good agreement with published experimental data and experimentally-validated analytical solutions.

[§]Published as: D. A. .Hoang, V. van Steijn, L. M. Portela, M. T. Kreutzer and C. R. Kleijn. Benchmark numerical simulations of segmented two-phase flows in microchannels using the Volume of Fluid method. *Computers & Fluids*, 2013, doi: 10.1016/j.compfluid.2013.06.024.

2.1 Introduction

This chapter presents benchmark simulations for the analysis of segmented flows. Such flows are ubiquitous in so-called "digital microfluidics", where streams of discrete droplets and bubbles at small capillary number are convected through microchannel networks [1,2]. Numerical simulations, here as always, will have to resolve the most important flow features, which in this field are (1) resolving the thin film that separates the bubbles and droplets from the confining walls, relevant for most transport processes [3] and (2) the breakup of liquid threads and the associated topological changes that occur in such networks [4,5].

One of the key questions in segmented flow simulations is how to model the dynamic interface between two immiscible fluids. Numerical techniques for fluid interfaces [6,7] can be divided into two categories: Lagrangian and Eulerian. Lagrangian methods such as moving-mesh [8–11] or front-tracking [12–14] accurately resolve the shape of the interface and are for instance ideally suited to capture the thin lubricating film around steadily moving bubbles or droplets (figure 2.1(a)). It is, however, complicated to apply Lagrangian methods to problems with large interface movement and topological changes. Such problems are typically modeled by Eulerian methods, which naturally handle complex topological changes. Examples of Eulerian methods include the diffuse interface method [15,16], the Level Set (LS) method [17,18], the Volume of Fluid (VOF) method [19–21], and the Lattice-Boltzmann method [22]. Its robustness and ease of implementation and parallelization together with the ability to conserve mass and render reasonably sharp interfaces explains why VOF is implemented in many well-known commerical and open source CFD packages, such as Fluent [23], CFX [24], CFD-ACE+ [25] and OpenFOAM [26].

Despite the popularity of the VOF method, there are issues when applying this method to surface-tension-dominated flows in microchannels. VOF does not resolve the interface location with sub-grid resolution. As a consequence, the thin lubricating films can only be resolved at significant numerical cost, and the fine details close to the exact moment of breakup and coalescence cannot be resolved directly. A second issue of the VOF method is the presence of parasitic currents, which originate from errors in calculating the curvature of the interface and from an imbalance between the discrete surface tension force and the pressure-gradient terms [6,27–29]. These errors propagate dramatically into the velocity field at small capillary numbers. Parasitic currents can be reduced by using a different, additional field variable (e.g. a level set function [30] or height function [31,32]) used only to calculate the curvature. Allowing this function to be smooth one can accurately calculate curvature, but only at the expense of significant numerical cost and difficult parallelization. A less complicated approach to reduce the parasitic currents is applying a smoother to the VOF function in the interfacial region [33–35]. Smoothing leads to a less steep gradient of the VOF function, and hence improves the accuracy in the calculation of the curvature. As a consequence, parasitic

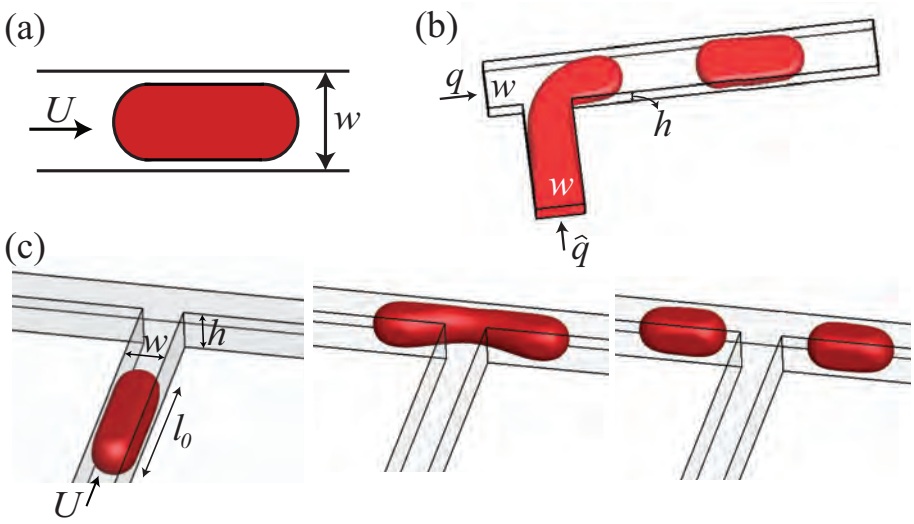

Figure 2.1 (a) Steady motion of 2D bubbles in a straight channel. (b) The formation of bubbles in a 3D T-junction. (c) The breakup of droplets in a 3D T-junction.

currents decrease significantly without much increase in computational time.

In this chapter, we present well-characterized benchmark cases that allowed us to find optimal approaches to using the VOF method for segmented flows. The three benchmark cases are shown in figure 2.1: the steady motion of 2D bubbles in a straight channel, the formation of bubbles in 3D T-junctions and the breakup of droplets in 2D and 3D T-junctions. All these cases have been extensively studied theoretically and experimentally, so in all cases we can compare to known expected values. The paper is organized as follows. A short description of the VOF method as implemented in the *interFoam* solver in OpenFOAM-1.6[36], including details of the sharpening and smoothing method, is followed by a standard stationary bubble test and a simple 2D breakup test to find the optimal parameters for the method. We then use these optimal parameters in the benchmark cases. In each of these cases, we compare to time-resolved experimental data of the fluid interface, and provide a detailed quantification of small remaining errors in the calculations. As we show below, our numerical simulations show a good agreement with experimental data and experimentally-validated analytical models.

2.2 Numerical method

2.2.1 Governing equations

In the VOF method, the transport equation for the VOF function, α, of each phase is solved simultaneously with a single set of continuity and Navier-Stokes equations for the whole flow field. Considering the two fluids as Newtonian, incompressible, and immiscible, the governing equations can be written as:

$$\nabla \cdot \mathbf{U} = 0 \tag{2.1}$$

$$\frac{\partial \rho_b \mathbf{U}}{\partial t} + \nabla \cdot (\rho_b \mathbf{U}\mathbf{U}) = -\nabla p + \nabla \cdot \mu_b (\nabla \mathbf{U} + \nabla \mathbf{U}^T) + \rho_b \mathbf{f} + \mathbf{F}_s \tag{2.2}$$

$$\frac{\partial \alpha}{\partial t} + \nabla \cdot (\alpha \mathbf{U}) = 0 \tag{2.3}$$

where $\mathbf{U}$ is the fluid velocity, p the pressure, $\mathbf{f}$ the gravitational force, and $\mathbf{F}_s$ volumetric representation of the surface tension force. The bulk density ρ_b and viscosity μ_b are computed as the averages over the two phases, weighted with the VOF function α:

$$\rho_b = \rho\alpha + \hat{\rho}(1-\alpha) \tag{2.4}$$

$$\mu_b = \mu\alpha + \hat{\mu}(1-\alpha) \tag{2.5}$$

where ρ, $\hat{\rho}$, μ and $\hat{\mu}$ are the densities and the viscosities of the two phases. In the VOF method, α is advected by the fluids. For incompressible flows, this is equivalent to a conservation law for the VOF function, and therefore ensures the conservation of mass.

The surface tension force, $\mathbf{F}_s$, is modeled as a volumetric force by the Continuum Surface Force (CSF) method[37]. It is only active in the interfacial region and formulated as $\mathbf{F}_s = \gamma\kappa(\nabla\alpha)$, where γ is the interfacial tension and $\kappa = \nabla \cdot (\nabla\alpha / |\nabla\alpha|)$ is the curvature of the interface.

2.2.2 Interface sharpening

In OpenFOAM, the fluid interface is sharpened by introducing the artificial compression term $-\nabla \cdot (\alpha(1-\alpha)\mathbf{U}_r)$ into Eq. 2.3. Thus, the VOF equation (Eq. 2.3) becomes:

$$\frac{\partial \alpha}{\partial t} + \nabla \cdot (\alpha \mathbf{U}) - \nabla \cdot (\alpha(1-\alpha)\mathbf{U}_r) = 0 \tag{2.6}$$

The artificial compression velocity $\mathbf{U}_r$ is given by:

$$\mathbf{U}_r = \mathbf{n}_f \min\left[C_\gamma \frac{|\phi|}{|S_f|}, \max\left(\frac{|\phi|}{|S_f|}\right)\right] \tag{2.7}$$

where $\mathbf{n}_f$ is the normal vector of the cell surface, ϕ is the mass flux, S_f is the cell surface area, and C_γ is an adjustable coefficient, the value of which can be set between 0 and 4. Physically, we can interpret $\mathbf{U}_r$ as a relative velocity between the two fluids, which arises from the density and viscosity change across the fluid interface. By taking the divergence of the compression velocity $\mathbf{U}_r$, the conservation of the VOF function is guaranteed[38]. The term $\alpha(1-\alpha)$ ensures that this artifact is only active in the interfacial area where $0<\alpha<1$. The level of compression depends on the value of C_γ: there is no compression with $C_\gamma=0$, a moderate compression with $C_\gamma\leq 1$, and an enhanced compression with $1<C_\gamma\leq 4$[39,40].

2.2.3 VOF smoothing

In the VOF method, the fluid interface is implicitly represented by the VOF function, the value of which sharply changes over a thin region. This abrupt change of the VOF function creates errors in calculating the normal vectors and the curvature of the interface, which are used to evaluate the interfacial forces. These errors induce non-physical parasitic currents in the interfacial region[6]. An easy way to suppress these artefacts is to compute the interface curvature κ from a smoothed VOF function $\tilde{\alpha}$, which is calculated from the VOF function α by smoothing it over a finite region around the fluid interface[6,34]. Thus, the curvature of the fluid interface is:

$$\kappa=\nabla\cdot\left(\frac{\nabla\tilde{\alpha}}{|\nabla\tilde{\alpha}|}\right) \tag{2.8}$$

whereas in all other equations, the non-smoothed VOF function α is used.

In this thesis, we applied the smoother proposed by Lafaurie et al.[33], namely a Laplacian filter that transforms the VOF function α into a smoother function $\tilde{\alpha}$:

$$\tilde{\alpha}_P=\frac{\sum_{f=1}^{n}\alpha_f S_f}{\sum_{f=1}^{n}S_f} \tag{2.9}$$

where the subscript P denotes the cell index and f denotes the face index. The interpolated value α_f at the face centre is calculated using linear interpolation. The application of this filter can be repeated m times to get a smoothed field. It should be stressed that smoothing tends to level out high curvature regions and should therefore be applied only up to the level that is strictly necessary to sufficiently suppress parasitic currents.

2.2.4 Numerical setup and discretization

Our numerical simulations were performed with the finite-volume-based code OpenFOAM[36] on co-located grids. The PISO (pressure-implicit with splitting of operators)

scheme is applied for pressure-velocity coupling[41]. The transient terms are discretized using a first order implicit Euler scheme, controlling the time step by setting the maximum Courant number to 0.3. Higher Courant numbers were found to lead to a distortion of the interface due to increased parasitic currents. We also examined the performance of a second order implicit backward time integration scheme for one of the test cases on droplet breakup described in section 2.3.3. Since the difference in breakup time was less than 1%, we used first order Euler schemes throughout this work. For spatial discretization, a second order TVD scheme with van Leer limiter was used. To ensure the boundedness of the VOF function, we used a special discretization scheme developed by OpenCFD Ltd., *interfaceCompression*, with the MULES (Multidimensional Universal Limiter with Explicit Solution) explicit solver[26].

The flow domains were meshed with hexahedral cells using Blockmesh, an internal mesh generator of OpenFOAM. At the channel walls, no-slip and zero contact angle boundary conditions were specified. This contact angle boundary condition is used to correct the surface normal vector, and therefore adjusts the curvature of the interface in the vicinity of the wall. A uniform velocity and zero-gradient for pressure and VOF function α were applied at the inlet. At the outlet, we imposed a fixed-valued (atmospheric) pressure boundary condition and zero-gradient for velocity and VOF function α.

2.3 Optimization of Computational Settings

2.3.1 Interface sharpening

To evaluate the influence of the interface sharpening coefficient C_γ, we simulated the relaxation of a 2D, stationary, circular droplet from a square initial shape, in the absence of the gravity. The fluid properties are similar to those considered by Brackbill et al.[37]: background density $\rho{=}1000\,\mathrm{g/L}$, viscosity $\mu{=}1\,\mathrm{mPas}$, density ratio $\rho/\hat{\rho}{=}2$, viscosity ratio $\mu/\hat{\mu}{=}0.4$ and surface tension $\gamma{=}23.6\,\mathrm{mN/m}$. Differently from the test case in Brackbill et al.[37], the diameter of the relaxed droplet was set to $2R{=}300\,\mu\mathrm{m}$, which appropriately represents the typical dimension of microfluidic systems. The domain size was $4R{\times}4R$. The grid cell size is $\Delta{=}0.04R$, corresponding to $100{\times}100$ cells.

Without interface compression ($C_\gamma = 0$), the dynamics of the relaxation process is shown in figure 2.2a (top). On the capillary time-scale $\gamma/\mu R$, the droplet obtains its final circular shape at $t\gamma/\mu R \sim 350$. The corresponding thickness of the interface, which is approximately 6 grid cells, is shown in 2.2b (top). Parasitic currents were characterized based on the magnitude of the maximum velocity, $\max(|\mathbf{U}|)$, which we normalized by the capillary velocity γ/μ. The maximum velocity decreases during

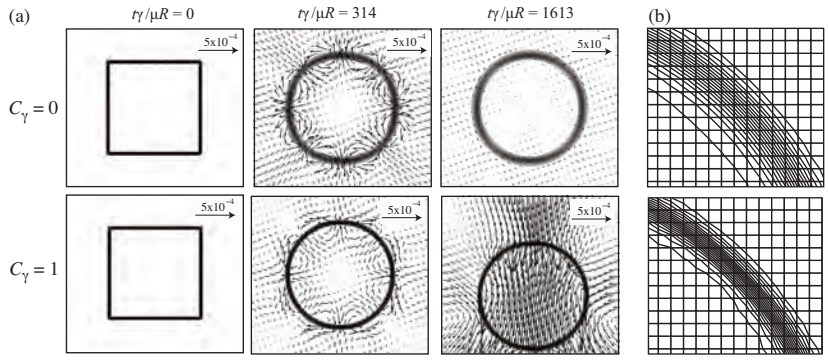

Figure 2.2 (a) Snapshots of the interface shape and the flow field during the relaxation of a bubble from its initially square shape without (top) and with (bottom) interface compression. Velocities are scaled with the capillary velocity γ/μ. The arrow indicates the reference velocity. (b) Snapshots of the fluid interface without (top) and with (bottom) interface compression.

the relaxation, and levels off at a non-zero value due to the parasitic currents when the droplet reaches its final shape as shown in figure 2.3.

Compressing the interface leads to a thinner interface of approximately 4 grid cells and increased parasitic currents, as qualitatively shown from the comparison between $C_\gamma = 1$ and $C_\gamma = 0$ in figures 2.2 and 2.3. While the bubble stays in the center without compression, compressing the interface leads to an increase in the parasitic currents. As a consequence of the large parasitic currents, the bubble drifts away from the initial position. Due to the "random nature" of the parasitic currents, the particular direction of the drift has no physical meaning, and a long simulation in a large domain would lead to a "random walk" for the bubble. More quantitatively, we compare the relative thickness ϵ_δ of the fluid interface, and the relative maximum time-averaged parasitic currents ϵ_{pc} for different values of C_γ, normalized with the values obtained for $C_\gamma = 0$ according to:

$$\epsilon_\delta = \frac{\delta}{(\delta)_{C_\gamma=0}} \tag{2.10}$$

$$\epsilon_{pc} = \frac{\int_t \max(|\mathbf{U}|)\mathrm{dt}}{(\int_t \max(|\mathbf{U}|)\mathrm{dt})_{C_\gamma=0}} \tag{2.11}$$

The time integral in Eq. 2.11 is taken over a relatively long time interval ($\Delta t\gamma/\mu R \approx 2000$), starting at the moment that the droplet has relaxed to its final circular shape at $t\gamma/\mu R \approx 350$. Table 2.1 shows that increasing C_γ leads to a decrease of the interface thickness δ, and to an increase of the parasitic currents. With $C_\gamma = 1$, the thickness of the fluid interface decreases by a factor 1.79 compared to the case with $C_\gamma = 0$, and the time-averaged parasitic currents increase by a factor 1.87. Further increasing C_γ from

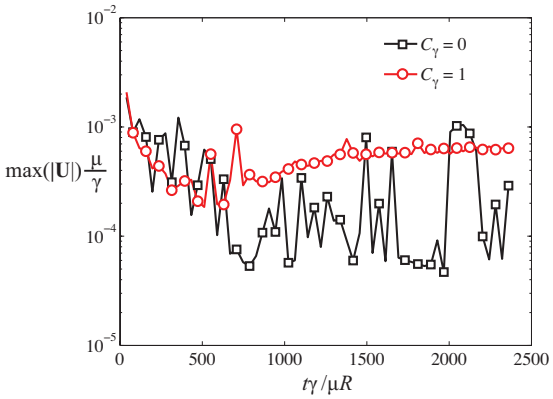

Figure 2.3 Evolution of the maximum velocity during relaxation without ($C_\gamma = 0$) and with ($C_\gamma = 1$) interface compression.

1 to 4 only reduces the interface thickness by a factor 1.31 while the time-averaged parasitic current increases by a factor 2.56. Thus, we used $C_\gamma = 1$ for all remaining simulations to get a sharp interface while keeping the parasitic currents small. An increase of parasitic currents due to the use of $C_\gamma = 1$ can be suppressed by applying the smoother as described in the next section.

2.3.2 VOF smoothing

To study the effect of smoothing the VOF function, we performed simulations with the same test case as described in the previous section. Figure 2.4a shows two snapshots of the parasitic currents after the droplet has relaxed to its steady shape for $m = 0$ (no smoother) and $m = 2$ (applying the smoother twice). The corresponding time traces of the maximum magnitude of the parasitic currents are shown in figure 2.4b. Comparing the magnitude of the parasitic currents at large t shows that the currents are reduced by one order of magnitude when twice applying the smoother. Moreover, the magnitude of the parasitic currents monotonically decreases with the smoother, while it goes

Table 2.1 The influence of C_γ on the interface thickness and the time-averaged parasitic currents.

C_γ	0	1	2	3	4
ϵ_δ	1	0.56	0.51	0.44	0.43
ϵ_{pc}	1	1.87	2.99	4.05	4.79

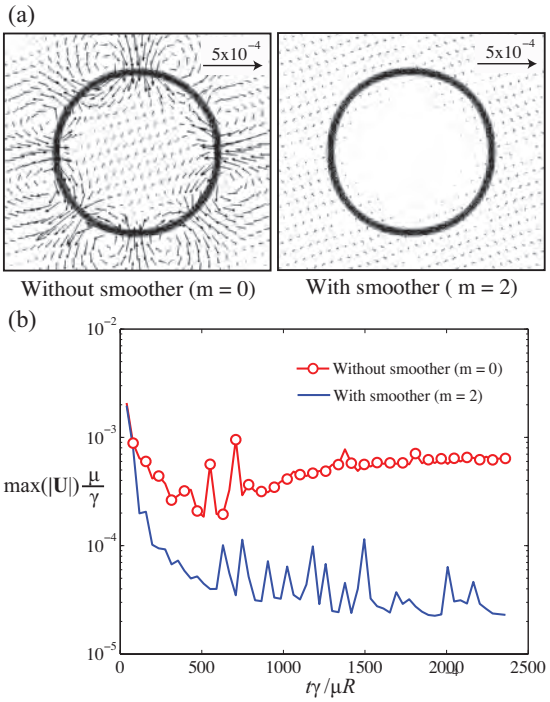

Figure 2.4 (a) Snapshots of the parasitic currents, scaled with γ/μ, at the moment the bubble has relaxed to its final steady shape ($t\gamma/\mu R$=350), for simulations without and with the Lafaurie smoother. The arrow indicates the reference velocity. (b) Corresponding time traces of the dimensionless maximum magnitude of parasitic currents. (All evaluated at interface compression $C_\gamma = 1$.)

through a minimum without the smoother.

We studied the influence of the number of repeats m of the smoother on the magnitude of the parasitic currents and compared the relative maximum time-averaged parasitic currents after the droplet has relaxed to its circular shape using:

$$\epsilon_{pc} = \frac{\int_t \max(|\mathbf{U}|)\mathrm{dt}}{(\int_t \max(|\mathbf{U}|)\mathrm{dt})_{m=0}} \tag{2.12}$$

where again the time integral in Eq. 2.12 is again taken over a long time interval, starting at the moment that the droplet has fully relaxed to its final circular shape. Table 2.2 shows that the magnitude of parasitic currents decreases sevenfold from $m=0$ (no smoothing) to $m=1$, and a further nearly twofold from $m=1$ to $m=2$. For $m>2$, only a slight further decrease was observed. Therefore, $m=2$ is used in all remaining simulations.

We also tested the performance of the smoother with other grid resolutions, $\Delta/R = 0.2, 0.066, 0.028, 0.02$, corresponding to mesh sizes $20\times20, 60\times60, 140\times140, 200\times200$. Comparing simulations with ($m=2$) and without ($m=0$) smoother on the same grid, we found that $\epsilon_{pc}\sim0.2$ for low grid resolutions (Δ/R=0.2, 0.066) and $\epsilon_{pc}\sim0.08$ for the higher grid resolutions. Furthermore, we found that parasitic currents increase with decreasing grid cell size, as reported previously[34].

2.3.3 Criterion for the breakup of the fluid interface

It is well-known that in the VOF method, breakup or coalescence of bubbles and droplets is unavoidable when the distance between two interfaces is on the order of a few grid cells. Therefore, it is difficult to determine whether such events are physical or due to this numerical artefact. We demonstrate how to determine the error in breakup time for the breakup of a 2D droplet in a T-junction. The droplet has an initial length l_0 and moves through the $w=30\,\mu\mathrm{m}$ wide channels of the T-junction at a speed U, as shown in the inset of figure 2.5. We use an initial droplet length $l_0=5.7w$ and velocity of $U=4\,\mathrm{cm/s}$ and chose the fluid properties such that they mimic those of droplet flows typically encountered in lab-on-a-chip devices, i.e. aqueous droplets ($\hat{\mu}=1\,\mathrm{mPas}$, $\hat{\rho}=1000\,\mathrm{g/L}$) dispersed in a more viscous carrier fluid ($\mu=8\,\mathrm{mPas}$, $\rho=770\,\mathrm{g/L}$) with an interfacial tension $\gamma=5\,\mathrm{mN/m}$. The resulting Capillary and Reynolds numbers are $Ca=\mu U/\gamma=6.4\times10^{-3}$ and $Re=\rho U w/\mu=1\times10^{-2}$.

To study the influence of grid size on the breakup time, we performed simulations with five different uniform grid cell sizes $\Delta/w=1/30, 1/60, 1/80, 1/120$ and $1/200$. The temporal evolution of the shortest distance d between two interfaces, rescaled with the grid cell size Δ, is shown in figure 2.5. For all grid cell sizes, the breakup happens numerically at $d\sim K\Delta$, with $K\approx6$. As a result, the numerical breakup time t_b increases with grid refinement in a way that is not related to the order of the numerical scheme, but rather to the shape of the $d\sim t$ curve. In most situations, one has a scaling of self-similar interface shapes close to breakup of the form $d\sim t^\beta$ or $1-d\sim t^\beta$, such that the exponent β is known from theory (for an overview of the most common cases, see Eggers and Villermaux[42]) or from the simulations themselves. For this particular 2D T-junction problem, self-similarity leads to $d/w\sim1-(Ut/w)^\beta$, with $\beta=3/7$ as derived by Leshansky et al.[5], shown in the inset of figure 2.5. Because the numerical

Table 2.2 The influence of the number of repeats m of the smoother on the magnitude of the parasitic currents. (All evaluated at interface compression $C_\gamma=1$)

m	0	1	2	3	4
ϵ_{pc}	1	0.14	0.078	0.072	0.07

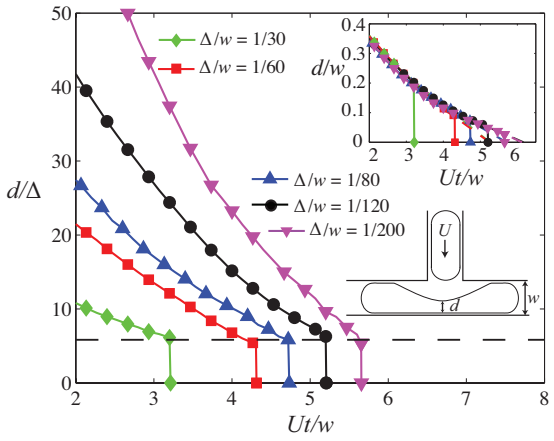

Figure 2.5 Dynamics of droplet interface in 2D breakup with different grid cell sizes Δ/w. The inset shows that d/w evolves similarly for different Δ/w.

breakup happens at $d = K\Delta$, we use the known scaling to find the error in breakup time as

$$\frac{t_{b,\Delta}}{t_{b,\Delta\to 0}} = \left(1 - \frac{K\Delta}{w}\right)^{1/\beta} \tag{2.13}$$

For $K\Delta/w \ll 1$, we expand to find for the relative error, up to $O[(K\Delta/w)^2]$,

$$\epsilon_t = \frac{t_{b,\Delta\to 0} - t_{b,\Delta}}{t_{b,\Delta\to 0}} = \frac{K}{\beta}\frac{\Delta}{w}. \tag{2.14}$$

So the error in the predicted breakup time is linear in Δ/w, and only depends on the value of β. From linear extrapolation of the d/w curve on our finest mesh, we estimate $(Ut_b/w)_{\Delta\to 0}$ to be 6.12. With this value, we compute the error of the breakup time for different Δ/w. Table 2.3 shows that indeed the error ϵ_t varies linearly with Δ/w for small Δ/w, and that the proportionality constant is close to K/β.

A guide for the determination of a sufficiently fine grid to correctly capture the breakup time can be given based on Eq. 2.14. Even without knowing a theoretical value for

Table 2.3 Relative errors of the breakup time for different grid resolutions.

Δ/w	1/30	1/60	1/80	1/120	1/200
ϵ_t	0.48	0.3	0.23	0.15	0.085
$\epsilon_t(\Delta/w)^{-1}$	14.4	18	18.4	18.8	17

the exponent β in the pinching rate, we can estimate it from fitting the time evolution of the neck thickness in a coarse-grid simulation. We then use this value to predict the grid cell size needed to reach a given error in the breakup time. Using this strategy, concluding that $\beta \approx 0.38$ from the interface evolution obtained at $\Delta/w = 1/30$ and assuming $K = 6$, we predict that a relative error of 0.085 can be obtained with a grid cell size $\Delta/w = 1/165$. This prediction is in close agreement with our simulations. It should be noted that the proposed criterion does not take any acceleration of the pinch-off by intermolecular forces into account. Such acceleration is well known in thin-film rupture where, as also here in 2D, capillary action does not destabilize the interface. Such effects become prominent typically at length scales much smaller than the present grid size[43], such that their impact on our criterion is small.

2.4 Benchmark cases

2.4.1 Motion of bubbles in a straight two-dimensional channel

The first benchmark case we consider is the steady motion of a non-wetting air bubble through a straight two-dimensional channel. The thickness of the lubricating film, b, separating the bubble from the channel walls is typically two orders of magnitude smaller than the channel width; hence, capturing this film and resolving the flow inside it is a computationally demanding task.

We simulated the motion of a droplet of length $l_0 = 200\,\mu\mathrm{m}$ in a fixed straight 2D microchannel of width $w = 100\,\mu\mathrm{m}$ and length $800\,\mu\mathrm{m}$ as shown in figure 2.1(*a*). We use air ($\hat{\rho}$=1 g/L, $\hat{\mu}$=18 µPas) and ethanol (ρ=789 g/L, μ=1.2 mPas) as the working fluids, with an interfacial tension of $\gamma = 20\,\mathrm{mN/m}$. The bubble is initialized as a rectangle with its rear positioned $20\,\mu\mathrm{m}$ downstream from the inlet. Before we switch on the flow, we first let the bubble relax to its static equilibrium shape. We then continuously inject the continuous phase at a velocity U, such that the bubble is pushed through the channel. Well before reaching the exit, the bubble adopts its new steady-state shape and keeps this shape for several thousand time steps in all simulations. Typical wall-clock times for these simulation were 12 hours on a single processor.

Grid dependency of the film thickness was performed for a fixed inlet velocity $U = 1.67\,\mathrm{cm/s}$, corresponding to $Ca = \mu U/\gamma = 10^{-3}$ and $Re = \rho U w/\mu = 0.32$. We used uniform grids with grid cell sizes Δ/w ranging from $1/75$ to $1/400$ and measured the dimensionless film thickness b/w as the scaled distance between the iso-surface $\alpha = 0.5$ and the channel wall at the middle of the bubble. For the two coarsest meshes ($\Delta/w = 1/75, 1/100$), the lubricating film is not resolved as shown in figure 2.6a. For $\Delta/w \leq 1/300$, we obtained mesh independent film-thicknesses that were within 1% of our finest mesh solution. Moreover, these film thicknesses were within 3% of the

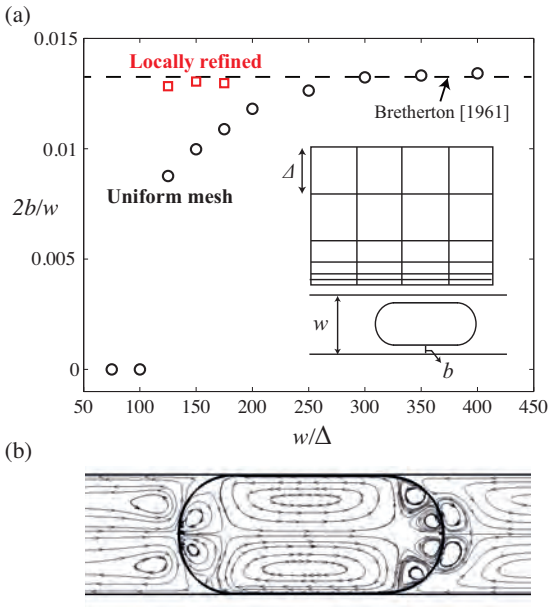

Figure 2.6 (a) Grid dependence of the lubricating film thickness for a bubble flowing in a straight channel at $Ca = 10^{-3}$. Uniform meshes with grid size Δ (circles), and locally refined meshes with base grid size Δ (squares). Also shown is the theoretically predicted film thickness by Bretherton [44] (dashed line). (b) Bubble shape and flow pattern for the finest locally refined mesh, qualitatively agreed with numerical simulations by Afkhami et al. [32]. The streaklines are plotted in the frame of reference of the bubble.

theoretical prediction ($b/w = 0.0134$ for $Ca = 10^{-3}$) by Bretherton [44]. This means that roughly 2 grid cells are needed to properly capture the lubricating film.

The requirement to successfully capture the lubricating film leads to very large numbers of grid cells when uniform meshes are used. For our 2D case, 0.8 million grid points were needed to reach a converged solution. In 3 dimensions, the required number of grid cells is prohibitively large. We therefore studied the possibility to apply relatively coarse uniform grids in the core of the domain, in combination with local grid refinement in the lubricating film near the wall. On a coarse base grid with uniform grid cell size Δ, we recursively divided the cell closest to the walls into four smaller cells in the direction perpendicular to the wall. The size of the smallest cell is then $\Delta/8$, as shown in the inset of figure figure 2.6(a). With this method, we obtained accurate results for the film thickness on a base grid with $\Delta/w = 1/125$, *i.e.* less than one base grid cell within the lubricating film. Figure 2.6(b) shows that the resulting droplet shape, together with the streaklines in the frame of reference of the bubble, qualitatively agrees with simulations by Afkhami et al. [32]. We do note that velocities

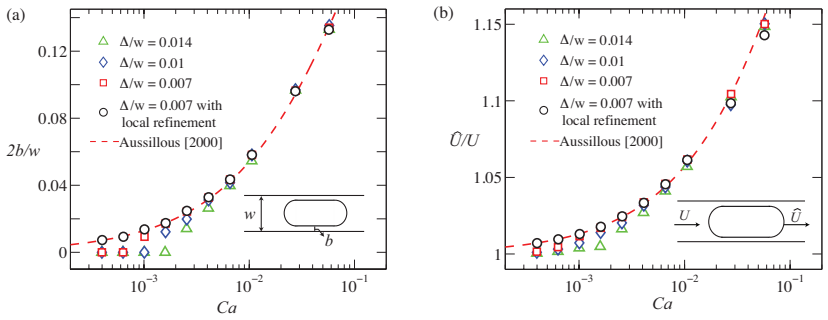

Figure 2.7 A comparison of the film thickness (a) and bubble velocity (b) between numerical simulations and experimentally-validated analytical model of Ref.[45] at different capillary numbers.

and pressures were not accurately resolved on too coarse base meshes ($\Delta/w > 1/50$) (data not shown). These results indicate that 3D simulations can be performed with $\sim 10\times$ less cells when locally refined meshes are used instead of uniform ones.

We further validate the above test case by extending the range of film thicknesses ($0.0073 < b/w < 0.1326$), which is done by varying the capillary numbers between 4×10^{-4} and 6×10^{-2}. In all cases, the Reynolds number is less than 20. We used four different meshes: uniform meshes with $\Delta/w = 1/75, 1/100, 1/150$ and a locally refined grid with a uniform base grid cell size $\Delta/w = 1/150$, locally refined near the wall to $1/1200$. In figure 2.7(a) we compare the scaled film thickness b/w, to the experimentally validated theoretical value due to Aussillous and Quere[45],

$$2b/w = \frac{0.643(3Ca)^{2/3}}{1 + 0.643 \cdot 2.50 \cdot (3Ca)^{2/3}} \tag{2.15}$$

which is a slight improvement on the "classical" Landau-Levich-Bretherton result ($2b/w = 0.643(3Ca)^{2/3}$) that takes the effect of finite film thickness on the nose curvature into account. Note that the constant 2.50 was obtained by fitting to an extensive experimental data set. To validate the dimensionless bubble velocity $\hat{U}/U$ (figure 2.7(b)), we adapted the Bretherton's law for a case of a 2D bubble in a Poiseuille flow between two plates:

$$\hat{U}/U = 1/(1 - 2b/w) \tag{2.16}$$

Focusing first on the larger values of Ca, we find that all used grids accurately capture the film thickness and bubble velocity as shown in figure 2.7(a-b). This agrees with our finding that two grid cells suffice to capture the film. For $Ca < 5 \times 10^{-3}$, the resulting film thickness drops below $b/w < 0.02$ such that this requirement is no longer satisfied. Indeed, the uniform grids are unable to resolve the lubricating film and consequently lead to inaccurate predictions of the bubble velocity. Clearly, a locally

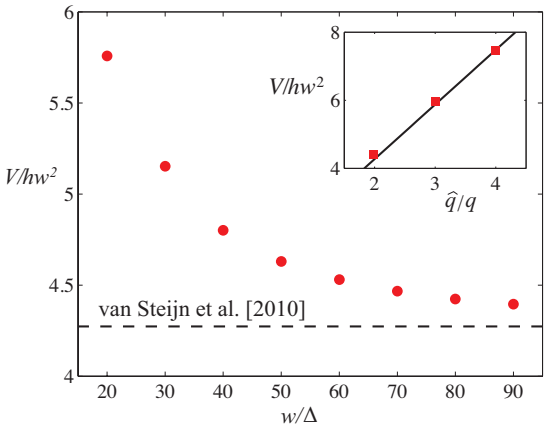

Figure 2.8 Grid dependency study on the dimensionless bubble volume generated in a T-junction at a fixed ratio of flow rates $\hat{q}/q=2$. The bubble volumes obtained with grid cell sizes $\Delta/w<1/80$ agree with predictions from the experimentally-validated analytical model (dashed line) by van Steijn et al.[46] within 4%. The inset shows bubble volumes for $\Delta/w=1/80$ as a function of $\hat{q}/q$, again in good agreement with model by van Steijn et al.[46] (solid line).

refined grid is needed for these small values of the capillary number. Using such a mesh, the error between our numerical simulations and the theoretical predictions for b/w was 3% on average and never larger than 5.5% in the entire range of tested *Ca*. This is an excellent agreement, considering that only 2 grid cells fall within the film thickness b for the smallest capillary numbers studied. Further improved accuracy may be obtained through further grid refinement, as shown in figure 2.6. For $\hat{U}/U$, the error between our numerical simulations and the theoretical predictions was even better, *viz.* 0.2% on average and never larger than 1.1% in the entire range of tested *Ca*.

2.4.2 Bubble formation in a three-dimensional T-junction

Establishing that our approach is suited for simulating two-dimensional problems in which no large topological changes occur, we now further validate our approach with a more complicated three-dimensional problem, involving the breakup of a fluid interface. We simulated the formation of bubbles in a microfluidic T-junction as shown in figure 2.1(*b*). Air is introduced from the $100\,\mu\mathrm{m}$ wide and $33\,\mu\mathrm{m}$ deep side channel at a flow rate $\hat{q}$, and water is introduced from the $100\,\mu\mathrm{m}$ wide and $33\,\mu\mathrm{m}$ deep main channel at a flow rate $q=4.95\,\mu\mathrm{l/h}$. The surface tension is set to $\gamma=70\,\mathrm{mN/m}$. In all cases, we consider surface-tension dominated flows at low Reynolds number ($Ca=\mu q/hw\gamma\sim O(10^{-3})$, $Re=\rho q/w\mu\sim O(10^{-2})$).

Table 2.4 Convergence rates and relative errors of the bubble volumes for different grid resolutions.

Δ/w	1/20	1/30	1/40	1/50	1/60	1/70	1/80	1/90
p		0.58	1.78	1.70	1.62	1.85	1.96	
ϵ_V	0.345	0.203	0.121	0.081	0.058	0.043	0.033	0.026

Grid dependency of the simulated bubble volume was tested on uniform grids for a bubble generated at the T-junction for $\hat{q}/q=2$. Typical wall clock times for the simulation of one bubble formation period were 200 hours for the finest meshes using 8 processors in parallel on a Beowulf Linux cluster. A comparison between the dimensionless bubble volume, V/hw^2, computed for grid cell sizes in the range $1/90<\Delta/w<1/20$ shows how the solution converges (Figure 2.8). We computed the convergence rate p from:

$$\frac{(\Delta_{l+1})^p-(\Delta_l)^p}{(\Delta_l)^p-(\Delta_{l-1})^p}=\frac{V_{l+1}-V_l}{V_l-V_{l-1}} \tag{2.17}$$

where l is the level of grid refinement. As expected for a second order discretization scheme, this convergence rate approaches a value of two for the finest meshes as shown in table 2.4. The relative error of the simulated bubble volumes is computed as:

$$\epsilon_V=\frac{V_l-V_{\Delta\to 0}}{V_{\Delta\to 0}} \tag{2.18}$$

with $(V/hw^2)_{\Delta\to 0}$ computed based on Richardson extrapolation[47]. For the finest meshes ($\Delta/w\leq 1/60$), the bubble volume is within 6% of $(V/hw^2)_{\Delta\to 0}=4.282$ as shown in table 2.4.

Validation was done by comparing the simulated bubble volumes with the experimentally-validated analytical model developed in our group[46]. Good agreement was found, with deviation from the theoretical value of $V/hw^2=4.273$ within 5% for a cell size of $\Delta/w=1/70$, within 4% for $\Delta/w=1/80$, and within 3% for the finest mesh ($\Delta/w=1/90$). Moreover, the agreement of the extrapolated bubble volume $(V/hw^2)_{\Delta\to 0}=4.282$ is excellent and within 0.2%. Also for flow rate ratios beyond $\hat{q}/q=2$ simulations and model agree within 4% as shown in the inset of figure 2.8.

Further validation was done by studying the dynamics of the fluid interface during bubble formation and pinch-off. We recorded the temporal evolution of the neck thickness $2r/w$ of the bubble in formation, and compared our simulation with the experimentally-validated model by van Steijn et al.[48]. Both the dynamic evolution of the interface and the critical radius at which the neck rapidly collapses are successfully captured, as shown in figure 2.9.

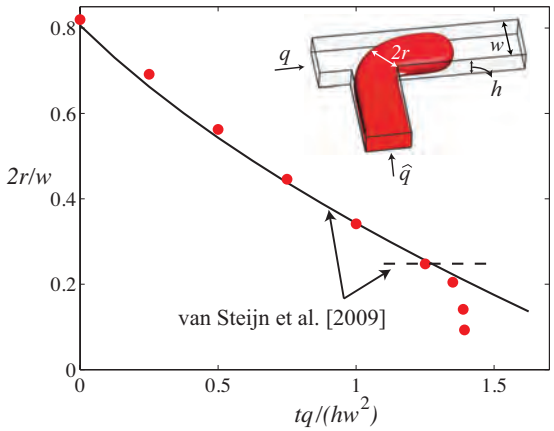

Figure 2.9 Comparison of the evolution of the neck thickness between simulations (dots), and the analytical model by van Steijn et al.[48] for the interface evolution (solid line) and critical neck thickness (dashed line): $\Delta/w=80$; Conditions: $\hat{q}/q=2$.

An interesting observation is that, in the above simulations, we found that resolving the lubricating film was not needed to accurately predict the bubble volume and the dynamics of the fluid interface. This is a clear deviation from what we found in the 2D test case described earlier. In a 2D case, and as a matter of fact also in the case of 3D circular or elliptic channels in which the continuous fluid can only flow around the bubbles through the thin lubricating film[49], not resolving the lubricating film means that no continuous liquid can flow past the bubble. In a 3D case with rectangular channels, however, so-called gutters are formed in the corners of the channels. Most of the fluid passing the bubble flows through the gutters, rather than through the lubricating film[4]. Accurate predictions of bubble volume and interface dynamics therefore primarily requires that the gutters are accurately represented. These gutters are much wider than the lubricating film, and can be resolved on much coarser meshes. Our mesh dependency study suggests that the gutters are well resolved for grid cell sizes $\Delta/w<1/60$. According to Wong et al.[50], the radius R_g/w of the gutter can be computed as:

$$\frac{R_g}{w}=\frac{h}{2w+2h} \tag{2.19}$$

For our geometry ($h/w=0.33$), this leads to R_g/w is 0.12. Combined with the observation that grid cell sizes $\Delta/w<1/60$ are needed to obtained accurate results, we may conclude that the gutters are adequately resolved when there are at least 7 grid cells along the edge of the gutter.

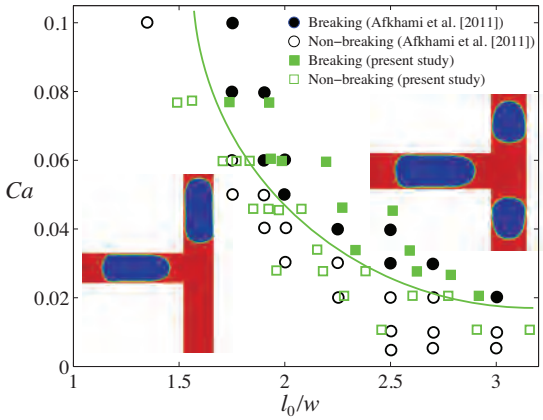

Figure 2.10 A comparison of the 2D breakup phase diagram shows an excellent agreement between our simulations (squares) and published numerical data (circles)[32]. Open symbols represent non-breaking droplets and closed symbols represent breaking droplets. The solid line is included to guide the eye and indicates the transition from the non-breaking to the breaking regime.

2.4.3 Bubble/Droplet breakup in three-dimensional T-junctions

This section presents a benchmark case of the breakup of bubbles/droplets in 3D symmetric T-junctions as depicted in figure 2.1(c). A bubble/droplet of length l_0 flowing into a symmetric T-juntion of height h and width w with a velocity U can either break into two equally sized droplets, or move into one of the branches of the T-junction. Whether or not the bubble/droplet breaks, depends on it scaled length l_0/w and the capillary number Ca. Many computational and experimental studies report breakup phase diagrams expressed in these two parameters[16,32,51,52]. Here we examine the performance of our VOF approach, applying the rules for the computational settings from earlier sections, in predicting the breakup behavior.

First, we validated our VOF method by comparing the phase diagram for a 2D T-junction obtained in this study with the phase diagram reported by Afkhami et al.[32]. We performed simulations for capillary numbers $0.01 \leq Ca \leq 0.08$ and droplet lengths $1.5 < l_0/w < 3.2$ using the same channel geometry and fluid properties as reported in section 2.3.3, which closely resemble those used by Afkhami et al.[32]. For the smallest capillary number $Ca = 0.01$, the thickness of the lubricating film is $b/w = 0.031$. As discussed previously, it is necessary to have at least 2 grid cells inside the lubricating film to correctly capture its thickness, which is essential in 2D simulations. Thus, we used a uniform base mesh with $\Delta/w = 1/45$, which was refined twice near the walls to get a local grid size $\Delta/w = 1/90$. With these settings, we found that the transition

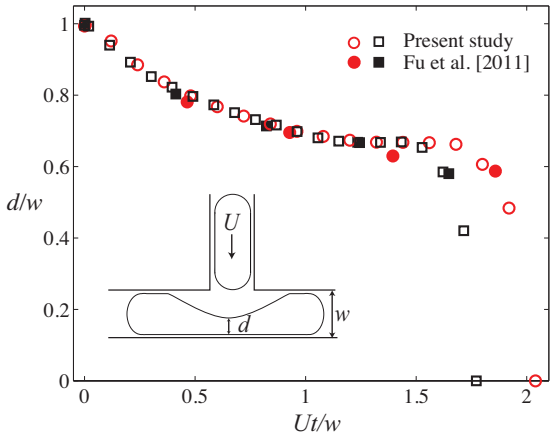

Figure 2.11 A comparison of the evolution of the neck thickness shows a good agreement between numerical data (open symbols) and experimental data (closed symbols)[53] for two cases: ($l_0/w = 4.13$, $Ca = 9.8 \times 10^{-4}$, squares) and ($l_0/w = 3.39$, $Ca = 1.2 \times 10^{-3}$, circles).

between breaking and non-breaking droplets predicted by our simulations agrees well with the simulations byAfkhami et al.[32], as shown in figure 2.10.

Then, we studied the dynamics of a bubble breakup, by recording the dimensionless neck thickness d/w in 3D simulations as a function of the dimensionless time for two cases ($l_0/w = 4.13$, $Ca = 9.8 \times 10^{-4}$) and ($l_0/w = 3.39$, $Ca = 1.2 \times 10^{-3}$). The channel geometry and the fluid properties were chosen such that they match with those used in an experimental study by Fu et al.[53]: $h{=}w{=}400\,\mu\mathrm{m}$, the bubble phase is nitrogen gas with viscosity of $17.8\,\mu\mathrm{Pas}$ and density of $1.25\,\mathrm{g/L}$; the continuous phase is 0.1wt%SDS in water with viscosity of $0.92\,\mathrm{mPas}$ and density of $1000\,\mathrm{g/L}$ and the surface tension is $39\,\mathrm{mN/m}$. In section 2.4.2, we showed that, in 3D simulations, it is sufficient to accurately capture the gutters in the corners of the channels, rather than the lubricating films at the walls. With Eq. 2.19 and $h/w = 1$, $\Delta/w = 1/40$ gives 10 grid cells along the edge of the gutter, which, according to what was shown in section 2.4.2, is sufficient to adequately resolve the flow in the gutter. Using this grid cell size, we successfully captured the dynamics of the droplet breakup for both cases. As shown in figure 2.11, the differences between our simulations on a $\Delta/w = 1/40$ mesh and experimental data are less than 8% for all time instances. Although this is probably already within the experimental error, further improvement of the accuracy of the simulations can be expected on finer meshes, as shown in section 2.4.2.

2.5 Conclusions

We have shown that the movement, formation and breakup of confined bubbles and droplets in microfluidic systems can be predicted in very good agreement with experimental data and theory using VOF simulations. The test cases we used, all fully documented and accompanied by extensive experimental validation, form a rigorous set of benchmarks for the ability of a numerical fluid simulation to handle large interfacial tension, topological changes and large separation of characteristic length and time scales.

The lubricating film between a bubble/droplet and the channel wall, which is orders of magnitude smaller than the channel diameter, was predicted within 5% of the theoretical value, provided that, through local grid refinement, the film spans at least two grid cells. With this grid-requirement fulfilled, the bubble velocity is also predicted within 5% of theoretical values.

The volume of bubbles created in a three-dimensional T-junction agreed within 3% with experimental and theoretical predictions, for which it was necessary and sufficient to resolve the gutters in the corners of the channels by at least 7 grid points.

The dynamics of the breakup of a bubble in a three-dimensional T-junction was predicted in excellent agreement with experiments, for which it was also necessary and sufficient to resolve the gutters in the corners of the channels; with 10 grid points along the edge of the gutters, the difference between experiments and simulations was always less than 8%. The prediction of breakup time is first order accurate in grid cell size and independent of the numerical order of the underlining spatial discretization. We present a simple method to calculated the error in the breakup time.

We provide a detailed account of balancing interface sharpness and parasitic currents by using a Laplacian smoother and interface compression, and provide guidelines for the choice of their tunable parameters. The simulations were performed with the *interFoam* solver in OpenFOAM-1.6, and we show that with the proper choice of parameters VOF is an efficient method to obtain accurate simulations of segmented flows in microchannels. Since the VOF method implemented in OpenFOAM is a very standard finite volume VOF implementation, we believe that the guidelines and benchmark cases proposed in this study are valid also for other finite volume VOF implementations.

Bibliography

[1] A. J. deMello. Control and detection of chemical reactions in microfluidic systems. *Nature*, 442 (7101):394–402, 2006.

[2] R. Seemann, M. Brinkmann, T. Pfohl, and S. Herminghaus. Droplet based microfluidics. *Rep. Prog. Phys.*, 75:016601, 2012.

[3] M. T. Kreutzer, F. Kapteijn, J. A. Moulijn, and J. J. Heiszwolf. Multiphase monolith reactors: Chemical reaction engineering of segmented flow in microchannels. *Chem. Eng. Sci.*, 60(22):5895–5916, 2005.

[4] D. A. Hoang, L. M. Portela, C. R. Kleijn, M. T. Kreutzer, and V. van Steijn. Dynamics of droplet breakup in a T-junction. *J. Fluid Mech.*, 717:R4, 2013.

[5] A. M. Leshansky, S. Afkhami, M.-C. Jullien, and P. Tabeling. Obstructed breakup of slender drops in a microfluidic T junction. *Phys. Rev. Lett.*, 108:264502, Jun 2012.

[6] R. Scardovelli and S. Zaleski. Direct numerical simulation of free-surface and interfacial flow. *Annu. Rev. Fluid Mech.*, 31(1):567–603, 1999.

[7] M. Wörner. Numerical modeling of multiphase flows in microfluidics and micro process engineering: a review of methods and applications. *Microfluid. Nanofluid.*, pages 1–46, 2012.

[8] M.T. Kreutzer, J.J.W. Bakker, F. Kapteijn, J.A. Moulijn, and P.J.T. Verheijen. Scaling-up multiphase monolith reactors: Linking residence time distribution and feed maldistribution. *Ind. Eng. Chem. Res.*, 44(14):4898–4913, JUL 6 2005.

[9] M. D. Giavedoni and F. A. Saita. The axisymmetric and plane case of a gas phase steadily displacing a Newtonian liquid – A simultaneous solution to the governing equations. *Phys. Fluids*, 9(8):2420–2428, 1997.

[10] A. L. Hazel and M. Heil. The steady propagation of a semi-infinite bubble into a tube of elliptical or rectangular cross-section. *J. Fluid Mech.*, 470:91–114, 2002.

[11] Z. Tukovíc and H. Jasak. A moving mesh finite volume interface tracking method for surface tension dominated interfacial fluid flow. *Comp. Fluid.*, 55(0):70 – 84, 2012.

[12] S. O. Unverdi and G. Tryggvason. A front-tracking method for viscous, incompressible, multi-fluid flows. *J. Comp. Phys.*, 100(1):25 – 37, 1992.

[13] G. Tryggvason, A. Esmaeeli, J. Lu, and S. Biswas. Direct numerical simulations of gas/liquid multiphase flows. *Fluid Dynamics Research*, 38(9):660, 2006.

[14] M. Muradoglu and S. Tasoglu. A front-tracking method for computational modeling of impact and spreading of viscous droplets on solid walls. *Computers & Fluids*, 39(4):615 – 625, 2010.

[15] D. M. Anderson, G. B. McFadden, and A. A. Wheeler. Diffuse-interface methods in fluid mechanics. *Annu. Rev. Fluid Mech.*, 30(1):139–165, 1998.

[16] M. De Menech. Modeling of droplet breakup in a microfluidic T-shaped junction with a phase-field model. *Phys. Rev. E*, 73(3), 2006.

[17] M. Sussman, P. Smereka, and S. Osher. A level set approach for computing solutions to incompressible two-phase flow. *J. Comp. Phys.*, 114(1):146 – 159, 1994.

[18] J. A. Sethian and Peter Smereka. Level set methods for fluid interfaces. *Annu. Rev. Fluid Mech.*, 35 (1):341–372, 2003.

[19] C. W. Hirt and B. D. Nichols. Volume of fluid (VOF) method for the dynamics of free boundaries. *J. Comp. Phys.*, 39(1):201 – 225, 1981.

[20] T. Taha and Z.F. Cui. CFD modelling of slug flow inside square capillaries. *Chem. Eng. Sci.*, 61(2): 665 – 675, 2006.

[21] P. Sobieszuk, P. Cygański, and R. Pohorecki. Bubble lengths in the gas–liquid Taylor flow in microchannels. *Chem. Eng. Res. Des.*, 88(3):263 – 269, 2010.

[22] L. Amaya-Bower and T. Lee. Lattice boltzmann simulations of bubble formation in a microfluidic T-junction. *Phil. Trans. R. Soc. A*, 369(1945):2405–2413, 2011.

[23] Ansys Inc. *Ansys Fluent Theory Guide*. Ansys Inc., 2005.

[24] Ansys Inc. *Ansys CFX-Solver Theory Guide*. Ansys Inc., November 2011.

[25] ESI Group. *CFD-ACE V2006 User Manual*. ESI Group, 2006.

[26] OpenCFD Ltd. *OpenFOAM Userguide*. OpenCFD Ltd., 2009.

[27] M. M. Francois, S. J. Cummins, E. D. Dendy, D. B. Kothe, J. M. Sicilian, and M. W. Williams. A balanced-force algorithm for continuous and sharp interfacial surface tension models within a volume tracking framework. *J. Comp. Phys.*, 213(1):141 – 173, 2006.

[28] S. Popinet. An accurate adaptive solver for surface-tension-driven interfacial flows. *J. Comp. Phys.*, 228(16):5838 – 5866, 2009.

[29] S. Afkhami and M. Bussmann. Height functions for applying contact angles to 2D VOF simulations. *Int. J. Numer. Meth. Fluid.*, 57(4):453–472, 2008.

[30] M. Sussman and E. G. Puckett. A coupled level set and volume-of-fluid method for computing 3d and axisymmetric incompressible two-phase flows. *J. Comp. Phys.*, 162(2):301 – 337, 2000.

[31] Sharen J. Cummins, Marianne M. Francois, and Douglas B. Kothe. Estimating curvature from volume fractions. *Comput. Struct.*, 83(6–7):425 – 434, 2005.

[32] S. Afkhami, A. M. Leshansky, and Y. Renardy. Numerical investigation of elongated drops in a microfluidic T-junction. *Phys. Fluids*, 23(2):022002, 2011.

[33] B. Lafaurie, C. Nardone, R. Scardovelli, S. Zaleski, and G. Zanetti. Modelling merging and fragmentation in multiphase flows with SURFER. *J. Comp. Phys.*, 113(1):134 – 147, 1994.

[34] D. Gerlach, G. Tomar, G. Biswas, and F. Durst. Comparison of volume-of-fluid methods for surface tension-dominant two-phase flows. *Int. J. Heat Mass Transfer*, 49(3–4):740 – 754, 2006.

[35] A. Q. Raeini, M. J. Blunt, and B. Bijeljic. Modelling two-phase flow in porous media at the pore scale using the volume-of-fluid method. *J. Comp. Phys.*, 231(17):5653 – 5668, 2012.

[36] H. G. Weller, G. Tabor, H. Jasak, and C. Fureby. A tensorial approach to computational continuum mechanics using object-oriented techniques. *Comp. Phys.*, 12(6):620–631, 1998.

[37] J. U. Brackbill, D. B. Kothe, and C. Zemach. A continuum method for modeling surface tension. *J. Comp. Phys.*, 100(2):335–354, 1992.

[38] H. G. Weller. A new approach to vof-based interface capturing methods for incompressible and compressible flow. Technical report, OpenCFD Ltd., 2008.

[39] E. Berberovic, N. P. van Hinsberg, S. Jakirlić, I. V. Roisman, and C. Tropea. Drop impact onto a liquid layer of finite thickness: Dynamics of the cavity evolution. *Phys. Rev. E*, 79(3):036306, 2009.

[40] S. S. Deshpande, L. Anumolu, and M. F. Trujillo. Evaluating the performance of the two-phase flow solver interFoam. *Comput. Sci. Disc.*, 5(1):014016, 2012.

[41] H. Rusche. *Computational Fluid Dynamics of Dispersed Two-Phase Flows at High Phase Fractions*. PhD thesis, Imperial College of Science, Technology and Medicine, 2002.

[42] J. Eggers and E. Villermaux. Physics of liquid jets. *Rep. Prog. Phys.*, 71(3):036601, 2008.

[43] A. Vrij. Possible mechanism for the spontaneous rupture of thin, free liquid films. *Discuss. Faraday Soc.*, 42:23–33, 1966.

[44] F. P. Bretherton. The motion of long bubbles in tubes. *J. Fluid Mech.*, 10(02):166–188, 1961.

[45] P. Aussillous and D. Quere. Quick deposition of a fluid on the wall of a tube. *Phys. Fluids*, 12(10): 2367–2371, 2000.

[46] V. van Steijn, C. R. Kleijn, and M. T. Kreutzer. Predictive model for the size of bubbles and droplets created in microfluidic T-junctions. *Lab Chip*, 10:2513–2518, 2010.

[47] P.J. Roache. Quantification of uncertainty in computational fluid dynamics. *Annu. Rev. Fluid Mech.*, 29:123–160, 1997.

[48] V. van Steijn, C. R. Kleijn, and M. T. Kreutzer. Flows around confined bubbles and their importance in triggering pinch-off. *Phys. Rev. Lett.*, 103:214501, Nov 2009.

[49] V. S. Ajaev and G.M. Homsy. Modeling shapes and dynamics of confined bubbles. *Annu. Rev. Fluid Mech.*, 38(1):277–307, 2006.

[50] H. Wong, C. J. Radke, and S. Morris. The motion of long bubbles in polygonal capillaries. Part 1. Thin films. *J. Fluid Mech.*, 292:71–94, 1995.

[51] D. Link, S. Anna, D. Weitz, and H. Stone. Geometrically mediated breakup of drops in microfluidic devices. *Phys. Rev. Lett.*, 92(5), 2004.

[52] M. C. Jullien, M. J. Tsang Mui Ching, C. Cohen, L. Menetrier, and P. Tabeling. Droplet breakup in microfluidic T-junctions at small capillary numbers. *Phys. Fluids*, 21(7):072001, 2009.

[53] T. Fu, M. Youguang, D. Funfschilling, and H. Z. Li. Dynamics of bubble breakup in a microfluidic T-junction divergence. *Chem. Eng. Sci.*, 66:4184ï£¡4195, 2011.

3. Dynamics of droplet breakup in a T-junction[§]

The breakup of droplets due to creeping motion in a confined microchannel geometry is studied using 3D numerical simulations. Analogously to unconfined droplets, there exist two distinct breakup phases: (i) a quasi-steady droplet deformation driven by the externally applied flow and (ii) a surface-tension-driven three-dimensional rapid pinching that is independent of the externally applied flow. In the first phase, the droplet relaxes back to its original shape if the externally applied flow stops; if the second phase is reached, the droplet will always break. Also analogously to unconfined droplets, there exist two distinct critical conditions: (i) a condition that determines whether the droplet reaches the second phase and breaks, or it reaches a steady shape and does not break, and (ii) a condition that determines when the rapid autonomous pinching starts. We analyze the second phase using stop-flow simulations, which reveal that the mechanism responsible for the autonomous breakup is similar to the end-pinching mechanism for unconfined droplets reported in the literature: the rapid pinching starts when, in the channel mid-plane, the curvature at the neck becomes larger than the curvature everywhere else. This same critical condition is observed in simulations in which we do not stop the flow: the breakup dynamics and the neck thickness corresponding to the crossover of curvatures are similar in both cases. This critical neck thickness depends strongly on the aspect ratio, and, unlike unconfined flows, depends only weakly on the capillary number and the viscosity contrast between the fluids inside and outside the droplet.

[§]Published as: D. A. .Hoang, L. M. Portela, C. R. Kleijn, M. T. Kreutzer and V. van Steijn. Dynamics of droplet breakup in a T-junction *Journal of Fluid Mechanics*, 717, R4, 2013, doi: 10.1017/jfm.2013.18.

3.1 Introduction

The breakup of droplets in confined geometries, such as found in microfluidic devices with branching networks and in two-fluid flows in porous media, is markedly different from the breakup of droplets in unconfined extensional or straining flows. Relevant questions are the strength of the flow needed to cause breakup and the mechanism by which this occurs.

Literature on unconfined breakup in Stokes flow dates back to pioneering work by Taylor [1], who showed that under steady extensional flow, there exists a critical strain rate G below which a droplet of radius a is extended and assumes a steady elongated shape with a length l, and above which the droplet deforms continuously until it breaks. Expressed as a capillary number $Ca = \mu Ga/\gamma$, where γ is the interfacial tension between the fluids, this critical strain rate, to which corresponds a critical droplet length, depends only on the viscosity contrast $\lambda = \hat{\mu}/\mu$ of the fluids inside and outside the droplet. The fate of droplets that are extended at supercritical strain rates was studied in great detail [2,3] by stretching droplets and suddenly stopping the flow in a computer-controlled four-roll mill. These experiments revealed that there exists a second critical droplet length, beyond which the droplets break even without an external driving flow, and below which droplets relax back to a sphere. This second critical length, again, depends only on the viscosity contrast λ. In fact, Stone's stop-flow experiments revealed many of the relevant and interesting flow features of breaking droplets, such as capillary instabilities similar to the pinching of a cylindrical jet, end-pinching, the formation of satellite droplets, etc., that go far beyond (pseudo-)steady analysis of the maximum strain rate that a droplet can withstand.

A confined geometry that resembles the extensional flows is a T-junction with equal arms into which a long droplet is driven and pushed into both arms. Droplets in the junction then either break up or reach a steady shape; this steady shape might be unstable, in which case the droplet eventually escapes into one of the arms. Link et al. [4] demonstrated that here too, a critical droplet length exists, corresponding to a critical capillary number expressed as $Ca = \mu U/\gamma$, with U the mean velocity flowing into the T-junction. In this confined flow, already on dimensional grounds, the ratio of droplet length to channel width $\epsilon = (l/w)$ is relevant, and experiments indeed reveal that the boundary between breakup and non-breakup regimes has the form $Ca = f(\epsilon, \lambda)$. Link et al. [4] used instability arguments similar to jet-breakup to predict this transition. More in the spirit of Taylor's analysis, Leshansky and Pismen [5] predicted the transition by calculating pseudo-steady droplet shapes using a two-dimensional model in which the capillary instability is not operative. Even though their model cannot possibly capture the complex three-dimensional shape of long confined droplets, their theory successfully predicts, up to an $O(1)$ constant, whether droplets break. However, the mechanisms that govern the dynamics beyond the critical capillary number, i.e. for breaking droplets, have remained unclear. Jullien et al. [6] observed that breaking droplets sud-

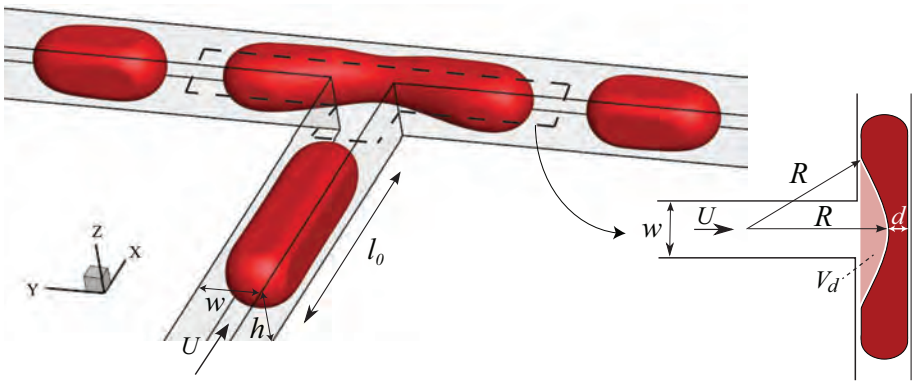

Figure 3.1 Geometry of the problem and top-view of the deforming droplet.

denly pinch, which suggests that confined droplets also exhibit a critical shape beyond which breakup is autonomous. Even though, as we will show here, this second critical shape is not generally the same as the critical shape associated with the question whether a droplet breaks, these shapes are used interchangably in current literature e.g.[6,7]. Similarly to unconfined flows, we use stop-flow numerical experiments to clarify this confusion between steady-state features of confined droplets and the 3D surface-tension-driven mechanisms of rapid pinching.

This chapter explores numerically the fate of droplets in a T-junction, exposed to flow rates above the critical value for breakup. We restrict ourselves to the Stokes flow regime; inviscid breakup dynamics are very different see e.g.[8]. We shall see that the breakup dynamics of these confined droplets in many ways resembles their unconfined equivalent. Of course, the shape of the confining channels is now a relevant parameter, in addition to the viscosity contrast and initial droplet size. In simulations, the stop-flow experiments are feasible with little effort, and reveal many interesting aspects that are difficult if not impossible to observe in physical experiments. Similarly in spirit to Stone's (1986) analysis, we seek to find critical features of the droplet shape that determine when a droplet will breakup autonomously even when the flow is stopped abruptly.

3.2 Problem formulation

Consider the droplet of viscosity $\hat{\mu}$ and density $\hat{\rho}$ in figure 3.1 that flows from a channel of width w and height h into a T-junction with two equal arms of same width w and height h. The droplet is too large to remain spherical inside the channel and has a length $l_0 > w$. It is surrounded by an outer fluid of viscosity μ and density ρ,

which flows through the feed branch of the T-junction with mean velocity U. We use the fluid properties reported by Link et al.[4] and Jullien et al.[6] as a set of base parameters: for the outer fluid $\mu=8\,\mathrm{mPas}$ and $\rho=770\,\mathrm{g/L}$, for the droplet $\hat{\mu}=1\,\mathrm{mPas}$ and $\hat{\rho}=1000\,\mathrm{g/L}$ and $\gamma=5\,\mathrm{mN/m}$. Velocities in the feed channel of cross-section $30\times30\,\mu\mathrm{m}^2$ were varied in the range $U=0.5-17.5\,\mathrm{mm/s}$. We varied the viscosity contrast by changing the droplet viscosity, $10^{-3}<\lambda<10$, and the channel aspect ratio by changing h, $1/3<h/w<1$. Droplet sizes $l_0/w=2.80$, 5.56, 11.1 and ∞ were considered, where $l_0=\infty$ was simulated by filling both branches with the droplet fluid at the start. Resulting Reynolds numbers $Re=\rho U w/\mu$ and capillary numbers were in the range $10^{-3}<Re<10^{-1}$ and $10^{-4}<Ca<10^{-2}$, respectively.

Simulations are performed using the finite-volume-based code OpenFOAM-1.6[9], in which the fluid interface is represented by the volume-of-fluid (VOF) method. We use hexahedral meshes and refine recursively four times the cells adjacent to the wall to resolve the thin lubrication films surrounding the droplet. At the two exits, we prescribe a reference pressure and zero gradient of the volume fraction. At the walls, we apply the no-slip boundary condition and use an equilibrium contact angle $\theta_e=0°$. We initialize the simulation with a rectangular droplet, more than $10w$ upstream of the T-junction,and let the droplet relax to an equilibrium shape. We then start the flow in the feed channel and run until the two daughter droplets start to leave the computational domain, which happens well after the breakup is complete. Details on the numerical methods employed and the validation can be found in chapter 2.

All published experimental data cited above are only available as the evolution of droplet shapes measured from top-view micrographs and as derived parameters, like the thickness of the neck d and the in-plane radius of curvature R, both shown in figure 1. We further detail the process with time and space-resolved velocity and pressure fields, which are difficult to obtain experimentally.

3.3 The mechanism of droplet pinching

3.3.1 Breakup of droplets in T-junctions

We begin by describing the subsequent stages of droplet deformation and flow when a droplet flows into the T-junction. In all cases, the capillary number was well above the critical value for breakup, $Ca=6\times10^{-3}$ for $l_0/w=2.80$, $Ca=2\times10^{-4}$ for $l_0/w=5.56$, similar to $l_0/w\approx0.98Ca^{-0.21}$ from Leshansky and Pismen[5]. We set $Ut/w=0$ at the moment when the droplet has entirely departed from the feed channel. From this moment on, the driving fluid deforms the droplet in the center of the T-junction resulting in a dumbbel-like droplet shape as shown in figure 3.1. The neck connects two half-droplets, which adopt the shape of a semi-infinite droplet in a rectangular channel

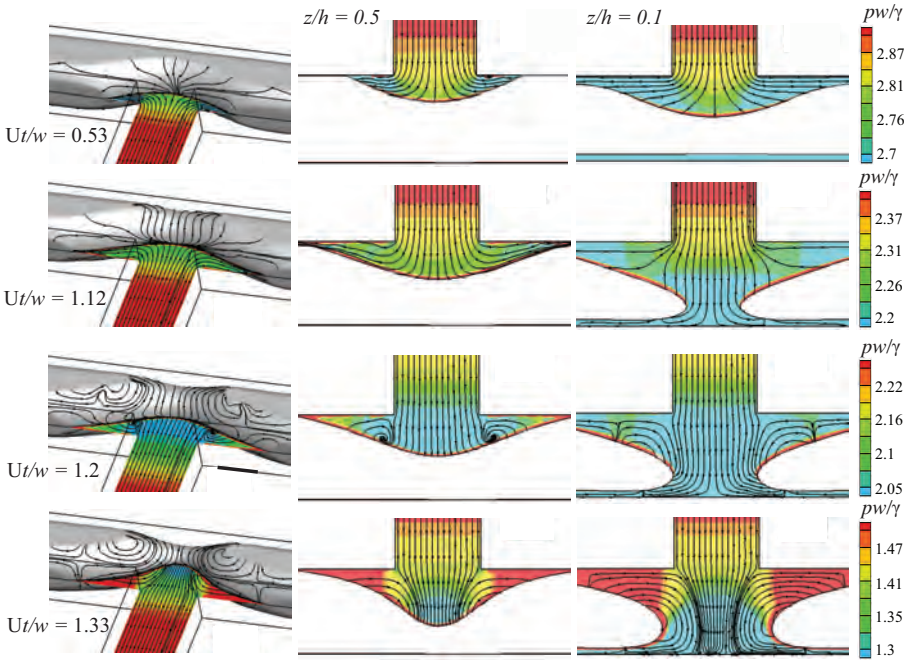

Figure 3.2 Pressure and velocity distribution during the breakup. $Ca = 6.25 \times 10^{-3}$, $Re = 0.01$, $l_0/w = 5.65$, $\lambda = 0.125$, $h/w = 1$.

as described by Wong et al.[10], with a near-flat film surrounding the droplet, except near the corners of the channel where the half-droplets are separated from the wall by a meniscus of radius $r^{-1} \sim 2(w^{-1} + h^{-1})$. Flow of the continuous phase around the droplet predominantly occurs through these corner regions, which we call gutters. Early in the breakup, the neck takes the shape of a circular arc with radius R at the mid-plane of the channel ($z/h = 0.5$) as shown in figure 3.2 for $Ut/w = 0.53$. The apparent macroscopic contact angle follows the theory of the hydrodynamics of wetting[11] as proposed by Leshansky et al.[12]. Once the neck detaches from the top and bottom wall as shown in the $z/h = 0.1$ plane at $Ut/w = 1.12$, the interface no longer assumes a circular arc shape at $z/h = 0.5$. At $Ut/w = 1.33$, the local radius of curvature at the neck further decreases until the droplet breaks into two equal daughter drops. Simulations for different droplet sizes show that the flow features are essentially identical in the center of the T-junction, regardless of the droplet size.

To further our understanding, we turn our attention to the pressure and velocity fields around the neck region as shown in figure 3.2. At first, fluid from the feed channel spreads out to the gutters and pushes the interface inwards to form a necking region. At $Ut/w = 0.53$, the droplet still touches the top and bottom walls in the middle via

a thin lubricating film. At $Ut/w = 0.67$ (not shown in figure 3.2), the driving liquid has sufficiently pushed the neck inwards to detach the droplet from the top and bottom walls. From this moment onwards, the fluid also flows through the opening that forms near the top and bottom walls into the gutters opposite of the feed channel, as shown for $Ut/w = 1.12$; however, the flow in these opposite gutters does not continue to the droplet ends, as can be seen by the stagnation point on the droplet surface. Later, at $Ut/w \approx 1.2$, flow to the gutters adjacent to the feed channel ceases. Pressure builds up where the gutters meet the necking region and liquid starts to flow back to the neck, where the pressure is lower. Still later, at $Ut/w = 1.33$, a flow to the middle of the T-junction is observed from the entrance of all eight gutters, where the total flow in the gutters adjacent to the inlet is 66 times larger than that in the opposite gutters. A stagnation line is found on the droplet surface in the $|y| \approx 1.2w$ plane in both branches. A result of this flow reversal is that the constriction is accelerated, because the incoming fluid can no longer escape.

3.3.2 Three-dimensional effects

A topic of recurring interest has been whether a two-dimensional description of the breakup captures the relevant phenomena. In a two-dimensional analysis, the shape of the lubricating film between the far ends of the breaking droplet and the neck is amenable to a self-similarity analysis, as is the flow through it. Recall that 2D-based predictions of *whether* the droplet breaks up compared favorably with experiments[5,6]. As the 2D lubricating film is thin, flow through it is minimal, and the droplet obstructs flow to the branches. Leshansky et al. [12] used this all but complete obstruction to develop a self-similar description for the breakup dynamics based on the notion that, absent leakage through the film, the depression volume V_d of outer fluid near the neck increases linearly with time. In this analysis, $(1 - d/w) \sim (Ut/w)^{3/7}$, leading to a collapse in a finite time.

We performed two-dimensional simulations, equivalent to the full three-dimensional simulations of breakup described above. Figure 3.3(a) shows the evolution of neck thickness for both the 2D and 3D simulations. In agreement with Leshansky et al. [12], we find that in 2D the thickness of the neck decreases monotonically until a grid-dependent collapse a consequence of the VOF method, see also[13]. The $3/7$ scaling describes the data well, as shown in the inset. The 3D evolution follows the 2D data very closely until $d/w \approx 0.5$. In fact, in 3D, $d/w \approx 1 - 0.58(0.25/3Ca)^{-1/7}(Ut/w)^{3/7}$, as in 2D. This agreement teaches that in the early stages of breakup, flow past the semi-obstructing ends is similar in 2D and 3D, with negligible influence of the Laplace pressure due to the out-of-plane curvature, $p \sim \gamma/d$, on the droplet surface at the neck. This, and the small influence of the flow through the gutters, explains why the two-dimensional theory to predict whether a droplet breaks works well in three dimensions: as is the case for unconfined flows, the maximum steady-state droplet

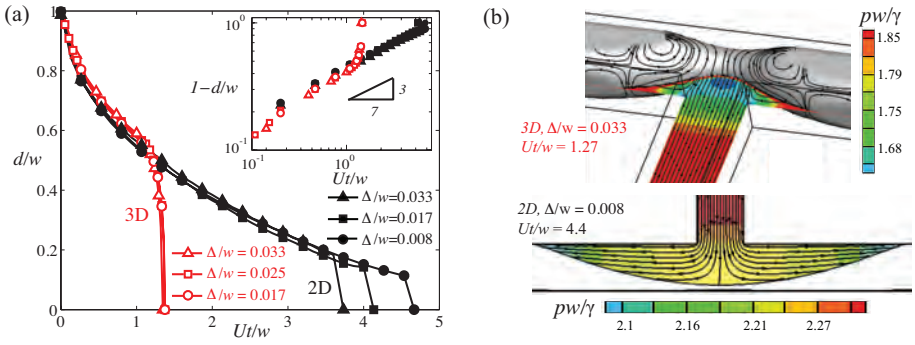

Figure 3.3 (a) Evolution of the neck thickness in 3D (red-open symbols) and 2D (black-closed symbols) for different grid resolutions Δ ($h/w=1$, $\lambda=0.125$, $l_0/w=5.56$ and $Ca=6.25\times 10^{-3}$). Inset: the same data as $\log(1-d/w)$ vs. $\log(Ut/w)$. (b) Pressure and velocity field of 3-D and 2-D simulations just before pinch-off.

deformation is moderate, with, in fact, $d/w\approx 0.5$ as the maximum deformation[5].

Three-dimensional capillary effects do significantly influence the breakup dynamics for $d/w<0.5$. In 3D, the grid-independent accelerated pinch-off happens well before the 2D breakup. The neck starts to collapse at $d/w\approx 0.5$, initiating a very fast second phase, resulting in a break-up at $Ut/w=1.37$, much faster than the 2D value at $Ut/w=3.54(0.25/3Ca)^{1/3}=8.39$[12]. As a result, the depression volume $V_d\sim t$ remains small and the range of droplet lengths for which a "tunnel" opens during the breakup (the "non-obstructed" regime) is smaller than predicted for 2D. The evolution of d/w with tunnel opening ($l_0/w=2.80$) was identical to that without tunnel opening ($l_0/w=5.56$). More importantly, the smaller break-up time can be compared to the time it takes a droplet to move, partially or entirely, into either branch because of slight imperfections of the symmetry of T-junctions in experiments. The shorter breakup time in 3D results, for a given device, in less asymmetry in the volume of the daughter droplets than would be predicted on 2D theory[14].

Figure 3.3(b) shows when the 2D and 3D dynamics diverge prior to pinch-off. In 3D, the effect of curvature on the pressure field leads to back flow, whereas in the 2D simulation flow towards the two exits of the T-junction persists until breakup, even if that flow is small. For the case considered here with $h/w=1$, the critical value of the neck thickness at the onset of the rapid collapse agrees well with the critical value $d/w=\frac{1}{2}$ for a continuous steady-state deformation as calculated by Leshansky and Pismen[5]. As we will discuss below, this result is not generic. In fact, as in unconfined flow[2] Figure 12, there exist two different critical values: (i) a value that determines whether the droplet deforms continuously, eventually leading to breakup, and (ii) a value that determines the onset of the rapid collapse. Before we discuss features of

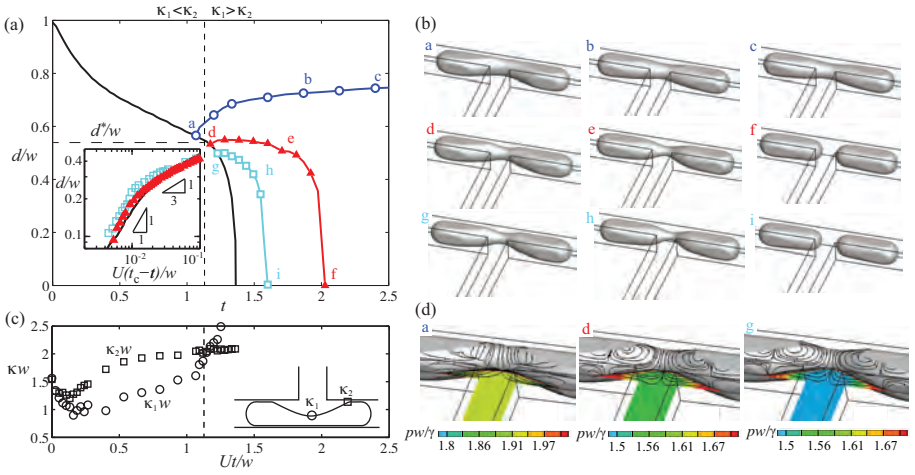

Figure 3.4 (a) Evolution of the neck thickness in continuous (solid black line) and stop-flow simulations (symbols). Inset: $\log(d/w)$ vs. $\log(U(t_c-t)/w)$. (b) Droplet shapes in stop-flow simulations. (c) Evolution of the curvature at indicated locations in the continuous simulation. (d) Pressure and velocity field immediately after the start of the stop-flow simulations. (Parameters as in figure 3.3(*a*).)

this second critical neck thickness, we first show how it can be determined from stop-flow simulations.

3.3.3 Stop-flow simulations

We now seek to find the critical features of the droplet shape that determine whether a droplet will breakup autonomously when the flow is stopped abruptly. As it turns out, the corresponding neck thickness is the same as the critical neck thickness at the onset of rapid collapse. Our starting point is a continuous simulation on droplet breakup (black line in figure 3.4(*a*)). In the stop-flow simulations, we extract the shape of the continuous simulation at different instances and then set the velocity everywhere in the domain equal to zero, keeping the pressure at the outlet constant throughout. We then restart the simulation, which now describes the flow driven by capillary effects alone.

In a first simulation, stopped at $Ut/w = 1.07$, the droplet relaxes back to the original shape (circles, blue line in figure 3.4(*a*) and the droplet shapes (a)-(c) in figure 3.4(*b*)). Absent the driving fluid coming into the T-junction, this process is dominated by the slow flow through the gutters and the droplet reaches its relaxed shape only at $t \gg 1$. The situation is markedly different for a second simulation, stopped at $Ut/w = 1.17$

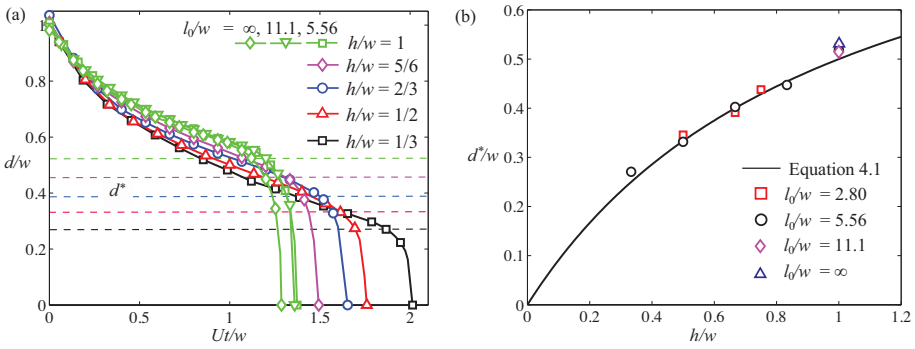

Figure 3.5 (a) Evolution of the neck thickness in T-junctions with different height-to-width ratios h/w. ($l_0/w=5.56, 11.1$ and ∞, $Ca=6.25\times10^{-3}$). (b) Critical neck thickness d^*/w vs. h/w. ($l_0/w=5.56$, $Ca=6.25\times10^{-3}$) and ($l_0/w=2.80$, $Ca=0.01$).

(triangles, red line, shapes (d)-(f)), where the neck first increases slightly, followed by a gradual decrease and a rapid collapse. In a third simulation, stopped at $Ut/w=1.23$, this initial increase is absent (squares, light blue line, shapes (g)-(i)), but the final rate $\partial d/\partial t$ of the rapid collapse is similar and equals the rate of the final collapse in case the flow is not stopped. The neck scales with $(U(t_c-t)/w)^\alpha$, where t_c is the pinch-off time, with an exponent α which changes from $\alpha\approx\frac{1}{3}$ at $d/w=0.3$ to $\alpha\approx1$ at $d/w=0.1$, which was smallest neck size that we could resolve our grid, indicating that a (inertial-) viscous-capillary balance is operative in the final stages[8]. Figure 3.4(*d*) shows that stagnation lines on the interface immediately appear for the two stop-flow simulations that lead to breakup, in contrast to the simulation that relaxes back to a single droplet. This highlights the importance of the flow of the outer fluid for the rapid pinch in the center. The three stop-flow simulations, taken together, show that once the neck thins beyond a critical value (here, $d^*/w=0.53$ at $Ut/w=1.1$), droplet breakup is inevitable. This transition between relaxation and breakup coincides with the start of the rapid collapse for the simulation in which the flow persists, as marked by the point of departure from the line $(1-d/w)\sim(Ut/w)^{3/7}$ in the inset of figure 3.3(a). Similarly to droplets that break without further external strain in unconfined flows[2], confined droplets break due to a surface-tension-driven mechanism. Following Stone's analysis on the droplet shape after stopping the flow, we note that droplets relax when, in the channel mid-plane, the local curvature at the neck, κ_1, is smaller than the curvature everywhere else, such that the surrounding liquid flows away from the neck. By contrast, droplets break when the curvature at the neck is larger than the curvature everywhere else. The comparison between κ_1 and the curvature κ_2 at the entrance of the gutter shows that, indeed, $\kappa_1-\kappa_2$ reverses sign at the transition between breaking and non-breaking drops (Figure 3.4c). The only difference between Stone's analysis and our analysis is that the location of the maximum curvature is off-center for uncon-

fined droplets, such that they break into at least three fragments. In fact, the confining geometry prevents the formation of the large bulbous ends, and the inflow at the center forces the pinch in the middle. Despite this slight difference, our work clearly shows that it is the shape of the droplet alone that drives the pinching: the breakup mechanism is similar to the end-pinching mechanism proposed by Stone et al.[2] for unconfined droplets.

3.4 Critical shape for autonomous pinching

We now explore how the critical shape for autonomous breakup d^*, which coincides with the point of departure from 2D-like behavior, depends on the confining geometry. Simulations (continuous and stop-flow) in channels with height-to-width ratios between 1/3 and 1 show the dependence of d^*/w on h/w as evident from a comparison of the evolution of the neck thickness in figure 3.5(*a*). A reduction in h/w reduces d^*/w, postponing the onset of the rapid collapse Ut^*/w. We note that both d^*/w and $d(t)/w$ are rather insensitive to droplet length. More quantitatively, we found that all data ($0.33 < h/w < 1$ and $l_0/w \geq 2.80$) follows the simple relation

$$\frac{d^*}{w} = \frac{h}{h+w} \tag{3.1}$$

as shown in figure 3.5(*b*). This relation was previously developed for the rapid collapse of the neck of droplets forming in T-junctions[15] suggesting that similar mechanisms are at play.

Unlike unconfined droplets, the shape of the droplet at $t = t^*$ is almost independent of the viscosity contrast and the capillary number. Consequently, we expect d^*/w to be insensitive to both these parameters. Indeed, a comparison of the neck evolution in channels with $h/w = 1$ shows that d^*/w only slightly depends on *Ca* (inset of figure 3.6(*a*)), with a decrease in d^*/w of 15% over the two orders of magnitude increase of *Ca* ($9 \times 10^{-4} < Ca < 2.8 \times 10^{-2}$). These results are in line with the experimental observations by Jullien et al.[6] and Fu et al.[7]. To study the influence of the viscosity contrast, we varied the viscosity of the droplet $\hat{\mu}$ while keeping the viscosity of the surrounding fluid μ constant. Figure 3.6(*b*) shows that the onset of rapid pinching does not change with λ. The rate of the pinching decreases with increasing λ, and the exponent in $d/w \sim (U(t_c - t)/w)^{\alpha}$ tends to $\alpha = 1$. One would expect asymmetry in the pinching for two viscous fluids[8], but for the neck sizes that we could resolve we did not observe that[8,16]. Due to the higher droplet viscosity, the pinching time increases, by a factor 1.4 going from $\lambda = 0.001$ to $\lambda = 1$ and by a factor 2.4 by going from $\lambda = 1$ to $\lambda = 10$.

We now return to the discussion on the two critical shapes in the breakup of confined droplets. By calculating steady-state shapes without regarding dynamics, Leshansky

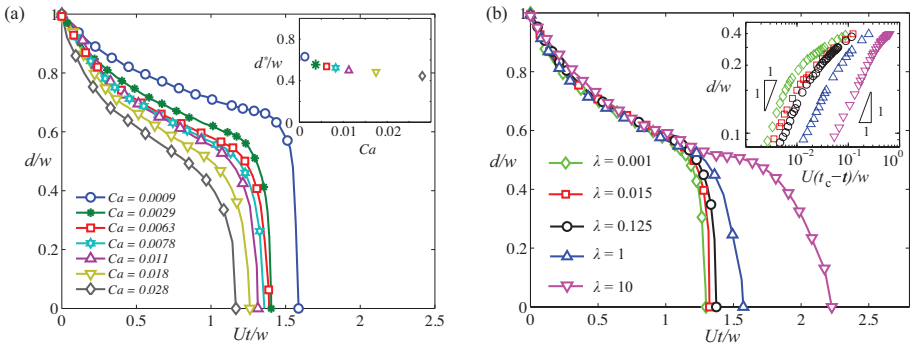

Figure 3.6 (a) Influence of the capillary number $9\times10^{-4}<Ca<2.8\times10^{-2}$ on the evolution of the neck thickness. Inset: d^* vs. Ca. ($h/w=1$, $l_0/w=5.65$, $\lambda=0.125$) (b) Influence of the viscosity contrast $0.001<\lambda<10$ on the evolution of the neck thickness. ($h/w=1$, $l_0/w=5.65$, $Ca=6.25\times10^{-3}$) Inset: $\log(d/w)$ vs. $\log(U(t_c-t)/w)$.

and Pismen[5] showed that the first critical droplet shape, which determines whether a droplet breaks, has a neck thickness $d/w=0.5$. Even though the second critical droplet shape, beyond which the droplets break autonomously at supercritical velocities, roughly coincides with the first at $h/w=1$, this result is certainly not general. Our simulations show that the second critical drop shape, though insensitive to Ca and λ, strongly depends on the aspect ratio of the channel h/w.

3.5 Concluding remarks

We have presented a numerical study on the breakup of droplets confined in a T-junction using full simulations and stop-flow simulations. While stop-flow experiments are notoriously difficult to perform in microfluidic devices, numerical experiments are easily done. Our simulations reveal that the breakup mechanism shows similarities with the breakup of unconfined droplets. The breakup process comprises two distinct phases: in the first phase the droplet goes through a quasi-steady deformation, driven by the externally applied flow, while in the second phase a surface-tension-driven three-dimensional rapid autonomous pinching occurs that is independent of the externally applied flow. The rapid autonomous pinching starts when, in the channel mid-plane, the curvature at the neck rises above the curvature everywhere else. The onset of this pinching depends strongly on the aspect ratio of the confining channel, however, unlike unconfined droplets, it depends only slightly on Ca and λ. This can be understood from the fact that the rapid autonomous pinching is solely driven by the shape of the droplet, which strongly depends on the aspect ratio of the channel, but,

contrary to unconfined flows, hardly depends on *Ca* and λ.

It is important to note that all droplets studied in this chapter break in case we do not stop the flow, i.e., we study the dynamics of droplets at supercritical velocities both in the "obstructed" and"non-obstructed" regime. The critical shape characterized by d^* corresponds to the onset of the rapid collapse, it does not correspond to the critical shape associated with the question of whether the droplets break, as addressed by Link et al. [4] and Leshansky and Pismen [5]. Our work reveals that the two critical values for the neck thickness only closely match in channels with an aspect ratio $h/w = 1$ and it clarifies why these two should not be used interchangeably for $h/w \neq 1$.

Bibliography

[1] G. I. Taylor. The formation of emulsions in definable fields of flow. *Proc. R. Soc. Lond. A*, 146 (A858):0501–0523, 1934.

[2] H. A. Stone, B. J. Bentley, and L. G. Leal. An experimental study of transient effects in the breakup of viscous drops. *J. Fluid Mech.*, 173:131–158, 1986.

[3] H. A. Stone and L. G. Leal. Relaxation and breakup of an initially extended drop in an otherwise quiescent fluid. *J. Fluid Mech.*, 198:399–427, 1989.

[4] D. Link, S. Anna, D. Weitz, and H. Stone. Geometrically mediated breakup of drops in microfluidic devices. *Phys. Rev. Lett.*, 92(5), 2004.

[5] A. M. Leshansky and L. M. Pismen. Breakup of drops in a microfluidic T junction. *Phys. Fluids*, 21 (2):023303, 2009.

[6] M. C. Jullien, M. J. Tsang Mui Ching, C. Cohen, L. Menetrier, and P. Tabeling. Droplet breakup in microfluidic T-junctions at small capillary numbers. *Phys. Fluids*, 21(7):072001, 2009.

[7] T. Fu, M. Youguang, D. Funfschilling, and H. Z. Li. Dynamics of bubble breakup in a microfluidic T-junction divergence. *Chem. Eng. Sci.*, 66:4184ï£¡4195, 2011.

[8] J. Eggers and E. Villermaux. Physics of liquid jets. *Rep. Prog. Phys.*, 71(3):036601, 2008.

[9] H. G. Weller, G. Tabor, H. Jasak, and C. Fureby. A tensorial approach to computational continuum mechanics using object-oriented techniques. *Comp. Phys.*, 12(6):620–631, 1998.

[10] H. Wong, C. J. Radke, and S. Morris. The motion of long bubbles in polygonal capillaries. Part 1. Thin films. *J. Fluid Mech.*, 292:71–94, 1995.

[11] L. H. Tanner. The spreading of silicone oil drops on horizontal surfaces. *J. Phys. D: Appl. Phys.*, 12 (9):1473, 1979.

[12] A. M. Leshansky, S. Afkhami, M.-C. Jullien, and P. Tabeling. Obstructed breakup of slender drops in a microfluidic T junction. *Phys. Rev. Lett.*, 108:264502, Jun 2012.

[13] S. Afkhami, A. M. Leshansky, and Y. Renardy. Numerical investigation of elongated drops in a microfluidic T-junction. *Phys. Fluids*, 23(2):022002, 2011.

[14] A. Bedram and A. Moosavi. Droplet breakup in an asymmetric microfluidic T junction. *Eur. Phys. J. E*, 34:78, 2011.

[15] V. van Steijn, C. R. Kleijn, and M. T. Kreutzer. Flows around confined bubbles and their importance in triggering pinch-off. *Phys. Rev. Lett.*, 103:214501, Nov 2009.

[16] D. T. Papageorgiou. On the breakup of viscous liquid threads. *Phys. Fluids*, 7(7):1529–1544, 1995.

4. Critical behavior of droplet breakup in T-junction microchannel

The critical behavior of droplet breakup in T-junction mirochannels is studied using three-dimensional numerical simulations. Two scenarios can happen when a droplet flows into a T-junction: (i) if the flow is strong enough, it breaks into two daughter droplets and (ii) otherwise, it drifts away into one branch of the T-junction owing to flow perturbations. Whether a droplet breaks or not is determined by the ratio between two timescales: breakup time and drifting time. Symmetric-boundary-condition simulations allow us to study the breakup time without any flow perturbations, thus to accurately compute the critical capillary number below which the droplet does not break. We study the drifting using full-T-junction simulations, identifying three phases in drifting process: (i) an exponential drifting, (ii) a transition phase and (iii) a linear drifting. Combining the understanding of the breakup and drifting behavior, we found that the critical capillary number below which the droplet drifts away increases more than 10% with respect to the one obtained in free-perturbation flow systems.

4.1 Introduction

Microdroplets have emerged as a controlled way to transport fluid samples in microfluidic networks for lab-on-a-chip applications[1–3]. The presence of these droplets enhances the mixing[4] and heat and mass transfer[5], as well as reduces the axial dispersion[6]. The size of droplets is relevant as it directly relates to the concentration of the sample they contain. In addition, the size plays an important role in the transportation of droplets in microfluidic systems, as it determines the resistance-to-flow. Several basic "unit operations" have been proposed and tested for the precise control and manipulation of the droplet size.

One of the basic "unit operations" in droplet microfluidics is droplet breakup in a T-junction in which droplets of controllable sizes are generated by breaking a big droplet into smaller droplets whose sizes depends on the ratio between the lengths of two branches of the T-junction. Depending on the capillary number ($Ca = \mu U/\gamma$ with μ the viscosity, U the mean flow velocity and γ the interfacial tension), the ratio between the droplet length and the channel width l/w and the viscosity ratio $\lambda = \hat{\mu}/\mu$ ($\hat{\mu}$ is the viscosity of the droplet phase), two scenarios can happens: (i) under a super-critical flow, the droplet breaks into two daughter droplets and (ii) under a sub-critical flow, the droplet does not break and might drift away into one branch of the T-junction.

Several attempts have been made to predict the critical breakup condition at which the behavior changes from breaking to non-breaking[7–11]. Leshansky and Pismen[7] developed a two-dimensional steady-state model to predict the critical capillary number using lubrication analysis in a narrow gap between droplets and channel walls where the interfacial tension force balances with the viscous force. According to their model, there exists a steady state for a droplet under the sub-critical flow. Available experiments demonstrated that the model by Leshansky and Pismen[7] sucessfully predicts, up to an $O(1)$ constant, whether droplets break[9–11]. However, in these experiments, non-breaking droplets do not reach the steady state but drift away into one branch of the T-junction owing to random perturbation in the system[8–11]. Zhang and Wang[11] also showed that, close to the transition line, an asymmetric breakup can happen in a symmetric T-junction due to the drifting. A comprehensive picture of the dynamics of the droplets approaching the critical breakup condition is important to reveal the mechanism of the drifting and the asymmetric breakup observed in physical experiments. Understanding the critical behavior of droplet breakup close to the transition line also helps to unravel the relation between the breakup condition and the ratio of the timescales for breaking and drifting.

The aim of this chapter is to numerically study the critical breakup condition by comparing the two timescales: breakup time and drifting time. We first analyze the timescale for breaking and the steady shape of droplets for different capillary numbers. In this set of simulations, we enforced the same flow conditions in two branches

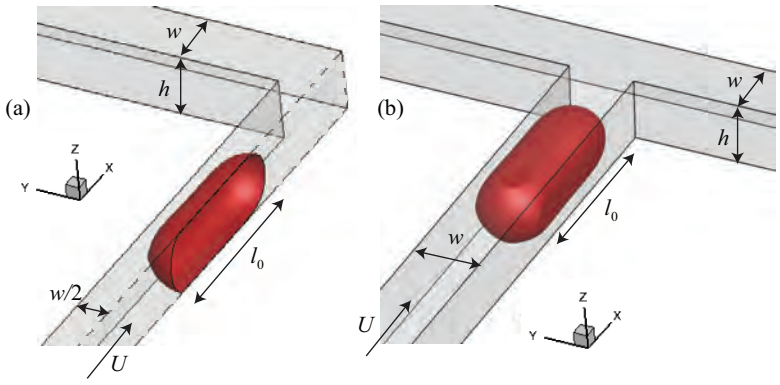

Figure 4.1 Geometries of the problems: (a) A half of a T-junction with a symmetric plane at $y=0$ (b) An entire T-junction.

of a T-junction by applying symmetric boundary condition to suppress flow asymmetry. This allows us to reveal accurate critical capillary numbers of the breakup and the sub-critical steady shape of droplets that are difficult to obtain in physical experiments. We then explore the timescale for drifting in the sub-critical conditions with a full T-junction. Different from the symmetric-boundary-condition simulations, a drifting can happen due to a flow difference between two branches of the T-junction arising from numerical perturbation. We also investigate the influence of a prescribed pressure difference between two outlets on the drifting behavior of the droplet. Combining the understanding of the breakup and drifting behavior, we are able to determine the critical condition for droplet breakup. Furthermore, it teaches us how close to the transition regime, the timescales of the breakup and drifting become comparable, leading to an asymmetric breakup.

4.2 Numerical setup

We investigated the dynamical behavior of droplets of viscosity $\hat{\mu}$, density $\hat{\rho}$ and length l_0 that is enclosed by an outer fluid of viscosity μ and density ρ. Two droplet lengths $l_0 = 59\,\mu\mathrm{m}$ and $84\,\mu\mathrm{m}$ were considered. Fluid properties were selected such that they represent the case often encountered in lab-on-a-chip devices: for the outer fluid $\mu =$ $8\,\mathrm{mPas}$ and ρ=$770\,\mathrm{g/L}$, for the droplet $\hat{\mu}$=$1\,\mathrm{mPas}$ and $\hat{\rho}$=$1000\,\mathrm{g/L}$ and γ=$5\,\mathrm{mN/m}$. We explored the breakup in two types of computational domains, as shown in figure 4.1. A half of a T-junction with a symmetric plane at $y=0$ (figure 4.1(a)) allows us to accurately compute a breakup time and the steady droplet shape without any flow perturbations, while an entire T-junction (figure 4.1(b)) was used to study the drifting behavior. Both geometries have the same dimensions: width $w = 30\,\mu\mathrm{m}$ and height

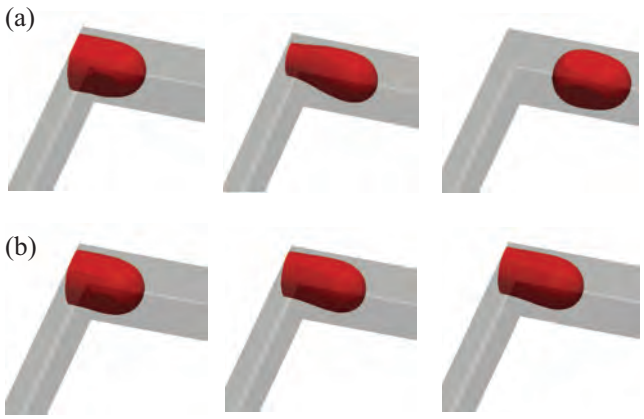

Figure 4.2 Snapshots of droplet shapes in half-T-junction simulations: (a) breaking regime and (b) non-breaking regime.

$h=30\,\mu\mathrm{m}$. Velocities in the main channel were varied in the range $U=0.5-30\,\mathrm{mm/s}$. The corresponding Reynolds numbers $Re=\rho U w/\mu$ and capillary numbers were in the range $10^{-3}<Re<10^{-1}$ and $8\times10^{-3}<Ca<8\times10^{-2}$. The initial time $Ut/w=0$ of the breakup and drifting process is set to the moment when the droplet has entirely exited the feed channel.

The finite-volume-based open-source CFD code OpenFOAM-dev1.6[12] with the Volume of Fluid method (VOF) was used to perform three-dimensional, dynamic simulations. Details on the employed numerical methods and the validation can be found in chapter 2. In all of our simulations, no-slip and zero contact angle boundary conditions were specified at the channel walls. A uniform velocity was applied at the inlet and an atmospheric pressure boundary condition and zero-gradient for the VOF function were applied at the outlets. In symmetric-boundary-condition simulations, a symmetric-plane boundary condition was applied at the plane $y=0$. The simulations ran in parallel on 8 to 16 processors on a Beowulf Linux cluster. The typical wall-clock computational time is approximately 150 hours for one simulation. Local grid refinement was used to resolve the thin lubrication film surrounding the non-wetting bubbles[13]. We have checked that the volume of the droplet phase is conserved during the entire simulations.

4.3 Breakup behavior approaching critical condition

We first study the critical breakup conditions and the timescale for breaking using a half of a T-junction, as shown in figure 4.1(a). In this set of simulations, we applied

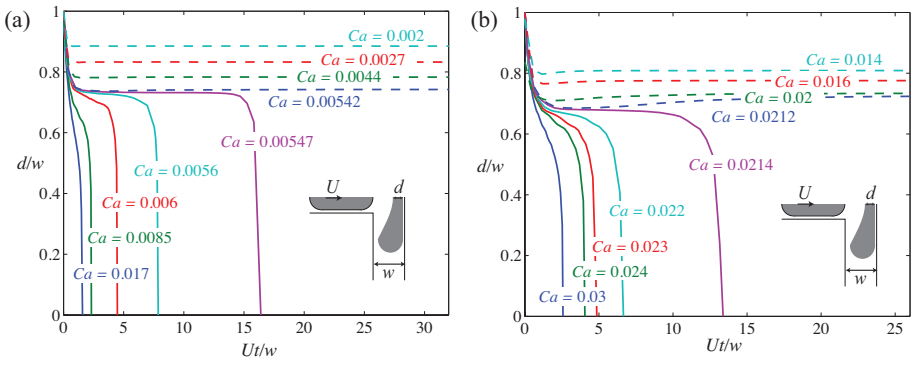

Figure 4.3 Evolution of dimensionless neck thickness d/w for two droplet sizes (a) $l_0/w = 2.8$ and (b) $l_0/w = 2.0$ for different capillary numbers.

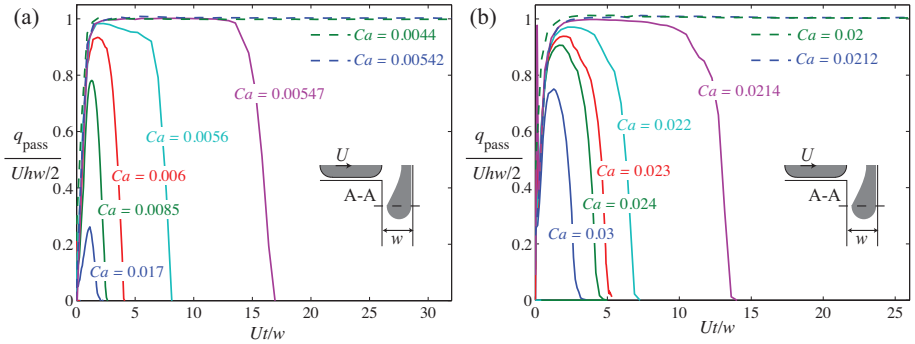

Figure 4.4 Dimensionless flow rate of the external fluid passing droplets through the cross section A-A for two droplet sizes (a) $l_0/w = 2.8$ and (b) $l_0/w = 2.0$ for different capillary numbers.

a symmetric boundary condition (BC) at the plane $y = 0$. This eliminates any flow asymmetries appearing in the system and thus allows us to accurately seek the breakup time and the critical capillary numbers. Preventing the flow asymmetry also allows the computation of the steady shape of the droplets in non-breaking regime, as described by Leshansky and Pismen [7]. Consider a droplet flowing in a junction, figure 4.2 shows two scenarios that can happen in the system: (i) in breaking regime, a droplet enters the branch of the T-junction and is squeezed by the external flow until breakup and (ii) in non-breaking regime, a droplet enters the branch of the T-junction and is also squeezed by the external flow until reaching its steady-state shape. In the second scenario, the external flow entirely passes over the droplet towards the branches of the T-junction - which we will refer as passing flow from now on - and the droplet can

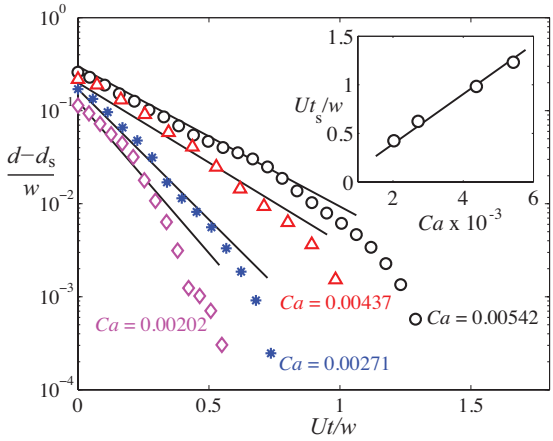

Figure 4.5 Plot of $(d-d_s)/w$ versus Ut/w for different capillary numbers for $l_0/w=2.8$. The inset shows the convergence time at $(d-d_s)/w=10^{-3}$ as a function of the capillary number. The lines are added to guide the eye.

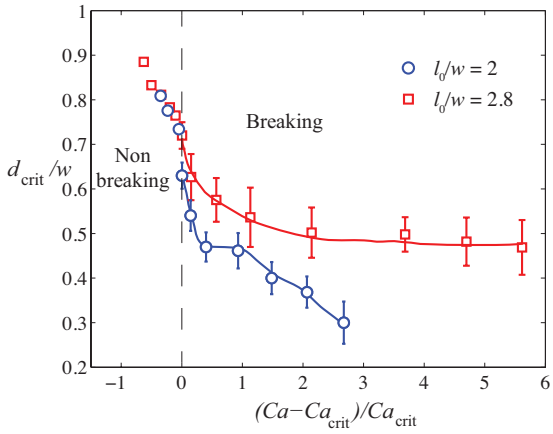

Figure 4.6 Dimensionless critical neck thickness d_{crit}/w at the steady state and at the onset of the rapid pinching for two droplet lengths: $(l_0/w=2.8; Ca_{crit}=0.00545)$ and $(l_0/w=2; Ca_{crit}=0.0213)$. The lines are added to guide the eye.

keep its steady shape indefinitely.

To seek the critical condition for the breakup, we performed simulations with a wide range of the capillary numbers $(2\times10^{-3}<Ca<8\times10^{-2})$. We varied the capillary number by changing the mean flow velocity U, focusing on the transition regime to accurately compute critical capillary numbers. Figure 4.3 shows the evolution of

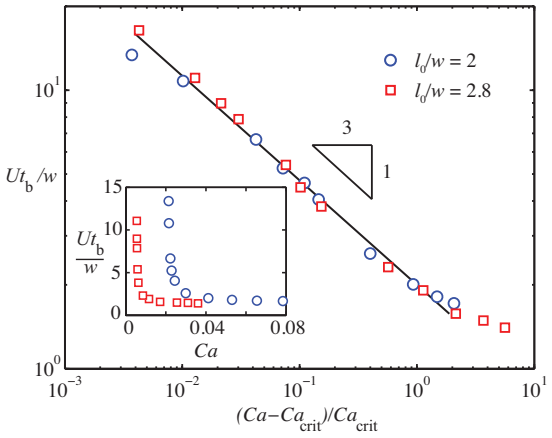

Figure 4.7 Dimensionless breakup time Ut_b/w when the capillary number approaches the critical value for two droplet lengths: ($l_0/w = 2.8$; $Ca_{crit} = 0.00545$) and ($l_0/w = 2$; $Ca_{crit} = 0.0213$). The line is added to guide the eye and to show the fitted scaling $Ut_b/w \sim (Ca/Ca_{crit} - 1)^{-1/3}$. The inset shows the dimensionless breakup time versus capillary numbers.

the dimensionless neck thickness d/w versus the dimensionless time Ut/w for two droplet lengths l_0/w=2.8 and 2.0. The critical capillary numbers of these two droplet lengths are $5.45 \times 10^{-3} \pm 0.02 \times 10^{-3}$ and $2.13 \times 10^{-2} \pm 0.01 \times 10^{-2}$, respectively.

In non-breaking regime (dashed lines in figure 4.3), the droplet enters the branch of the T-junction; it is squeezed shortly until reaching the steady shape. Since there is no flow asymmetry in the system, this steady shape is preserved and the droplet stays at the center of the T-junction. A measurement of the passing flow rate, rescaled with the flow rate at the inlet $Uhw/2$, in time shows that the ratio between the injected flow rate and the passing flow rate reaches unity when the droplet reaches its steady shape (dashed lines in figure 4.4). Our results also show that the steady neck thicknesses at the capillary number just below the critical value are 0.74 ± 0.025 for l_0/w=2.8 and 0.72 ± 0.025 for l_0/w=2. These values are different than the prediction by Leshansky and Pismen [7] ($(d_s/w)_{crit} = 0.5$). The difference might come from the three-dimensional effects that were not taken into account in their model.

Figure 4.5 shows the convergence rate to the steady state of the neck thickness for different capillary numbers for $l_0/w = 2.8$. Our results show that for lower capillary number, the droplet reaches its steady shape faster. The convergence time at which $(d - d_{steady})/w = 10^{-3}$ is linearly proportional to the capillary numbers. In the initial stage, the neck thickness seems to converge exponentially in time towards the steady state.

Further increase of the capillary number leads to the transition between non-breaking and breaking regimes. The solid lines in figure 4.3 and 4.4 show the behavior of the dimensionless neck thickness and passing flow rate during the breakup process. As described in chapter 3, the droplet goes through two phases, squeezing and rapid-pinching, during the breakup. The timescale for breaking is determined by the squeezing rate and the onset of the rapid-pinching.

The squeezing rate is controlled by the amount of fluid passing over the droplet. For the relatively short droplet considered in this chapter, the external fluid pass over the droplet via both the lubrication film between the droplet and the channel walls and the gutters - the corners of the channel that are not filled by the droplet phase. We noticed that the flow via the gutters is approximately ten times larger than the flow via the lubrication film. Hence, the passing flow rate depends primarily on the length of the gutters. During the squeezing phase, the droplet is squeezed by the external flow at its center, resulting in a decrease in the gutter length. Figure 4.4 shows that the passing flow rate increases in the initial stage of the squeezing phase owing to the decreased gutter length. It goes through a maximum and slightly decreases until the rapid pinching kicks in. Our results show that the maximum passing flow rate increases with decreasing capillary number. We found that this flow rate varies with the capillary number in the form: $(q_{pass}/Uhw)_{max} \sim Ca^{-\alpha}$, where $\alpha = 1.95$ and 1.1 for $l_0/w = 2.8$ and $l_0/w = 2.0$, respectively. We observed that the ratio between the passing flow rate and the injected flow rate approaches unity when the flow approaches the critical condition. For ($Ca < 6 \times 10^{-3}$;$l_0/w = 2.8$) and ($Ca < 0.023$;$l_0/w = 2.0$), more than 90% of the injected flow escapes via the gutter. A consequence of the increased passing flow is a decrease of the squeezing rate, leading to an increase of the breakup time.

The onset of the rapid pinching is marked by an accelerated decrease of the neck thickness, as shown in figure 4.3. In chapter 3, we showed that this rapid pinching is governed by interfacial tension forces. At the onset of the rapid pinching, there is by a flow reversal from the entrance of the gutters - the corners of the channel that are not filled by the droplet phase - to the center of the droplet (see figure 3.2). Due to this flow reversal, no fluid can escape via the gutter. Figure 4.4 shows that indeed the onset of the rapid-pinching coincides with the moment that the gutter flow rate starts decreasing rapidly. To quantify the dependence of the onset of the rapid-pinching on the capillary number, we measured the critical neck thicknesses d_{crit}/w at which the rapid-pinching starts. Figure 4.6 shows a plot of these critical neck thicknesses together with the neck thicknesses at the steady state as a function of the capillary numbers. For $l_0/w = 2.8$, the critical neck thickness is 0.5 ± 0.03 in super-critical flows ($(Ca - Ca_{crit})/Ca_{crit} > 1.1$), in agreement with the prediction of the critical neck thickness for square channel in chapter 3. As the capillary number approach the critical value ($0 < (Ca - Ca_{crit})/Ca_{crit} < 1.1$), the critical neck thickness increases from 0.53 to 0.72. For $l_0/w = 2.0$, similar behavior of the critical neck thickness was

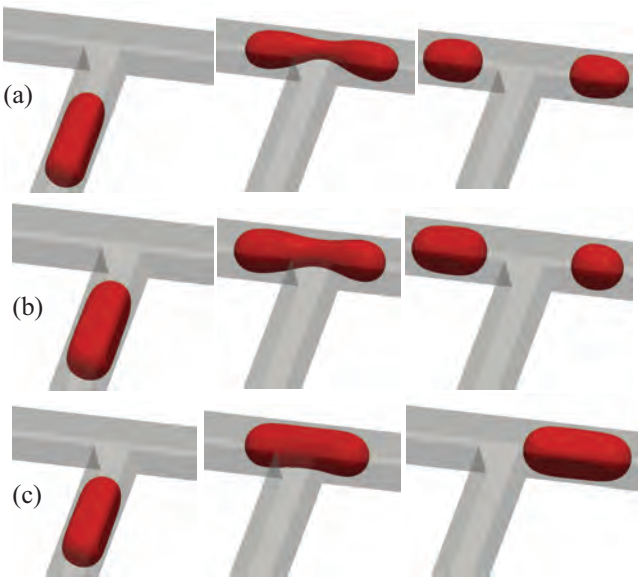

Figure 4.8 Snapshots of droplet shapes in full-T-junction simulations: (a) symmetric breakup, (b) asymmetric breakup and (c) drifting.

observed except for high capillary numbers. Our results show that the critical neck thickness starts deviating from the predicted value of 0.5 at $(Ca-Ca_{crit})/Ca_{crit}=1$, corresponding to $Ca=0.041$. It could be that at such high capillary numbers, the viscous forces become more relevant and the breakup is not fully governed by the interfacial tension forces, leading to a deviation from our analytical prediction.

To further our understanding on the timescale for breaking, we recorded the breakup times and plotted them against the capillary numbers, as shown in figure 4.7. The breakup time increases towards infinity as the capillary approaches the critical value. We found that the breakup time Ut_b/w scales with $(Ca/Ca_{crit}-1)^{-1/3}$ for both droplet lengths. We do not have an explanation for this scaling law yet. This scaling seems to be invalid for the capillary number far from the critical value. For $(Ca-Ca_{crit})/Ca_{crit}>2$, the breakup time starts deviating from this scaling law. Our result suggests an universal law of the variation of the breakup time. However, it is difficult to draw a firm conclusion with only two droplet lengths considered in this chapter.

4.4 Drifting behavior approaching critical condition

We now turn the discussion to the drifting behavior of droplets when the capillary number approaches the critical value. Due to flow asymmetries, the droplet position is not stable and the droplet will drift away into one branch of the T-junction. This flow asymmetries can be caused by the fabrication tolerance of the devices or the pressure fluctuations in the system[14]. To simulate the drifting behavior, we performed simulations with a full T-junction, as shown in figure 4.1(*b*). Here, the flow asymmetry comes from numerical perturbations, which can be caused by round-off in resolving the Navier-Stokes equations or an asymmetry in the computational mesh. We also mimicked the fabrication tolerance in physical experiments by imposing a small pressure difference between two outlets and investigated the drifting behavior in such a situation.

4.4.1 Drifting process

Consider a droplet entering a symmetric T-junction as in figure 4.8, three scenarios can happens in the system: (a) symmetric breakup, (b) asymmetric breakup and (c) drifting. In the symmetric breakup scenario (super-critical conditions), the droplet enters the T-junction; it is compressed by the external flow and finally breaks into two identical droplets. The breakup behavior of the droplet in this scenario is similar to that in half-T-junction simulations, as described in section 4.3. Approaching the critical condition, we observed an asymmetric breakup even with the used symmetric T-junction. In this scenario, the droplet drifts away from the center of the T-junction while the breakup is happening, leading to the observed asymmetric breakup. In the drifting scenario (sub-critical conditions), the droplet enters the T-junction; it reaches the steady shape for a short time and drifts away to one of the branches.

In this section, we focus our discussion on the drifting behavior of droplets in near-critical and sub-critical regimes. Figure 4.9 and 4.10 show the displacement y_c/w of the center of mass (CoM) during the drifting, for two droplet lengths, $l_0/w = 2.8$ and 2.0. We recorded the movement of the center of mass from the moment when the droplet entirely departs from the feed channel ($Ut/w = 0$) until the moment when it moves far away from the center of the T-junction. The drifting process comprises three phases: (i) initially, the droplet drifts exponentially out of the center of the T-junction owing to flow perturbation, followed by (ii) a transition phase and (iii) when the droplet fully enters one branch of the T-junction, it moves linearly.

Figure 4.9(*b*) shows snapshots of the droplet shape during the drifting process for l_0/w=2.8 and Ca=4.3×10^{-3}. At Ut/w=0, the droplet fully enters the branch of the T-junction. The droplet stays at the center of the T-junction, corresponding to $y_c/w \approx 0$, until $Ut/w = 0.73$. The moment when the droplet starts moving out of the center

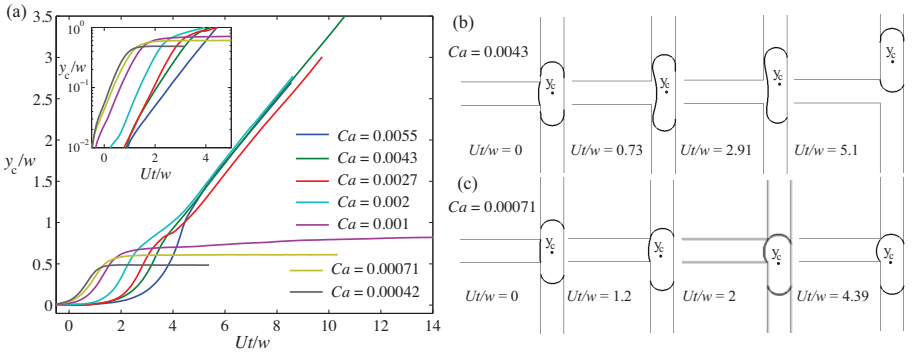

Figure 4.9 (a) Displacement of the center of mass (CoM) during a drifting process for $l_0/w = 2.8$ for different capillary numbers. The inset shows the plots of the displacement of the CoM in log-lin scale. (b) Snapshots of droplet shapes for $Ca = 4.3 \times 10^{-3}$. (c) Snapshots of droplet shapes for $Ca = 7.1 \times 10^{-4}$.

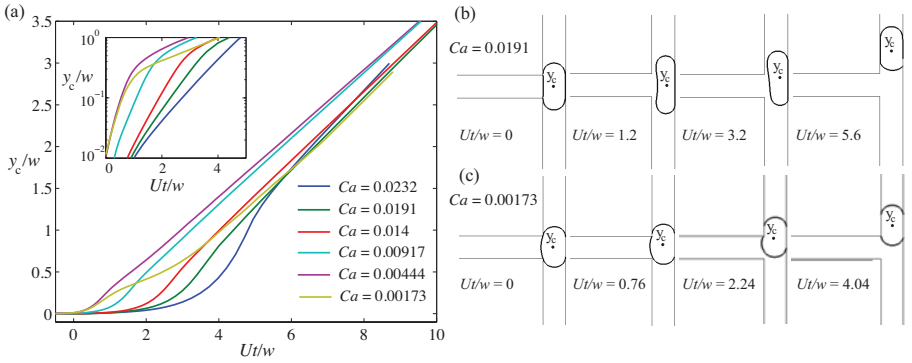

Figure 4.10 (a) Displacement of the center of mass (CoM) during a drifting process for $l_0/w = 2.0$ for different capillary numbers. The inset shows the plots of the displacement of the CoM in log-lin scale.(b) Snapshots of droplet shapes for $Ca = 1.91 \times 10^{-2}$. (c) Snapshots of droplet shapes for $Ca = 1.73 \times 10^{-3}$.

depends on the ratio between the force exerted by the external flow on the droplet and the flow perturbation. For lower capillary numbers (smaller external forces), the droplet moves out of the center earlier. Once the droplet starts drifting, it moves exponentially in time: $y_c/w \sim e^{\lambda_1 Ut/w}$ (see the inset of figure 4.9(a)). In this phase, the drifting of the droplet can be primarily caused by the flow perturbations in the system. These perturbations grow exponentially in time, resulting in the exponential drifting as observed in our simulations. We also observed that while the droplet drifts away ($Ut/w = 2.91$), the gap between the droplet and the channel wall on one branch

of the channel increases and a large part of the flow goes into that branch. This is similar to the experimental observation shown in figure 11 of Fu et al. [10]. At $Ut/w \approx 4$ (not shown in figure 4.9(*b*)), the droplet almost gets into one branch of the T-junction, at which the transition phase starts. Our results show that the duration of the transition phase is longer for smaller capillary numbers. At $Ut/w = 5.1$, the droplet fully enters one branch of the T-junction. From that moment on, the droplet speed is driven only by the strength of the external flow in the branch of the T-junction. Thus, the position of the center of mass linearly depends on the convective timescale: $y_c/w \sim \lambda_2 Ut/w$.

For the capillary numbers that are much smaller than the critical value, there is a change in the drifting behavior. Figure 4.9(*c*) shows snapshots of the droplet shape for $l_0/w = 2.8$ and $Ca = 7.1 \times 10^{-4}$. In the initial stage of the drifting, the droplet also moves exponentially out of the center of the T-junction. However, in the transition phase ($Ut/w = 2$), part of the droplet bumps back into the feed channel, resulting in a high flow resistance in one branch of the T-junction. Therefore, all injected fluid flows into another branch. As a consequence, the droplet is stuck at the corner of the T-junction and cannot go further downstream. For $Ca < 10^{-3}$, our results show that the center of mass keeps constant for a long time and probably the droplet will stay indefinitely in the transition regime.

The drifting behavior of the droplet of length $l_0/w = 2.0$ and 2.8 shares many similarities, as shown in figure 4.10. There are also three phases during the drifting: (i) an exponential drifting, (ii) a transition phase and (iii) a linear drifting. For this droplet length, we did not observed the situation in which the droplet is stuck at the corner of the T-junction even though for the lowest capillary number ($Ca = 1.73 \times 10^{-3}$), part of the droplet also bumps back into the feed channel. At this capillary number, the duration of the transition phase is relatively longer than that at higher capillary numbers. It might be that for a much lower capillary number, we will also observe the sticking behavior.

To further our understanding on the drifting behavior, we measured the variation of the exponent λ_1 and the coefficient λ_2 for different capillary numbers for two considered droplet lengths. For $l_0/w = 2.8$, the exponent λ_1 varies from 2.29 to 1.33 for $4.2 \times 10^{-4} < Ca < 5.5 \times 10^{-3}$. For $l_0/w = 2.0$, the coefficient λ_1 varies from 3.15 to 1.58 for $1.7 \times 10^{-3} < Ca < 2.3 \times 10^{-2}$. We do not have any explanations for the observed values of λ_1 yet. For λ_2, we found that it varies from 0.37 to 0.46 for both droplet lengths. The value of λ_2 depends on the ratio between the pressure drops over two branches of the T-junction: $\lambda_2 = 1/\left(1 + \Delta p_{drop}/\Delta p_{nodrop}\right)$. Δp_{drop} and Δp_{nodrop} are the pressure drops over one branch of the T-junction with and without the presence

of the droplet. They can be computed as:

$$(\Delta pw/\gamma)_{nodrop} = \frac{12\mu L/w}{1-0.63\frac{h}{w}}\frac{w^2}{h^2}Ca \tag{4.1}$$

$$(\Delta pw/\gamma)_{drop} = \frac{12(\mu(L-l_0)/w+\hat{\mu}l_0/w)}{1-0.63\frac{h}{w}}\frac{w^2}{h^2}Ca+4.77\left(1+\frac{w}{h}\right)(3Ca)^{2/3} \tag{4.2}$$

where $L=6w$ is the length of one branch of the used T-junction. For $l_0/w=2.8$, the predicted values of λ_2 are 0.34 for $Ca=4.2\times10^{-4}$ and 0.45 for $Ca=5.5\times10^{-3}$. Our prediction shows a good agreement with the simulated value of λ_2.

4.4.2 Influence of the prescribed pressure difference on the drifting

In physical experiments, there always exists a geometrical difference between two branches of the T-junction owing to the fabrication tolerance. This difference can cause a flow asymmetry in the system. To investigate the influence of the flow asymmetry on the drifting process, we performed simulations in which a small pressure difference Δp between two outlets of the T-junction was imposed. Figure 4.11 shows the drifting behavior of the droplet of length $l_0/w=2.8$ at $Ca=5.5\times10^{-3}$ for six different values of rescaled pressure difference: $\Delta Pw/\gamma=0;0.003;0.015;0.03;0.045;0.06$. Figure 4.11(*a*) shows that the droplet drifts with the same rate during the first phase of the drifting. The only change we observed is the initial displacement y_{c0}/w. Figure 4.11(*b*) shows that the initial displacement linearly depends on the prescribed pressure difference. Similar behavior was observed for $l_0/w=2.0$ (see figure 4.12). For this droplet length, we also studied the influence of the capillary numbers on the initial displacement with the prescribed pressure difference. Figure 4.12(*b*) shows that the initial displacement increases with decreasing capillary numbers.

The dependence of the initial displacement on the prescribed pressure difference Δp between two outlets of the T-junction can be expressed as:

$$\frac{l_0/2+y_{c0}}{l_0/2+y_{c0}} = \frac{p_c+\Delta p/2}{p_c-\Delta p/2} \tag{4.3}$$

where $p_c \sim f(Ca)$ is the pressure of the external phase at the center of the junction. With a small manipulation of Eq. 4.3, the initial displacement can be expressed as $y_{c0}=\Delta p l_0/4p_c$. This simple model teaches us that the initial displacement is linearly proportional to the pressure difference Δp for a fixed droplet length and capillary number, as shown in figure 4.11(*b*) and 4.12*(b)*. Also based on this model, the slope of the line $y_{c0}(\Delta p)$ increases with decreasing capillary number and increasing droplet length, qualitatively in agreement with our numerical simulations.

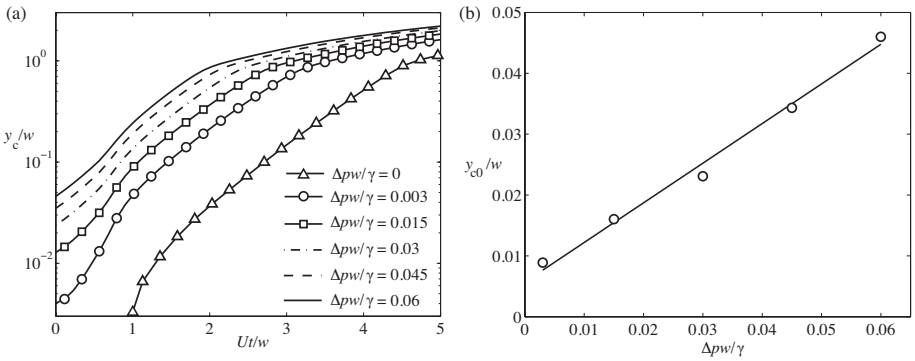

Figure 4.11 (a) Displacement of the center of mass for (l_0/w=2.8; Ca=5.5×10^{-3}) for various prescribed pressure differences between two outlets. (b) Initial displacement of droplets versus prescribed pressure differences between two outlets.

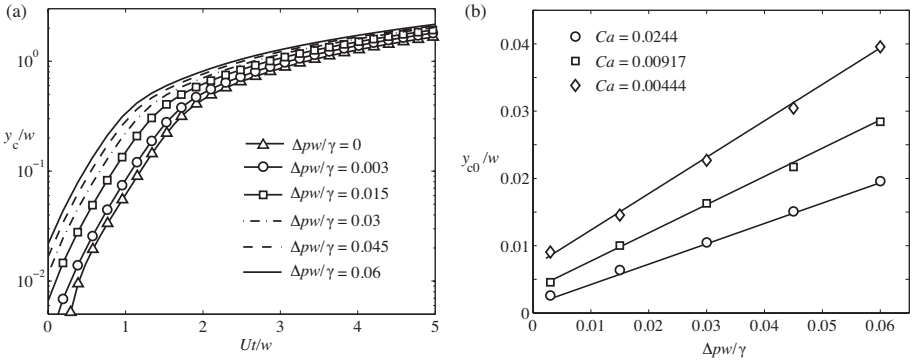

Figure 4.12 (a) Displacement of the center of mass for ($l_0/w = 2.0; Ca = 9.17 \times 10^{-3}$) for various prescibed pressure differences between two outlets. (b) Initial displacement of droplets versus prescribed pressure differences between two outlets.

4.5 Critical breakup conditions

In previous section, we investigated the behavior of droplet during the breakup and drifting process. We now combine our understanding on the two timescales, breakup time and drifting time, to determine the critical condition for the breakup.

Figure 4.13(a) shows a comparison of the breakup time and the drifting time for $l_0/w = 2.8$. The solid line shows the breakup time for different capillary numbers obtained with symmetric-BC simulations. The square symbols show the drifting time for different capillary numbers obtained with full-T-junction simulations. From sec-

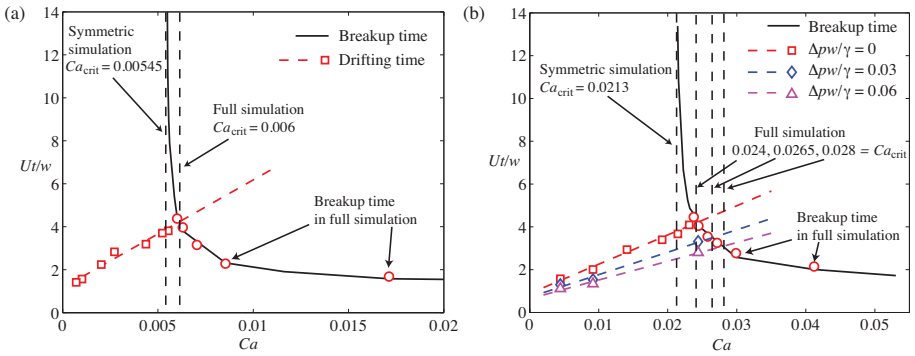

Figure 4.13 A comparison of the timescale for breakup the timescale for drifting for (a) $l_0/w=$ 2.8 and (b) $l_0/w=2$. The solid lines show the breakup time obtained with symmetric-BC simulations as described in section 4.3. The circles show the breakup time obtained in the full-T-junction simulations. The squares, triangles and diamonds show the drifting time as described in section 4.4. The colored dashed lines are a fitting of the drifting time.

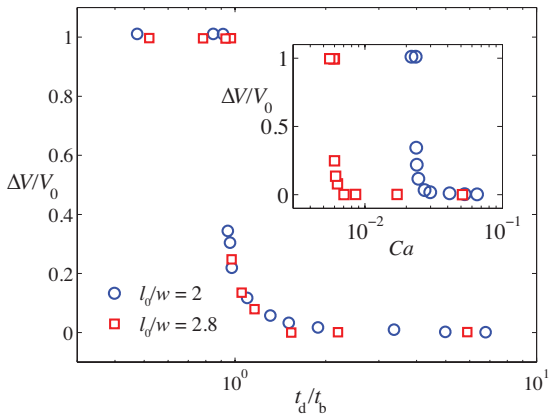

Figure 4.14 The difference in the volume of two daughter droplets $\Delta V/V_0$ as a function of the ratio between the drifting time and the breakup time t_d/t_b. The inset plots these volume differences against the capillary number.

tion 4.4, we noticed that the droplets will not break once the displacement of the center of mass is larger than $0.5w$. Therefore, the drifting time presented here is determined at the moment when $y_c/w=0.5$. Figure 4.13(a) shows three types of droplet behavior: (i) droplet breaks in both the symmetric-BC and full-T-junction simulations for $Ca > 6\times10^{-3}$,(ii) droplet breaks in the symmetric-BC simulations but does not break in the full-T-junction simulations for $5.45\times10^{-3} < Ca < 6\times10^{-3}$ and (iii)

droplet does not break in both the symmetric-BC and full-T-junction simulations for $Ca < 5.45 \times 10^{-3}$. In regime (i), the breakup time is smaller than the drifting time such that the droplet will break into two daughters. The size of these two daughter droplets depends on the ratio between two timescales, as discussed below. There is no difference in the breakup time in symmetric-BC and full-T-junction simulations. In regime (ii), the breakup time increases rapidly and is much larger than the drifting time. Thus, in the full-T-junction simulations, the droplet does not have enough time to break as it does in the symmetric-BC simulations but drifts away into one branch of the junction. In regime (iii), the droplet does not break in the symmetric-BC simulations and certainly drifts away in the full-T-junction simulations owing to the flow perturbations. Our results show that the critical capillary numbers for the breakup of droplet are 5.45×10^{-3} and 6×10^{-3} for the symmetric-BC and full-T-junction simulations, respectively. Owing to the drifting, the "critical" capillary number below which the droplet drifts away in the full-T-junction simulations increases 10% with respect to the "real" critical capillary number obtained in the symmetric-BC simulations.

Similar analysis for $l_0/w = 2.0$ was shown in figure 4.13(*b*). We observed the same behavior in the competition of the two timescales. For this droplet length, we extend our analysis to the situations in which there is a small pressure difference between two outlets of the T-junction. We plotted the drifting time of the droplet for three different values of the prescribed pressure difference: $\Delta pw/\gamma = 0; 0.03; 0.06$. We found that an increase of the prescribe pressure difference leads to an increase of the critical capillary number below which the droplet drifts away. The same effect is expected for the droplet length of $l_0/w = 2.8$. The "real" critical capillary number for breakup in the symmetric-BC simulations is 2.13×10^{-2} while the "critical" capillary numbers for breakup in the full-T-junction simulations are $2.4 \times 10^{-2}, 2.65 \times 10^{-2}, 2.8 \times 10^{-2}$ for $\Delta pw/\gamma = 0; 0.03; 0.06$. The differences between the two critical capillary numbers are 12%, 24% and 31% for $\Delta pw/\gamma = 0; 0.03; 0.06$, respectively.

The existence of the drifting not only influences the critical capillary number for the breakup but also leads to an asymmetric breakup in the full-T-junction simulations. Figure 4.14 shows the variation of the difference in the volume of two daughter droplets as a function of the ratio between the two timescales, breakup time and drifting time. The drifting time presented in figure 4.14 was obtained for $\Delta pw/\gamma = 0$. In drifting regime ($t_d/t_b < 1$), breakup does not happen and the droplet entirely moves into one branch of the T-junction; thus $\Delta V/V_0 = 1$. Close to the critical condition for breakup, the two timescales become comparable ($t_d/t_b \sim 1$). In this situation, the droplet drifts away during the breakup. As a result, the droplet breaks asymmetrically. In this asymmetric breakup regime, the droplet always stays in the first phase of drifting process. Knowing the breakup time, one can compute the level of asymmetry based on the drifting speed of the droplet. Far from the critical condition ($t_d/t_b > 2$), the droplet just stays at the center of the T-junction during the breakup process, resulting in a symmetric breakup ($\Delta V/V_0 = 0$).

4.6 Conclusion

We have shown that the critical capillary number for breakup is controlled by the ratio between the timescale for breaking and the timescale for drifting. To separately study the behavior of these two timescales, we performed two types of simulations, symmetric-boundary-condition and full-T-junction simulations. The symmetric-BC simulation provide a free-perturbation flow system, thus allow us to compute the breakup time for different capillary number and to accurately identify the critical capillary number. When the capillary number approaches the critical value, the breakup time increases towards infinity. We found that the breakup time scales with $(Ca/Ca_{crit} - 1)^{-1/3}$ for both two considered droplet lengths. The drifting behavior was studied with the full-T-junction simulations. Three phases was identified during the drifting process: (i) an exponential drifting, (ii) a transition phase and (iii) a linear drifting. Our result shows that the exponential drifting phase controls the behavior of the drifting time. We found that the drifting time linearly depends on the capillary number.

Understanding the behavior of the two timescales, we can determine the critical capillary number below which the droplet drifts away into one branch of the T-junction. Owing to the drifting, the critical capillary number for breakup increases with respect to the one obtained in free-perturbation flow systems. The ratio between the timescale for drifting t_d and the timescale for breaking t_b determines how asymmetrically the breakup is. Our work reveals that symmetric breakup is obtained when the ratio t_d/t_b is larger than 2, corresponding to $(Ca - Ca_{crit})/Ca_{crit} \approx 0.5$ for the considered droplet lengths.

Bibliography

[1] B. T. Kelly, J. C. Baret, V. Talyab, and A. D. Griffiths. Miniaturizing chemistry and biology in microdroplets. *Chem. Commun.*, 18:1773 – 1788, 2007.

[2] S.-Y. Teh, R. Lin, L.-H. Hung, and A. P. Lee. Droplet microfluidics. *Lab Chip*, 8:198 – 220, 2008.

[3] C. N. Baroud, F. Gallaire, and R. Dangla. Dynamics of microfluidic droplets. *Lab Chip*, 10(16): 2032–2045, 2010.

[4] J. D. Tice, H. Song, A. D. Lyon, and R. F. Ismagilov. Formation of droplets and mixing in multiphase microfluidics at low values of the reynolds and the capillary numbers. *Langmuir*, 19(22):9127–9133, 2003.

[5] A. Günther and K. F. Jensen. Multiphase microfluidics: from flow characteristics to chemical and material synthesis. *Lab Chip*, 6:1487–1503, 2006.

[6] M. T. Kreutzer, A. Gunther, and K. F. Jensen. Sample dispersion for segmented flow in microchannels with rectangular cross section. *Anal. Chem.*, 80(5):1558–67, 2008.

[7] A. M. Leshansky and L. M. Pismen. Breakup of drops in a microfluidic T junction. *Phys. Fluids*, 21 (2):023303, 2009.

[8] D. Link, S. Anna, D. Weitz, and H. Stone. Geometrically mediated breakup of drops in microfluidic devices. *Phys. Rev. Lett.*, 92(5), 2004.

[9] M. C. Jullien, M. J. Tsang Mui Ching, C. Cohen, L. Menetrier, and P. Tabeling. Droplet breakup in microfluidic T-junctions at small capillary numbers. *Phys. Fluids*, 21(7):072001, 2009.

[10] T. Fu, M. Youguang, D. Funfschilling, and H. Z. Li. Dynamics of bubble breakup in a microfluidic T-junction divergence. *Chem. Eng. Sci.*, 66:4184ï£¡4195, 2011.

[11] Y. X. Zhang and L. Q. Wang. Nanoliter-droplet breakup in confined T-Shaped junctions. *Curr. Nanosci.*, 7(3):471–479, 2011.

[12] H. G. Weller, G. Tabor, H. Jasak, and C. Fureby. A tensorial approach to computational continuum mechanics using object-oriented techniques. *Comp. Phys.*, 12(6):620–631, 1998.

[13] D. A. Hoang, V. van Steijn, L. M. Portela, M. T. Kreutzer, and C. R. Kleijn. Benchmark numerical simulations of segmented two-phase flows in microchannels using the Volume of Fluid method. *Comp. Fluid.*, 86(0):28–36, 2013.

[14] V. van Steijn, M.T. Kreutzer, and C.R. Kleijn. Velocity fluctuations of segmented flow in microchannels. *Chem. Eng. J.*, 135(0):S159 – S165, 2008.

5. Design and characterization of bubble-splitting distributor for scaled-out multiphase microreactors[§]

This chapter reports an analysis of the parallelized production of bubbles in a microreactor based on the repeated break-up of bubbles at T-junctions linked in series. We address the question how to design and operate such a multi-junction device for the even distribution of bubbles over the exit channels. We study the influence of the three primary sources leading to the uneven distribution of bubbles: (1) nonuniformity in the size of bubbles fed to the distributor, (2) lack of bubble break-up, and (3) asymmetric bubble breakup caused by asymmetries in flow due to fabrication tolerances. Based on our theoretical and experimental analysis, we formulate two guidelines to operate the multi-junction bubble distributor. The device should be operated such that: (i) the capillary number exceeds a critical value at all junctions, $Ca > Ca_{\text{crit}}$, to ensure that all bubbles break, and (ii) the parameter $(l_s/w) \cdot Ca^{1/3}$ is sufficiently large, with l_s/w the distance between the bubbles normalized by the channel width. More quantitatively, $(l_s/w) \cdot Ca^{1/3} > 2$ for fabrication tolerances below 2%, which are typical for devices made by soft lithography. Furthermore, we address the question whether including a bypass channel around the T-junctions reduces flow asymmetries and corresponding nonuniformities in bubble size. While bubble nonuniformities in devices with and without bypass channels are comparable for fabrication tolerances of a few percent, we find that incorporating a bypass channels does have a beneficial effect for larger fabrication tolerances. The results presented in this chapter facilitate the scale-out of bubble-based microreactors.

[§]Published as: D. A. Hoang, C. Haringa, L. M. Portela, M. T. Kreutzer, C. R. Kleijn and V. van Steijn. Design and characterization of bubble-splitting distributor for scaled-out multiphase microreactors. *Chemical Engineering Journal*, In press, 2013, doi: 10.1016/j.cej.2013.08.066.

5.1 Introduction

Multiphase microreactors have emerged as an attractive class of reactors for the production of fine chemicals and pharmaceuticals[1,2], for the synthesis of micro- and nanoparticles[3–7], and for high-throughput screening applications[8–11]. Besides excellent heat and mass transfer characteristics in microreactors, continuous flow chemistry based on the confinement of reactions in picoliter to nanoliter bubbles or droplets (a) enhances mixing, (b) reduces axial dispersion, and (c) prevents precipitation at walls and clogging of channels such that higher yields and selectivities are obtained[10,12].

Despite the conceptually simple idea of numbering-up as a strategy to increase throughput, parallelization of segmented flows remains a challenge in practice[13]. One basic approach to increase throughput of segmented flow microreactors is to produce droplets or bubbles in each individual channel[14–24]. With a few notable exceptions[25–27], this approach requires that the supply of the fluids to all these channels is identical, as differences in flow lead to corresponding differences in the volume, frequency, and speed of the bubbles or droplets. Integrating resistive channels upstream of the segmented flow channels minimizes cross-talk between the channels and ensures a constant supply of fluids, which is not affected by the dynamic pressure fluctuations in the segmented flow channels[17,28]. de Mas et al.[17] showed that the pressure drop over the resistive channels should be two orders of magnitude larger than the pressure drop over the segmented flow channels. Fulfilling this requirement is particularly challenging for gas-liquid flows, because the low viscosity of gas requires resistive gas channels that are roughly two orders of magnitude smaller in width than the segmented flow channels. These channels should be fabricated with high precision, as small difference in their hydrodynamic resistance lead to differences in the features of the segmented flows running in parallel.

An alternative approach that does not require on-chip integration of resistive feed channels is to feed a segmented flow to the chip, and split the bubbles or droplets at a series of successive junctions[29–33]. To obtain segmented flows with an identical bubble volume and bubble spacing in all channels downstream the bubble distributor, two key questions need to be addressed: 1) how to ensure breakup at all junctions, 2) how to minimize asymmetries in flow. The first question can be addressed based on the understanding of breakup of bubbles or droplets at single T-junctions. Whether a droplet breaks primarily depends on its length relative to the channel width, l/w, and on the capillary number, Ca[34–39]. Of secondary importance is the viscosity contrast between the two phases[40,41]. The second question can be addressed by considering the differences in hydrodynamic resistances of the channels due to fabrication inaccuracies. As well known for single T-junctions, a difference in velocity in the two exiting arms leads to the asymmetric breakup of bubbles[34,42–45]. Consequently, the size of the bubbles and their distance apart is different in the two exiting arms. For a multi-junction device, Adamson et al.[29] identified a second cause for unequal flow

distribution: if bubbles enter downstream T-junctions at times that are not precisely coordinated, the backpressure generated when the bubbles split causes an imbalance in the pressure drops across the two exiting arms of the upstream T-junctions. This also leads to asymmetries in segmented flows. They showed that this source of variation is reduced by designing the system such that the magnitude of the pressure pulses is negligible with respect to the total pressure drop over the branches. Another clever trick to reduce the influence of pressure pulses at downstream T-junctions is to reduce the coupling between the successive T-junctions by incorporating a pressure-equalizer at the T-junctions in the form of a bypass-like structure[32]. Although this concept has been demonstrated, no quantative data is available on the influence on this bypass.

Summarizing the work done on multi-junction bubble and droplet distributors, we conclude that – although there are some pointers on how to design and operate these devices – there is no systematic study how key operating conditions influence the performance, and to what extend polydispersity is reduced by incorporating a pressure equalizer.

In this chapter, we start with a discussion on the different design strategies and explain why a design that fixes the relative length of the bubbles or droplets is favorable over other types of design. We then identify three primary sources leading to the uneven distribution of bubbles and systematically study their influence on the uniformity of the size of bubbles in the downstream channels of a multi-junction device. Additionally, we quantify to what extend flow asymmetries are reduced with the use of a pressure equalizer. In short, this chapter teaches how to design and operate a multi-junction bubble distributor.

5.2 Theory on the design and operation of a multi-junction bubble distributor

5.2.1 Design

Non-breaking bubbles are one of the main sources of polydispersity. A straightforward approach to ensure breakup at all successive junctions is to design the network such that l/w and *Ca* are kept the same at all junctions. Operating the device above the transition line ($Ca_{\text{crit}} = f(l/w)$) at the first junction then ensures breakup at all successive junctions. But, in the planar networks that are commonly used in the field of microfluidics *Ca* and l/w cannot be fixed at the same time. This is easily seen from the fact that the flow rate entering a junction hw_iv_i equals twice the flow rate in the two exiting channels $hw_{i+1}v_{i+1}$ that lead to the next junctions, with h the channel height, w the channel width, v the bubble velocity, and i the index of the junction. Hence, $v_{i+1} = \frac{1}{2}\frac{w_i}{w_{i+1}}v_i$. Defining the capillary number based on the bubble velocity,

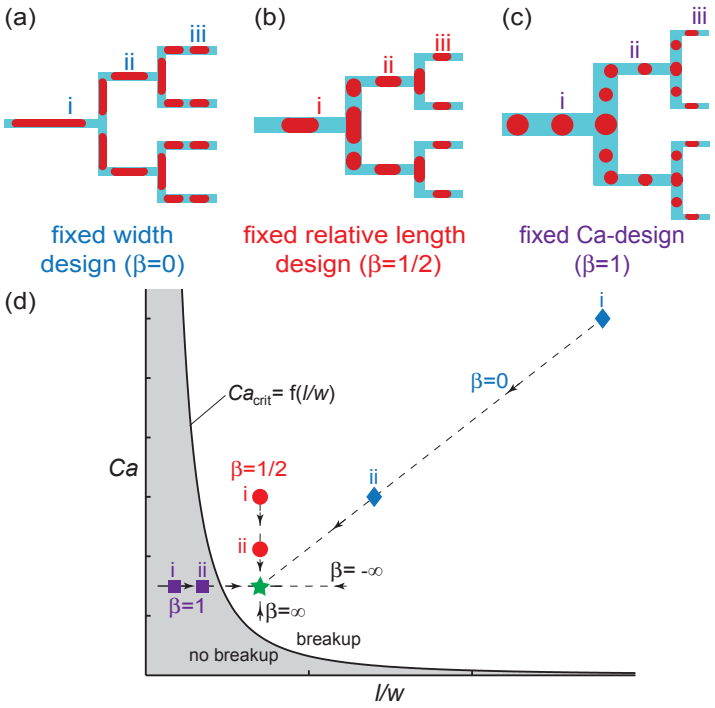

Figure 5.1 Examples of three design strategies in which the channel width (a), relative bubble length (b), and capillary number (c) is fixed for a bubble splitter comprising two generations of T-junctions. (d) Sketch of a breakup map (Ca, l/w); the gray area below the transition line ($Ca_{\text{crit}} = f(l/w)$) indicates the region in which bubbles do not break. For a desired relative bubble length and bubble velocity in the exit channels (indicated by the green star), the length and Ca needed in the channels leading to the first (i) and second (ii) generation are shown for the three design strategies.

the viscosity of the compartments between the bubbles, μ, and the interfacial tension, γ, according to $Ca = \mu v/\gamma$, we hence find that the capillary number decreases at successive junctions according to $Ca_{i+1} = \frac{1}{2}\frac{w_i}{w_{i+1}} Ca_i$. Similarly, the volume of a bubble flowing into a junction $\sim h w_i l_i$ equals twice the volume of the daughter droples leaving the junction $\sim h w_{i+1} l_{i+1}$. Hence, $l_{i+1} = \frac{1}{2}\frac{w_i}{w_{i+1}} l_i$ such that the relative length decreases at successive junctions according to $l_{i+1}/w_{i+1} = \frac{1}{2}\frac{w_i^2}{w_{i+1}^2} l_i/w_i$. This simple analysis shows that fixing Ca requires a reduction in width by a factor 2 in successive junctions, whereas a $2^{1/2}$ reduction is needed to fix the relative length l/w[29]. Fixed l/w-designs[29] and fixed Ca-designs[30] have both been demonstrated, as well as design in which the width of the channels is fixed such that both Ca and l/w decrease at

successive junctions[34]. These three design strategies are illustrated in Fig. 5.1a-c for a network in which segmented flow is distributed over four channels by breaking the incoming stream of bubbles at two successive generations of T-junctions. Of course, other choices are possible for $w_i/w_{i+1}=2^{\beta}$, but for the sake of simplicity we limit the discusson to designs with a fixed w ($\beta=0$, Fig. 5.1a), a fixed l/w ($\beta=0.5$, Fig. 5.1b), and a fixed *Ca* ($\beta=1$, Fig. 5.1c).

To compare these different designs, we calculate the values of *Ca* and l/w required in the feed channel (i) and in the channels downstream of the first junction (ii) to obtain a desired *Ca* and l/w in the output channels (iii). This desired point is indicated by a star in the $(l/w, Ca)$ map sketched in Fig. 5.1d and lies above the transition line. Below this line (shaded area), breakup does not occur. As shown for the fixed width device ($\beta=0$), relatively long bubbles or droplets need to be fed to the first junction at relatively high *Ca*. Both these requirements pose a problem, because long droplets or droplets might spontaneously breakup[29], while operating at high *Ca* leads to the formation of satellites during breakup[30]. By contrast, the fixed *Ca*-design ($\beta=1$) requires a feed of short bubbles or droplets to the first junction, which are exceedingly difficult to break. For the example discussed here, the bubble length in channels (i) and (ii) is below the required length for breakup. Compared to the fixed-width and fixed-*Ca* designs, the fixed l/w-design ($\beta=0.5$) can be operated at relatively low values of *Ca* and l/w, while ensuring that breakup occurs at all successive junctions. We therefore focus on the fixed relative length-design in this chapter.

We conclude this section on the design by illustrating the design methodology for the fixed relative length-design based on a practical example. Suppose one aims to produce a gas-liquid segmented flow in 8 parallel channels that each have a height and width of $50\,\mu\mathrm{m}$, with bubbles having a length of $200\,\mu\mathrm{m}$. One then uses a cascade with three generations. For a desired bubble velocity of in these exit channels of $10\,\mathrm{cm/s}$, the corresponding capillary number can be calculated using the flow properties. Taking, for example, a viscosity of $1\,\mathrm{mPas}$ and an interfacial tension of $5\,\mathrm{mN/m}$, $Ca=2\cdot10^{-2}$. Knowing the relative length and capillary number in the 8 exit channels, one calculates the relatively length and capillary number in the channels leading to the T-junctions of the last generation and finds $l/w=4$, $Ca=2.8\cdot10^{-2}$. To ensure that bubbles break at all junctions of the device, it is sufficient to check whether the capillary number in the channels leading to the last generation of T-junctions is larger than the critical capillary number for the desired relative length $l/w=4$. As explained later in section 5.4.4, the critical capillary number can be calculated using $Ca_{\mathrm{crit}}=0.98(l/w)^{-3.60}$. After confirming that $Ca>Ca_{\mathrm{crit}}$, the only thing left to do is to calculate the relative length and velocity of the bubbles that need to be fed to the multi-junction device.

5.2.2 Operation

Throughout this chapter, we quantify the nonuniformity in bubble size based on the coefficient of variation CV. Unless stated otherwise, we use the following definition

$$CV = \frac{\sigma(l)}{\bar{l}} \tag{5.1}$$

with $\bar{l}$ and $\sigma(l)$ the average bubble length and the standard deviation in bubble length.

Influence of non-breaking bubbles on size uniformity

We now quantify the influence of non-breaking bubbles on the size uniformity. For a single T-junction, it is straightforward to calculate how the polydispersity is influenced in case m out of n incoming bubbles do not break. The coefficient of variation, CV_{out}, of the bubbles leaving the two arms of the T-junction depends on the coefficient of variation, CV_{in}, of the incoming bubbles, and on the breakup fraction defined as $\eta = (n-m)/n$ according to

$$\frac{CV_{\text{out}}^2 + 1}{CV_{\text{in}}^2 + 1} = \frac{\eta\,(1-\eta)}{2} + 1 \tag{5.2}$$

To demonstrate the sensitivity of CV_{out} on the break-up fraction, we calculate CV_{out} for several values of η for the case $CV_{\text{in}} = 0$. This shows that 1% non-breaking bubbles ($\eta = 0.99$) already leads to a polydisperse size distribution with a value of $CV_{\text{out}} = 0.07$. For 5% and 10% non-breaking bubbles, the coefficients of variation are 0.15 and 0.21 respectively. This simple analysis hence shows the importance to ensure that all bubbles break.

Influence of flow asymmetries due to fabrication errors on size uniformity

Ensuring that all bubbles break is a necessary but not sufficient condition to ensure a narrow size distribution. We now focus on the question how asymmetries in flow that are caused by fabrication errors influence the polydispersity. This analysis also reveals how polydispersity in bubble size at the exit of the parallel channels is influenced by the size uniformity of the bubbles fed to the bubble distributor. For the sake of simplicity, we start the analysis by considering a single T-junction. We hereby consider fabrications errors only in the height of the channels. For microchannels fabricated using soft lithography, this assumption is justified by the fact that tolerances in channel width or length are typically much smaller than tolerances in channel height. We assume that the height of one of the exit channels is $h - u(h)$,

while the height of the second exit channel is $h+u(h)$. The difference in height leads a difference velocities, $v-u(v)$ and $v+u(v)$. Consequently, the lengths of the two daughter droplets follow from $(v+u(v))/(l+u(l))=(v-u(v))/(l-u(l))$[34]. Similarly, the length of the compartments (slugs) between the bubbles or droplets after split-up follows from $(v+u(v))/(l_s+u(l_s))=(v-u(v))/(l_s-u(l_s))$. For channels of equal length, the number of bubbles and compartments is $n-u(n)$ and $n+u(n)$ in the channels with higher and lower velocity respectively, according to $(v+u(v))/(v-u(v))=(n-u(n))/(n+u(n))$. To understand how the relative flow asymmetry, $u(v)/v$, depends on the relative error in channel height $u(h)/h$, the capillary number, the height-to-width ratio of the channel, h/w, and the dimensionless length of the compartment between bubbles, we equate the pressure drop over the two exiting channels. To predict the pressure drop over a channel of width w and height $h<w$ through which n bubbles of length l and n slugs of length l_s flow at a velocity v, we use a similar expression as in Fuerstman et al.[46], van Steijn et al.[47], Parthibana and Khan[48]

$$\Delta p = n\frac{12\mu l_s}{1-0.63\frac{h}{w}}\frac{1}{h^2}v + nC\gamma\left(\frac{2}{w}+\frac{2}{h}\right)(3Ca)^{2/3} \tag{5.3}$$

with μ the viscosity of the compartments between the bubbles, γ the interfacial tension and C an order one constant[46,49,50]. We hereby neglect the viscous pressure drop over the gas bubbles, and define the capillary number as $Ca=\mu v/\gamma$. Substituting the expressions for the lengths of the bubbles and liquid compartments, the bubble velocity, the number of compartments, and the channel height, we find expressions for the two pressure drops over the two exiting channels. Equating these pressure drops and solving for $u(v)/v$ under the assumption $u(v)/v<<1$ yields

$$\frac{u(v)}{v} = \frac{(C_3-C_1)\,\frac{l_s}{w}Ca^{1/3}+(C_4-C_2)}{(C_1+C_3)\,\frac{l_s}{w}Ca^{1/3}-(C_2+C_4)/3} \tag{5.4}$$

with

$$C_1 = \frac{12}{1-0.63\frac{h}{w}\left[1+\frac{u(h)}{h}\right]}\frac{w^2}{h^2}\left[1+\frac{u(h)}{h}\right]^{-2}$$

$$C_2 = 2C\left(1+\frac{w}{h}\left[1+\frac{u(h)}{h}\right]^{-1}\right)3^{2/3}$$

$$C_3 = \frac{12}{1-0.63\frac{h}{w}\left[1-\frac{u(h)}{h}\right]}\frac{w^2}{h^2}\left[1-\frac{u(h)}{h}\right]^{-2}$$

$$C_4 = 2C\left(1+\frac{w}{h}\left[1-\frac{u(h)}{h}\right]^{-1}\right)3^{2/3}$$

As expected for the single phase limit (long slugs, high velocity) and small fabrication errors, this reduces to $\frac{u(v)}{v} \approx \left(2+\frac{0.63\frac{h}{w}}{1-0.63\frac{h}{w}}\right)\frac{u(h)}{h}$. This simple model teaches how a small difference in channel height leads to asymmetries in flow for a single T-junction.

We now extend the analysis to a multi-junction device. For a cascade device with k generations, it is straightforward to show that the coefficient of variation for the bubbles collected at the 2^k exiting channels, CV_{out}, depends on the coefficient of variation of the bubbles fed to the device, CV_{in}, and the asymmetries in flow at the different generations, $(u(v)/v)_i$, according to

$$\frac{CV_{\text{out}}^2+1}{CV_{\text{in}}^2+1} = \prod_{i=1}^{k}\left(1+\left(\frac{u(v)}{v}\right)_i^2\right) \tag{5.5}$$

We hereby used the simplifying assumption that the flow asymmetries at the junctions in the same generation are identical. For the fixed relative length design considered in this study, with narrowing channels immediately after the T-junctions, the flow asymmetries can be written as

$$\left(\frac{u(v)}{v}\right)_i = \frac{(C_3-C_1)\,\alpha_i\left(\frac{l_s}{w}\right)_0 Ca_0^{1/3}+(C_4-C_2)}{(C_1+C_3)\,\alpha_i\left(\frac{l_s}{w}\right)_0 Ca_0^{1/3}-(C_2+C_4)/3} \tag{5.6}$$

with $\alpha_i = 2^{-i/6}$, $\left(\frac{l_s}{w}\right)_0$ the dimensionless length of the compartments between the bubbles fed to the multi-junction device, and Ca_0 the capillary number based on the velocity in the feed channel. In the three-generation network used in this work, we do not narrow the channel in the third generation, such that $\alpha_1 = 2^{-1/6}$, $\alpha_2 = 2^{-2/6}$, and $\alpha_3 = 2^{-5/3}$. For this design, Fig. 5.2a shows how the uniformity of size of the bubbles leaving the 8 exit channels depends on $(l_{s0}/w_0)Ca_0^{1/3}$ for three values of $u(h)/h$. For large $(l_{s0}/w_0)Ca_0^{1/3}$, the uniformity of the bubble size is nearly constant and approaches flow uniformities for single phase flow. For $(l_{s0}/w_0)Ca_0^{1/3}$ approaching zero, the nonuniformity sharply increases. The contribution of each generation to the nonuniformitiy in the size of bubbles leaving the device is shown in Fig. 5.2b. This figure shows that flow asymmetries in the final generation of T-junctions are the main cause of nonuniformities in bubble size for the design used in this work.

In summary, the model (Eqns. (5.5) and (5.6)) developed in this section enables one to predict the nonuniformity in bubble size at the exit of a multi-junction device caused by (i) nonuniformity in the size of bubbles fed to the distributor, and (ii) difference in channel height due to fabrication errors. We note that this model is different from the model proposed by Adamson et al.[29], who identified pressure pulses caused by bubbles entering downstream channels as the main source of flow asymmetries. Since we consider flows at higher values of the capillary number ($Ca > 0.01$) in this chapter, the magnitude of such pressure pulses (γ/w)[47], is negligible compared to the pressure

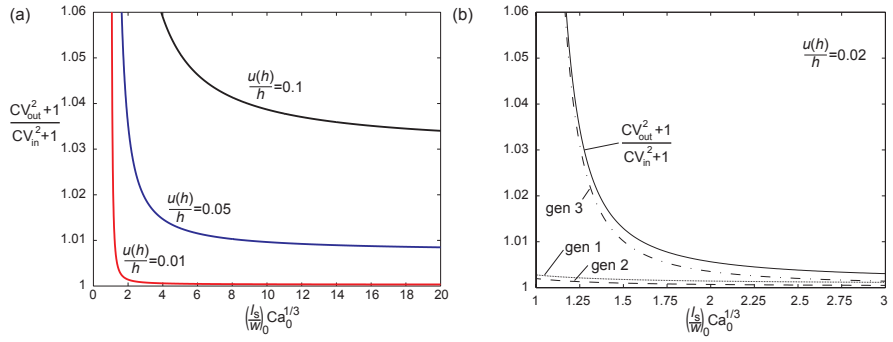

Figure 5.2 (a) Theoretical prediction (Eqns. (5.5) and (5.6)) of nonuniformities in the size of bubbles flowing through the 8 exit channels of a three generation bubble splitter used in this work for three values of $u(h)/h$. (b) $(CV^2_{\text{out}}+1)(CV^2_{\text{in}}+1)$ depends on the contributions $1+(u(v)/v)^2$ of the three generations (gen 1, gen 2, gen 3) according to Eqn. (5.5). This graph shows that nonuniformities in bubble size are mainly caused by flow asymmetries in the T-junctions in the last generation $(u(h)/h=0.02)$.

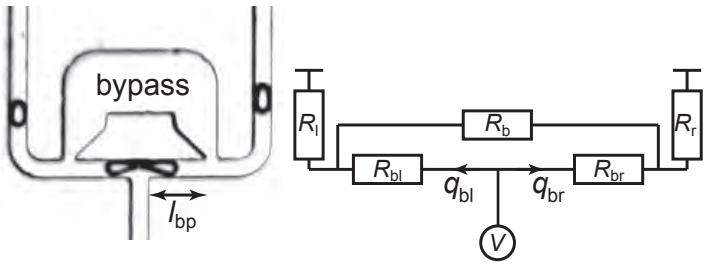

Figure 5.3 A bypass channel around the T-junction significantly reduces asymmetries in flow. This can be understood from an analysis of the hydrodynamic resistances in analogy with the electrical circuit on the right.

drop over a channel (Eqn. (5.3)). We can hence ignore pressure pulses generated by breaking bubbles or bubbles entering the narrowing channel segments.

Influence of the bypass

Including a bypass around the T-junction can reduce flow asymmetries considerably. This is easily seen from an analysis based on hydrodynamic resistances as shown in Fig. 5.3. The asymmetry in relative velocity can be expressed in terms of the flow rates, q_{br} and q_{bl}, in the two branches between the T-junction and the exits of the bypass, as $u(v)/v=(q_{br}-q_{bl})/(q_{br}+q_{bl})$. It is straightforward to show that the

asymmetry in velocity depends on the hydrodynamic resistances of the bypass, the two branches between the T-junction and the exit of the bypass, and the two channels leading to the exit of the device according to

$$\frac{u(v)}{v} = \frac{R_{br} - R_{bl} + (R_l - R_r)\,\frac{R_b}{R_b+R_l+R_r}}{R_{br} + R_{bl} + (R_l + R_r)\,\frac{R_b}{R_b+R_l+R_r}} \tag{5.7}$$

For a bypass with a low resistance ($R_b \to 0$), the flow assymmetry hence only depends on the difference in hydrodynamic resistance of the two short branches of the bypass $u(v)/v = (R_{br} - R_{bl})/(R_{br} + R_{bl})$. In case no bubbles are present in the short branches except the breaking bubble, flow asymmetries in a bypass device can be approximated by the single phase limit $\frac{u(v)}{v} \approx \left(2 + \frac{0.63\frac{h}{w}}{1-0.63\frac{h}{w}}\right)\frac{u(h)}{h}$ derived before. For distances between the bubbles exceeding the distance between the T-junction and the exit of the bypass ($l_s > l_{bp}$), we hence expect that the coefficient of variation depends on the fabrication inaccuracy and is independent of the conditions as long as the device is operated above the critical capillary number. It is important to note that for slugs shorter than the length of the bypass ($l_s < l_{bp}$), bubbles preceeding the breaking bubble likely block the exit of the bypass. With the bypass shut off under these conditions, devices with and without a bypass obviously yield the same coefficient of variation.

5.3 Experimental

We fabricated our devices in PDMS using standard soft lithography techniques[51]. Channels are sealed against PDMS coated glass slides using an air plasma. The devices consist of a T-junction bubble maker, an additional liquid inlet, and three generations of T-junctions as shown in Fig. 5.4a-b. While the size of the bubbles is controlled by the flow rate of gas q_G and liquid q_L injected at the bubble maker, the velocity or distance between the bubbles is controlled using a second liquid stream q_{L2} injected from the side channel shown in Fig. 5.4a. We used a *fixed relative length design* to study the distribution of bubbles over the eight parallel exit channels. The width of the feed channel is $w_0 = 100\,\mu\mathrm{m}$. To fix the relative length of the droplets, we narrowed the channels leading to the second and third generation of T-junctions to $w_1 = 71\,\mu\mathrm{m}$ and $w_2 = 50\,\mu\mathrm{m}$, respectively. The fabrication inaccuracy in the widths of the channels is below $1\,\mu\mathrm{m}$. To quantify the effect of pressure equalizers, we studied the distribution of bubbles in devices without and with bypass channels around the T-junctions (Fig. 5.4c). The height of the channels in the devices with and without bypass were $h = 41 \pm 1\,\mu\mathrm{m}$ and $h = 43 \pm 1\,\mu\mathrm{m}$ respectively. We complemented the experiments in the multi-junction devices with experiments performed in single T-junctions to reveal the influence of the height-to-width ratio of the channels on the transition line between

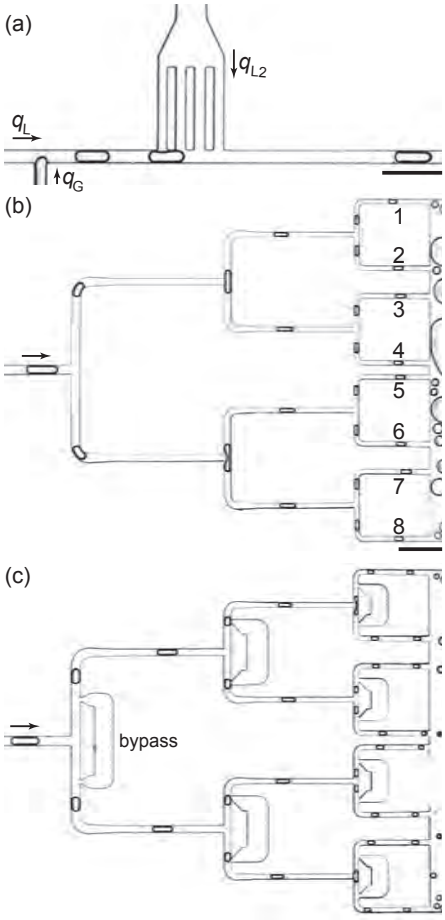

Figure 5.4 (a) A steady stream of bubbles is produced at a T-junction from a stream of gas and liquid injected at flow rates q_G and q_L. The additional liquid stream injected from the side channel at a rate q_{L2} enables the independent control of the size and speed of the bubbles and their distance apart. Once spaced out, the bubbles are distributed over 8 parallel channels by splitting them at three successive junctions, without (b) and with (c) a bypass channel. Scale bars: $500\,\mu\mathrm{m}$.

breakup and non-breakup. We used three single T-junction splitters with aspect ratios of h/w = 0.27, 0.59 and 0.94.

We used HFE-7500 (3M, $\mu = 1.2\,\mathrm{mPas}, \gamma = 16.2\,\mathrm{mN/m}$) and air as working fluids, without the addition of surfactants. The liquid flow rates were controlled using two individual syringe pumps (Harvard pico plus 11). The flow rates were in the range

$3 < q_L < 20\,\mu\mathrm{m/min}$ and $4 < q_{L2} < 100\,\mu\mathrm{m/min}$. A steady air flow was supplied from a fixed pressure source and controlled using a reducing valve in the range between 2 and $6\,\mathrm{bar}$. Air was injected into the microfluidic device through a $4-7\,\mathrm{m}$ long capillary tube with internal diameter of $25\,\mu\mathrm{m}$. The pressure drop over this tube is much larger than the pressure drop over the chip. This ensures a steady air flow rate, which is independent of (temporal) events in the chip such as bubble breakup. We confirm that for the range of gas and liquid flow rates used in this work, we did not observe fluctuations in the speed of bubbles caused by pressure fluctuations arising from the gas pressure source or the mechanics of the syringe pump. To image the flow, we used a high speed camera (Phantom V9.1, Vision Research) attached to an inverted microscope (Axiovert 200M, Zeiss). We extracted the length of the bubbles, their distance apart, and their velocity from the images. We used a magnification and frame rate such that the inaccuracy in the length and velocity measurements is below 2%.

5.4 Results

5.4.1 Influence of non-breaking bubbles on size uniformity

In a first set of experiments, we studied the influence of non-breaking bubbles on size uniformity. To study this influence separately from the influence of flow asymmetries caused by fabrication inaccuracies, we operated the device at sufficiently large values of $(l_s/w)_0 \cdot Ca_0^{1/3}$ such that the contribution of flow asymmetries to the coefficient of variation is negligible. For typical fabrication inaccuracies in this work ($u(h)/h < 0.02$), this requires that we operated the device beyond $(l_s/w)_0 \cdot Ca_0^{1/3} > 1.75$ as can be seen from Fig. 5.2b.

Based on the model in section 5.2.2, we expect that the coefficient of variation is small in case all bubbles break ($\eta = 1$). This, in turn, is expected when the device is operated such that the capillary number is beyond the critical capillary number at all T-junctions. For the fixed relative length design used in this study, the capillary number, Ca_2, at the final generation of T-junctions is the smallest. We hence expect small coefficients of variation for $Ca_2 > Ca_{\mathrm{crit}}$. By contrast, CV_{out} is expected to sharply increase for decreasing η. We tested these hypotheses by measuring CV_{out} as a function of Ca. To this end, we recorded movies at the eight exit channels and measured the length of all bubbles flowing through each exit channel for a given time window. We adjusted Ca such that the length of the bubbles in the feed stream is comparable in all experiments ($3.1 < l_0/w_0 < 3.8$). We used the average bubble lengths measured upstream of the last junctions to calculate the critical value of the capillary number for each experiment based on Leshansky's relation $Ca_{\mathrm{crit}} = a(l/w)^b$, where we used $a = 0.98$ and $b = -3.60$ as explained later in section 5.4.4.

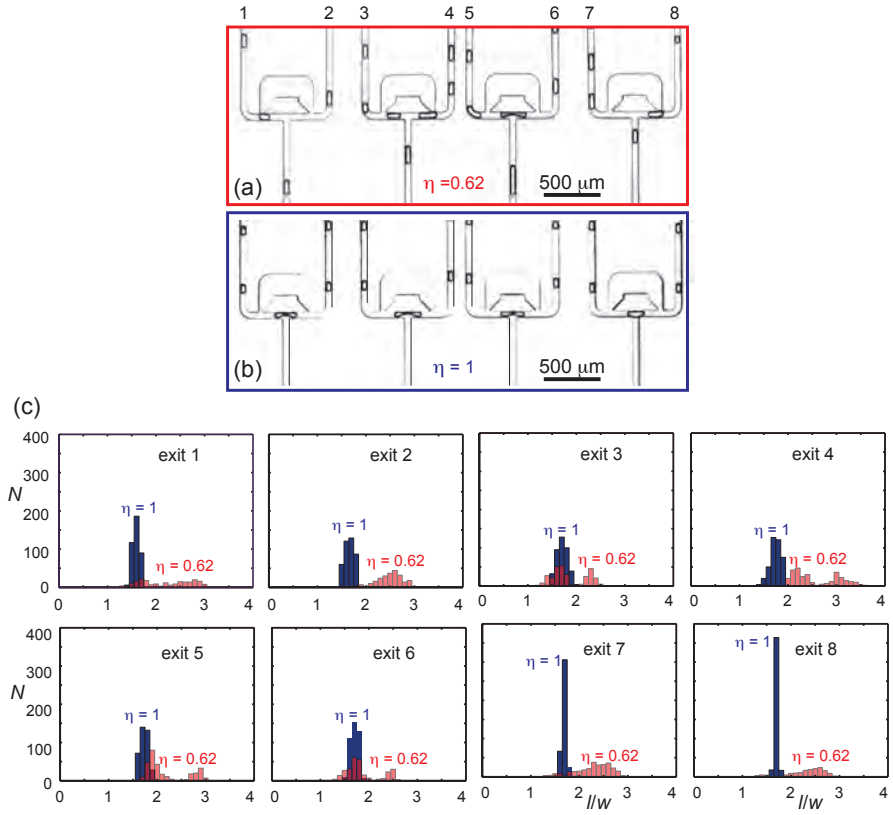

Figure 5.5 (a) Snapshot of the 8 exiting channels for a multi-junction device operated at $Ca_2 = Ca_0/2 = 4.9 \cdot 10^{-3} < Ca_{\text{crit}} = 1.4 \cdot 10^{-2}$ such that a fraction of bubbles, $\eta = 0.62$, breaks. Bubble and slug lengths: $(l_0/w_0, l_s0/w_0)$ = (3.2, 8.8). (b) Snapshot for $Ca_2 = Ca_0/2 = 1.3 \cdot 10^{-2} > Ca_{\text{crit}} = 1.1 \cdot 10^{-2}$ with all bubbles breaking ($\eta = 1$). Bubble and slug lengths: $(l_0/w_0, l_s0/w_0)$ = (3.3, 16).(c) Corresponding histograms of the relative bubble length l/w measured in the eight exit channels.

For capillary numbers below the critical capillary number, we indeed find that a significant fraction of bubbles fed to the distributor does not breakup as illustrated in the snapshot of the eight exit channels in Fig. 5.5a. By contrast, all bubbles break $(\eta = 1)$ when operating the device beyond the critical capillary number (Fig. 5.5b). The corresponding histograms of the bubble length measured at the eight exit channels show a large spread in bubble length for the case $Ca < Ca_{\text{crit}}$, while a narrow size distribution is obtained for $Ca > Ca_{\text{crit}}$ as shown in Fig. 5.5c. For these two examples, the corresponding values of the coefficient of variation based on all bubbles leaving the

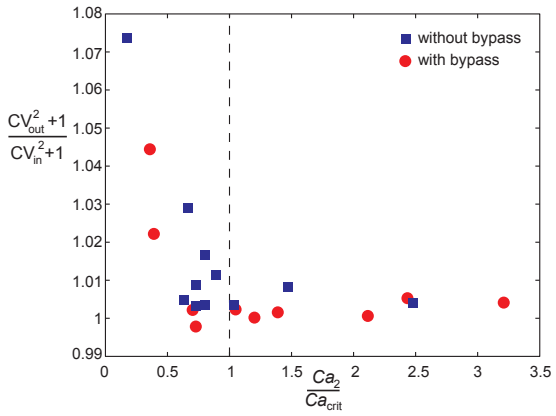

Figure 5.6 Influence of non-breaking bubbles on the coefficient of variation CV_{out} of bubbles leaving a multi-junction device with (red circles) and without (blue squares) bypass. For $Ca_2 > Ca_{\text{crit}}$, all bubbles break resulting small CV_{out}. For $Ca_2 < Ca_{\text{crit}}$, CV_{out} sharply increases with decreasing Ca_2.

device are $CV_{\text{out}} = 0.21$ and $CV_{\text{out}} = 0.05$, respectively.

In addition to the two examples shown in Fig. 5.5a, we further illustrate the influence of Ca on CV_{out} for a wider range of Ca/Ca_{crit}. For $Ca_2/Ca_{\text{crit}} > 1$, we find that the coefficient of variation is small and independent of Ca_2 (Fig. 5.6). For $Ca_2/Ca_{\text{crit}} < 1$, CV_{out} sharply increases with decreasing Ca_2. We observe the same behavior for devices with and without bypass channels around the T-junctions. Without further elaborating on the influence of the bypass, which will be done in a separate section (5.4.3), we conclude that this set of experiments clearly stresses the importance of operating the device beyond the critical value of the capillary number such that break up is ensured at all T-junctions.

5.4.2 Influence of flow asymmetries on size uniformity

We now turn our attention to bubble size uniformities caused by asymmetries in flow due to fabrication inaccuracies. To distinguish between this source of variation and the influence of non-breakup, we performed a second set of experiments in which we ensured that all bubbles broke, i.e. $\eta = 1$.

For devices without a bypass, we expect that the coefficient of variation depends on $(l_s/w)_0 \cdot Ca_0^{1/3}$ according to Eqns. 5.5 and 5.6. To test our model, we varied this parameter in the range 1.2 -18. As shown in Fig. 5.7, the coefficient of variation found experimentally (blue squares) quantitatively agrees with our theoretical model;

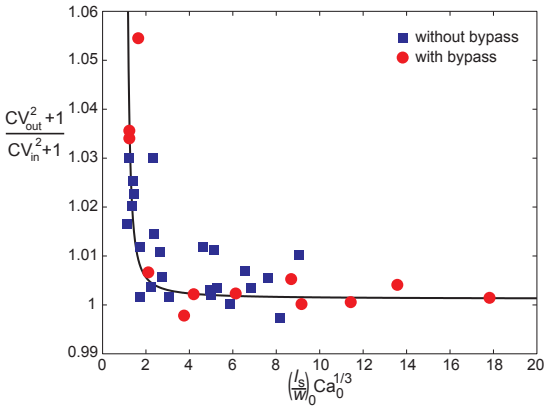

Figure 5.7 Influence of flow asymmetries due to fabrication inaccuracies on the coefficient of variation CV_{out} of bubbles leaving a multi-junction device with (red circles) and without (blue squares) bypass. Good agreement is found between the experimental results and the theoretical model (Eqns. (5.5) and (5.6)), where we used $C=3.58$ and a measured value of the fabrication inaccuracies of $u(h)/h=0.02$.

CV_{out} is nearly constant for larger values of $(l_s/w)_0 \cdot Ca_0^{1/3}$ and steeply increases with decreasing $(l_s/w)_0 \cdot Ca_0^{1/3}$ for values below 2.

For the device with the bypass, we expect that the value at large $(l_s/w)_0 \cdot Ca_0^{1/3}$ is nearly the same as in the device without a bypass, given the fabrication error is small. This is indeed what we find experimentally. Moreover, we find that the data for the devices with and without bypass collapses on the same curve over the entire range of $(l_s/w)_0 \cdot Ca_0^{1/3}$. The reason the data also collapse for small $(l_s/w)_0 \cdot Ca_0^{1/3}$ is that the distance between the bubbles becomes smaller than the distance between the T-junction and the exit of the bypass (l_{bp}, see Fig. 5.3). Consequently, the bypass is blocked by the bubble that precedes the bubble arriving at the T-junction. Obviously, this closes the bypass such that for short slugs ($l_s < l_{bp}$), flow asymmetries propagate the same in devices with and without a bypass. In the next section, we further investigate the influence of the bypass.

Finally, we evaluate how the coefficient of variation grows from generation to generation. For the present design, the leading contribution to CV_{out} is the asymmetric breakup at the final generation as shown in Fig. 5.2b. To verify this prediction, we measured the coefficient of variation of the bubbles entering the first, second, and third generation as well as the CV of the bubbles leaving the third generation. As expected, the primary increase in CV occurs in the final generation. This effect becomes more pronounced with decreasing $(l_s/w)_0 \cdot Ca_0^{1/3}$ as shown in Table 5.1.

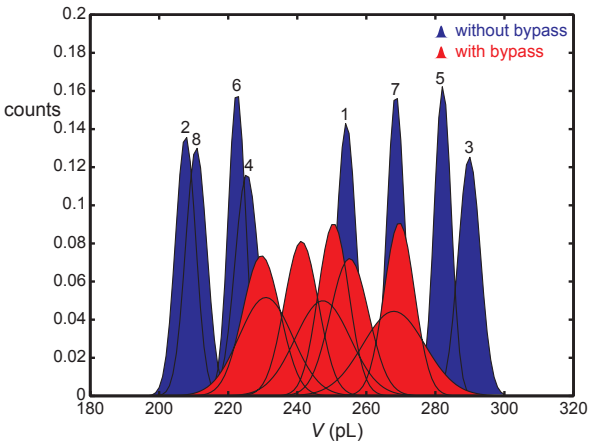

Figure 5.8 Histograms of 1000 successive bubbles measured at the eight individual exits of devices with (red) and without (blue) bypass. Normalization was done by dividing the number of counts by 1000. To demonstrate that incorporating a bypass has an advantage for large fabrication tolerances, we designed these devices such that exit channels 1, 3, 5, and 7 were 20% wider than exit channels 2, 4, 6, and 8. Conditions: l_0/w=4.3; Ca_0=0.028; $(l_s/w)_0$=25 and 36 for the devices with and without the bypass respectively.

5.4.3 Influence of the bypass

For the devices used in this study with fabrication tolerances below 2%, we have shown experimentally and theoretically that incorporating a bypass has a negligible advantage. For larger fabrication tolerances, we do expect that the bypass significantly reduces flow asymmetries. To test this hypothesis, we fabricated devices with and without a bypass and introduced a large fabrication error by design: in these devices, we increased the width of the straight channels leading to exits 1, 3, 5, and 7 (see Fig. 5.4) by 20%. For the device without the bypass, we expect that the volume of the bubbles is about 20% larger in the wider channels leading to a coefficient of variation of $CV_{\text{out}} \sim 0.1$. For the device with bypass, we expect that the splitting ratio of bubbles is not affected by the difference in width downstream of the T-junction.

Table 5.1 Increase in CV from generation to generation for bubbles breaking in a three-generation bubble splitter with bypass.

$(l_s/w)_0 \cdot Ca_0^{1/3}$	Ca_0	l/w	CV_{in}	CV_1	CV_2	CV_{out}
3.8	0.014	3.6	0.03	0.02	0.03	0.05
2.1	0.011	4.8	0.03	0.03	0.04	0.09
1.6	0.020	3.8	0.03	0.02	0.03	0.24

We measured the length of 1000 successive bubbles in each exit channel and used it to calculate the bubble volume using the simple approximation $V = hwl$. The bubble size in each exit channel shows a Gaussian distribution. We plot these Gaussian shapes for the devices with and without the bypass in Fig. 5.8. For the device without bypass, we indeed find that the mean bubble volumes in exit channels 1, 3, 5, and 7 deviate roughly 25% from the mean bubble volumes in the even channels. This translates into a coefficient of varation of all bubbles leaving the device of $CV_{\text{out}} = 0.13$. As expected, the deviations between the mean bubble volume in the exit channels of the bypass channels is much smaller ($CV_{\text{out}} = 0.06$). We hence conclude that incorporating a bypass reduces nonuniformities in bubbles size caused by fabrication errors, but only when fabrication tolerances are significant.

5.4.4 Influence of heigh-to-width ratio on critical capillary number for a single T-junction

In the previous set of experiments, we estimated the critical capillary number using the relations available in literature and have verified that indeed all bubbles break. A question particularly relevant to planar multi-junction device in which the width of the successive junctions decreases is whether the critical value of the capillary number depends on the height-to-width ratio of the channel. We studied the influence in a single T-junction device for aspect ratios in the range of those encounted in the multi-junction device. The breakup maps are shown in 5.9a-c. We fitted the transition between non-breaking bubbles (open symbols) and breaking bubbles (closed symbols) using the function $Ca_{\text{crit}} = a(l/w)^b$ as proposed by Leshansky and Pismen [35]. This resulted in $a = 0.98 \pm 0.23$ and $b = -3.60 \pm 0.27$ for $h/w = 0.94$, $a = 0.41 \pm 0.04$ and $b = -2.79 \pm 0.12$ for $h/w = 0.59$, and $a = 0.26 \pm 0.06$ and $b = -2.66 \pm 0.22$ for $h/w = 0.28$. The intervals hereby indicate the 95% confidence interval of the fits. A comparison of the three fits (Fig. 5.9d) reveals that the critical capillary number not only depends on the bubble length, but also on the height-to-width ratio of the T-junction. This fact is particularly relevant for planar multi-junction devices in which the height-to-width ratio is different for all successive junctions.

5.5 Conclusions

In this chapter, we presented a theoretical and experimental study on the design and operation of a bubble distributor, which can be used for the scale-out of segmented flow microreactors. We systematically studied how the uniformity of bubble size in the exit channels depends on the operating conditions. We identified three main sources leading to nonuniformities: nonuniformity in the size of bubbles fed to the distributor, nonuniformities caused by non-breaking bubbles, and nonuniformities caused

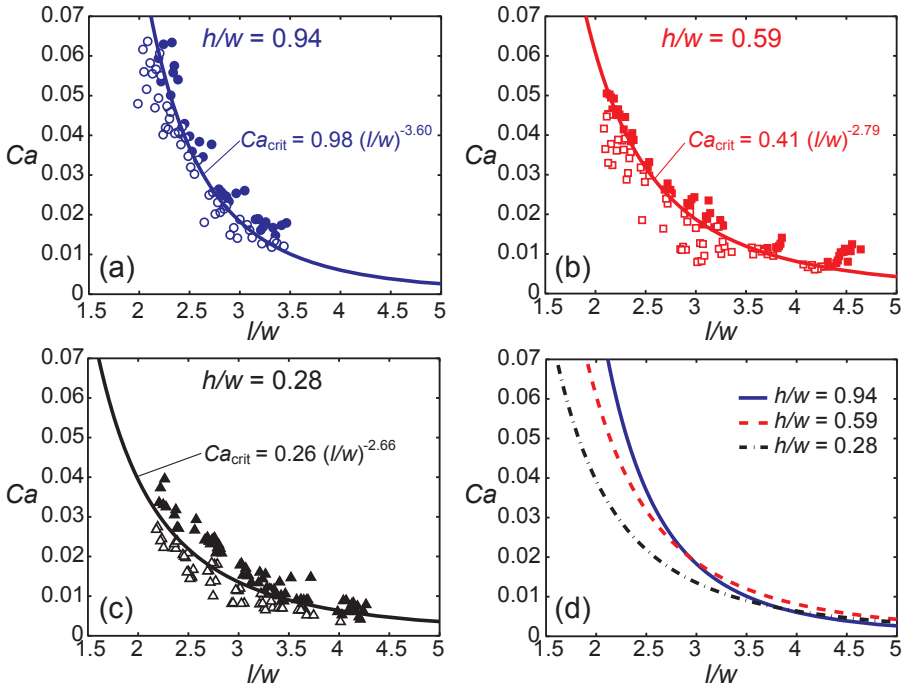

Figure 5.9 Breakup map obtained in single T-junctions with different height-to-width ratios: (a) $h/w = 0.94$, (b) $h/w = 0.59$, (c) $h/w = 0.28$. Breaking and non-breaking bubbles are indicated by closed and open symbols respectively. The solid lines are fits of the functional form proposed by Leshansky and Pismen [35] $Ca_{\text{crit}} = a(l/w)^b$. (d) Overview clearly reveals the height-to-width ratio dependence on the critical capillary number of the channels $Ca_{\text{crit}} = f(l_s/w, h/w)$. Geometries: $(h, w) = (81, 300), (94, 160), (85, 90)\,\mu\text{m}$.

by asymmetries in flow due to fabrication inaccuracies. We showed both theoretically and experimentally that even a small fraction of non-breaking bubbles leads to bubble populations with large polydispersities. The device should hence be designed and operated such that non-breaking events are avoided; for planar devices, we have argued that a design that keeps the relative bubble length constant in all generations is favourable over other types of designs. Operating the device such that the capillary number corresponding to the bubble velocity at the last generation of T-junctions is larger than the critical capillary number ensures that all bubbles break. Our experiments confirm that this critical capillary number depends on the length of the incoming bubbles, and reveal that it also depends on the height-to-width ratio of the T-junction. This finding is particularly relevant for planar multi-junction distributors, because h/w is different at all successive junctions.

Ensuring that all bubbles break ($Ca > Ca_{\text{crit}}$) is a necessary but not sufficient condition to ensure a uniform bubble size in all parallel channels. We also quantified the nonuniformities caused by asymmetries in flow due to fabrication inaccuracies. Our theoretical analysis shows that nonuniformities caused by fabrication inaccuracies mainly depend on $(l_s/w)_0 \cdot Ca_0^{1/3}$. This analysis shows that large nonuniformities are expected for $(l_s/w)_0 \cdot Ca_0^{1/3} < 2$ for fabrication tolerances of 2%. Good agreement was found between this prediction and our experiments, leading to the second operating guideline that $(l_s/w)_0 \cdot Ca_0^{1/3} > 2$. We have furthermore clarified whether including bypass channels around the T-junctions reduces flow asymmetries and corresponding nonuniformities in bubble size. While bubble nonuniformities in devices with and without bypass channels are comparable for fabrication tolerances of a few percent, we conclude that incorporating a bypass channels does have an beneficial effect for larger fabrication tolerances.

Bibliography

[1] J. R. Burns and C. Ramshaw. The intensification of rapid reactions in multiphase systems using slug flow in capillaries. *Lab Chip*, 1:10–15, 2001.

[2] J. Kobayashi, Y. Mori, K. Okamoto, R. Akiyama, M. Ueno, T. Kitamori, and S. Kobayashi. A microfluidic device for conducting gas-liquid-solid hydrogenation reactions. *Science*, 304:1305–1308, 2004.

[3] D. Dendukuri and P. S. Doyle. The synthesis and assembly of polymeric microparticles using microfluidics. *Adv. Mater.*, 21(41):4071–4086, 2009.

[4] S. A. Khan, A. Günther, M. A. Schmidt, and K. F. Jensen. Microfluidic synthesis of colloidal silica. *Langmuir*, 20:8604–8611, 2004.

[5] S. Marre and K. F. Jensen. Synthesis of micro and nanostructures in microfluidic systems. *Chem. Soc. Rev.*, 39(3):1183–1202, 2010.

[6] H. C. Shum, A. R. Abate, D. Lee, A. R. Studart, B. Wang, C.H. Chen, J. Thiele, R. K. Shah, A. Krummel, and D. A. Weitz. Droplet microfluidics for fabrication of non-spherical particles. *Macromol. Rapid Comm.*, 31(2):108–118, 2010.

[7] J. Zhang, R. J. Coulston, S. T. Jones, J. Geng, O. A. Scherman, and C. Abell. One-step fabrication of supramolecular microcapsules from microfluidic droplets. *Science*, 335:690–694, 2012.

[8] K. Martin, T. Henkel, V. Baier, A. Grodrian, T. Schön, M. Roth, J. M. Köhler, and J. Metze. Generation of larger numbers of separated microbial populations by cultivation in segmented-flow microdevices. *Lab Chip*, 3:202–207, 2003.

[9] J. J. Agresti, E. Antipov, A. R. Abate, K. Ahn, A. C. Rowat, J. C. Baret, M. Marquez, A. M. Klibanov, Griffiths A. D., and D. A. Weitz. Ultrahigh-throughput screening in drop-based microfluidics for directed evolution. *Proc. Natl. Acad. Sci. U. S. A.*, 107:4004–4009, 2010.

[10] A. B. Theberge, F. Courtois, Y. Schaerli, M. Fischlechner, C. Abell, F. Hollfelder, and W. T. S. Huck. Microdroplets in microfluidics: An evolving platform for discoveries in chemistry and biology. *Ang. Chem. - Int. Ed.*, 49:2–25, 2010.

[11] M. T. Guo, A. Rotem, J. A. Heyman, and D. A. Weitz. Droplet microfluidics for high-throughput

biological assays. *Lab Chip.*, 12:2146–2155, 2012.

[12] A. Günther and K. F. Jensen. Multiphase microfluidics: from flow characteristics to chemical and material synthesis. *Lab Chip*, 6:1487–1503, 2006.

[13] C. Holtze. Large-scale droplet production in microfluidic devices - an industrial perspective. *J. Phys. D: Appl. Phys.*, 46:114008, 2013.

[14] V. Barbier, H. Willaime, and P. Tabeling. Producing droplets in parallel microfluidic systems. *Phys. Rev. E.*, 74:046306, 2006.

[15] V. Haverkamp, V. Hessel, H. Löwe, G. Menges, M. J. F. Warnier, E. V. Rebrov, M. H. J. M. de Croon, J. C. Schouten, and M. A. Liauw. Hydrodynamics and mixer-induced bubble formation in micro bubble columns with single and multiple-channels. *Chem. Eng. Technol.*, 29:1015–1026, 2006.

[16] W. Li, E. W. K. Young, M. Seo, Z. Nie, Garstecki. P., C. A. Simmons, and E. Kumacheva. Simultaneous generation of droplets with different dimensions in parallel integrated microfluidic droplet generators. *Soft Matter*, 4:258–262, 2008.

[17] N. de Mas, A. Günther, T. Kraus, M. A. Schmidt, and K. F. Jensen. Scaled-out multilayer gas-liquid microreactor with integrated velocimetry sensors. *Ind. Eng. Chem. Res.*, 44(24):8997–9013, 2005.

[18] M. K. Mulligan and J. P. Rothstein. Scale-up and control of droplet production in coupled microfluidic flow-focusing geometries. *Microfluid Nanofluid*, 13:65–73, 2012.

[19] T. Nisisako, T. Torii, T. Takahashi, and Y. Takizawa. Synthesis of monodisperse bicolored janus particles with electrical anisotropy using a microfluidic co-flow system. *Adv. Mater.*, 18:1152–1156, 2006.

[20] T. Nisisako and T. Torii. Microfluidic large-scale integration on a chip for mass production of monodisperse droplets and particles. *Lab Chip*, 8(2):287–93, 2008.

[21] M. B. Romanowsky, A. R. Abate, A. Rotem, C. Holtze, and D. A. Weitz. High throughput production of single core double emulsions in a parallelized microfluidic device. *Lab Chip*, 12:802–807, 2012.

[22] A. M. Nightingale, J. H. Bannock, S. H. Krishnadasan, F. T. F. O'Mahony, S. A. Haque, J. Sloan, C. Drury, R. McIntyrec, and J. C. deMello. Large-scale synthesis of nanocrystals in a multichannel droplet reactor. *J. Mater. Chem. A*, 1:4067–4076, 2013.

[23] J. Yue, R. Boichot, L. Luo, Y. Gonthier, G. Chen, and Q. Yuan. Flow distribution and mass transfer in a parallel microchannel contactor integrated with constructal distributors. *AIChE J.*, 56:298–317, 2010.

[24] M. Al-Rawashdeh, L.J.M. Fluitsma, T.A. Nijhuis, E.V. Rebrov, V. Hessel, and J.C. Schouten. Design criteria for a barrier-based gas-liquid flow distributor for parallel microchannels. *Chem. Eng. J.*, 181-182:549 – 556, 2012.

[25] K. C. van Dijke, G. Veldhuis, K. Schroën, and R. M. Boom. Parallelized edge-based droplet generation (EDGE) devices. *Lab Chip*, 9:2824–2830, 2009.

[26] R. Dangla, S. C. Kayi, and C. N. Baroud. Droplet microfluidics driven by gradients of confinement. *Proc. Natl. Acad. Sci. U. S. A.*, page early edition, 2013.

[27] V. van Steijn, P. M. Korczyk, L. Derzsi, A. R. Abate, D. A. Weitz, and P. Garstecki. Block-and-break generation of microdroplets with fixed volume. *Biomicrofluidics*, 7, 2013.

[28] M. Al-Rawashdeh, F. Yu, T. A. Nijhuis, E. V. Rebrov, V. Hessel, and J. C. Schouten. Numbered-up gas-liquid micro/milli channels reactor with modular flow distributor. *Chem. Eng. J.*, 207(SI): 645–655, OCT 1 2012.

[29] D. N. Adamson, D. Mustafi, J. X. J. Zhang, B. Zheng, and R. F. Ismagilov. Production of arrays of chemically distinct nanolitre plugs via repeated splitting in microfluidic devices. *Lab Chip*, 6: 1178–1186, 2006.

[30] A. R. Abate and D. A. Weitz. Faster multiple emulsification with drop splitting. *Lab Chip*, 11(11): 1911–5, 2011.

[31] C. Amador, A. Gavriilidis, and P. Angeli. Flow distribution in different microreactor scale-out geometries and the effect of manufacturing tolerances and channel blockage. *Chem. Eng. J.*, 101(1-3): 379–390, 2004.

[32] K. Kawai, M. Fujii, J. Uchikoshi, K. Arima, S. Shoji, and M. Morita. Continuous generation of femtolitre droplets using multistage dividing microfluidic channel. *Curr. Appl. Phys.*, 12(3):S33–S37, DEC 2012.

[33] T. Moritani, M. Yamada, and M. Seki. Generation of uniform-size droplets by multistep hydrodynamic droplet division in microfluidic circuits. *Microfluid. Nanofluid.*, 11(5):601–610, NOV 2011.

[34] D. Link, S. Anna, D. Weitz, and H. Stone. Geometrically mediated breakup of drops in microfluidic devices. *Phys. Rev. Lett.*, 92(5), 2004.

[35] A. M. Leshansky and L. M. Pismen. Breakup of drops in a microfluidic T junction. *Phys. Fluids*, 21 (2):023303, 2009.

[36] S. Afkhami, A. M. Leshansky, and Y. Renardy. Numerical investigation of elongated drops in a microfluidic T-junction. *Phys. Fluids*, 23(2):022002, 2011.

[37] A. Bedram and A. Moosavi. Droplet breakup in an asymmetric microfluidic T junction. *Eur. Phys. J. E*, 34:78, 2011.

[38] Y. X. Zhang and L. Q. Wang. Nanoliter-droplet breakup in confined T-Shaped junctions. *Curr. Nanosci.*, 7(3):471–479, 2011.

[39] T. Fu, M. Youguang, D. Funfschilling, and H. Z. Li. Dynamics of bubble breakup in a microfluidic T-junction divergence. *Chem. Eng. Sci.*, 66:4184ï£¡4195, 2011.

[40] M. de Menech. Modeling of droplet breakup in a microfluidic T-shaped junction with a phase-field model. *Phys. Rev. E*, 73:031505, 2006.

[41] M. C. Jullien, M. J. Tsang Mui Ching, C. Cohen, L. Menetrier, and P. Tabeling. Droplet breakup in microfluidic T-junctions at small capillary numbers. *Phys. Fluids*, 21(7):072001, 2009.

[42] H. Song, J. D. Tice, and R. F. Isgmagilov. A microfluidic system for controlling reaction networks in time. *Angew. Chem. Int. Edit.*, 42:768–772, 2003.

[43] J. Nie and R. T. Kennedy. Sampling from nanoliter plugs via asymmetrical splitting of segmented flow. *Anal. Chem.*, 82:7852–7856, 2010.

[44] B. Verbruggen, T. Tóth, Y. T. Atalay, F. Ceyssens, P. Verboven, R. Puers, B. Nicolai, and J. Lammertyn. Design of a flow-controlled asymmetric droplet splitter using computational fluid dynamics. *Microfluid. Nanofluid.*, page Online first, 2013.

[45] M. Yamada, S. Doi, and H. Maenaka. Hydrodynamic control of droplet division in bifurcating microchannel and its application to particle synthesis. *J. Colloid Interface Sci.*, 321:401–407, 2008.

[46] M. J. Fuerstman, A. Lai, M. E. Thurlow, S.S. Shevkoplyas, H. A. Stone, and G. M. Whitesides. The pressure drop along rectangular microchannels containing bubbles. *Lab Chip*, 7:1479–1489, 2007.

[47] V. van Steijn, M.T. Kreutzer, and C.R. Kleijn. Velocity fluctuations of segmented flow in microchannels. *Chem. Eng. J.*, 135(0):S159 – S165, 2008.

[48] P. Parthibana and S. A. Khan. Filtering microfluidic bubble trains at a symmetric junction. *Lab Chip*, 12:582–588, 2012.

[49] F. P. Bretherton. The motion of long bubbles in tubes. *J. Fluid Mech.*, 10(02):166–188, 1961.

[50] H. Wong, C. J. Radke, and S. Morris. The motion of long bubbles in polygonal capillaries. Part 1. Thin films. *J. Fluid Mech.*, 292:71–94, 1995.

[51] D.C. Duffy, J. C. McDonald, O. J. A. Schueller, and G. M. Whitesides. Rapid prototyping of microfluidic systems in poly(dimethylsiloxane). *Anal. Chem.*, 79:4974–4984, 1998.

6. Epilogue

The purpose of this chapter is to highlight some of our main findings and discuss them in a broader perspective. The chapter starts with a discussion on the generality of those findings: 1) surface-tension-driven pinching, 2) 3D versus 2D, 3) the role of CFD in unraveling the breakup phenomena and 4) scale-up of segmented flow microreactors. We then conclude the chapter by proposing some opportunities for future research.

6.1 General conclusions

This thesis comprises computational and experimental studies of the breakup of bubbles and droplets in confined microfluidic systems. The main contribution of the thesis is to reveal the breakup mechanism. The understanding of the breakup mechanism allowed us to successfully design and characterize a droplet-splitting distributor. We now spend a few words to discuss some of our main findings in a broader perspective.

Surface-tension-driven pinching The breakup of confined droplets comprises two phases: (i) a squeezing phase in which the droplet interface is continuously compressed by an external flow and (ii) a rapid-pinching phase in which the neck of the thread collapses at an accelerated rate. The rapid pinching is a consequence of a surface-tension-driven flow associated with the curvature variation along the surface of the droplet. The onset of this rapid pinching begins when the curvature at the center of the neck becomes larger than the curvature everywhere else. We also observed that the neck of the thread deforms locally during the rapid pinching. We now argue that similar mechanism is expected to drive the breakup of the liquid thread in other configurations, *viz.* the formation of bubbles in a T-junction[1,2] or flow-focusing device[3,4] or the breakup of droplets in Y-junction[5].

The breakup of the liquid thread in the above flow configurations shares many similarities with the breakup process described in this thesis. It also comprises two distinct phases: squeezing and rapid-pinching phases. A local constriction of the liquid thread around the pinching point was observed in all flow configurations. van Steijn et al.[2] experimentally observed a flow reversal towards the center of the thread that accelerates the pinching rate for the formation of bubbles in T-junctions. We therefore can expect that the rapid pinching reported in these flow configurations is also driven by the difference of the curvature along the droplet. A measurement of the flow velocity and three-dimensional shape of the droplet is useful to validate the applicability of our finding in addition to stop-flow simulations.

3D versus 2D In chapter 3, we have shown that in the squeezing phase, the behavior of droplets in 2D simulations is similar to that in 3D simulations. However, the rapid-pinching stage was only observed in 3D simulations. This leads to a much longer breakup time in 2D simulations. Chapter 4 shows that whether the droplet breaks or not in physical experiments or full-T-junction simulations is controlled by the ratio between the breakup time and the drifting time. Hence, the overestimation of the breakup time in 2D simulations leads to an overestimation of the critical capillary number. We indeed observed that with the same fluid properties and channel geometries, the critical capillary number in 2D simulations is approximately three times larger than that in 3D simulations (square channel) for a droplet of length $l/w = 2.8$. These findings clearly illustrate the limitations of 2D simulations.

We now discuss the relevance of this finding in another phenomena, the formation

of bubbles/droplets in microfluidic systems. In the formation process, the size of the generated bubbles/droplets is proportional to the timescale of the breakup of the liquid thread. A longer breakup time will lead to a bigger bubble/droplet. Therefore, numerical studies of the formation of bubbles and droplets in microfluidics have to be conducted with 3D simulations to capture the correct physics and to obtain accurate bubble/droplet volumes.

The role of CFD in unraveling the breakup phenomena In this thesis, CFD has been used extensively to unravel the physics behind droplet breakup. CFD provides a powerful tool to verify some of our hypotheses. For instance, in chapter 3, we found that the rapid pinching is driven by capillary effects alone. This hypothesis was verified using stop-flow simulations in which we extracted the shape of the droplet from the full simulation at different instances, set the velocity in the internal and external fluid to zero, and then restarted the computation. These simulations allowed us to eliminate the influence of other forces than capillary effects on the rapid pinching. Another example illustrating the power of CFD is the perturbation-free simulation presented in chapter 4. To obtain accurate critical capillary numbers for the breakup and to eliminate perturbations in the system, we utilized symmetric-boundary-condition simulations. With these simulations, we successfully simulated the steady state of non-breaking droplets and computed the critical capillary number with an accuracy of within 0.5%.

The simulations presented in this thesis were performed with the Volume of Fluid (VOF) method. In chapter 2, we have shown that with appropriate computational settings, this method can provide sufficiently accurate results which allow us to investigate the fundamental physics behind the breakup phenomena. Even though we have improved the performance of the implemented VOF method with a smoother, its well-known issue, the parasitic current, still exists. An analysis of the magnitude of the parasitic current showed that it increases with a decreasing capillary number[6]. In most of our simulations, the capillary number varies from 10^{-3} to 10^{-1}. This can lead to the parasitic currents with a magnitude of approximately a hundred times larger than the mean flow velocity at low capillary numbers. Due to the parasitic currents, the computational time step in our simulations is limited to approximately $1\,\mu s$. For low capillary number cases ($Ca < 10^{-3}$), this leads to a very high computational cost. In such cases, approaches such as CLSVOF (Coupled Level Set/Volume-of-Fluid) method[7] or MMIT (Moving Mesh Interface Tracking) method[8,9] might be better choices. For high capillary number flows ($Ca > 10^{-3}$), the VOF is still a reasonably good choice due to its capability of handling topological changes and the ease of implementation.

Scale-up of segmented flow microreactors One of the goals of this thesis project was to design a bubble-splitting distributor, which can be used to evenly distribute a stream of bubbles or droplets over a network of microchannels. This was achieved by splitting these bubbles and droplets with a series of successive splitters. We have studied three strategies to a design planar bubble-splitting distributor based on either a fixed channel

width, a fixed capillary number, or a fixed relative bubble length. We have identified the most suitable design strategy to ensure the breakup in all generations for a device with three generations (8 exits). We now shortly address the question whether we can use this strategy for further scale-out.

A limitation of the current planar type of distributor is the difficulty to indefinitely number up the splitting generations. The further we scale up, the higher flow velocity we have to feed to the system to ensure 100% breakup. Suo and Griffith [10] showed that at $Ca > 0.35$, segmented flow is transformed to bubbly slug flow. Thus, this imposed an upper range on the operating condition and the number of splitting generations for a planar device. For example, with the fixed relative length device, to get the final droplet length $l/w = 3$ (which leads to $Ca_{crit} = 1.1 \times 10^{-2}$ for air-HFE7500 system), the maximum number of splitting generations is 6 (64 outlets) to ensure segmented flow in the whole device. This limitation can be eased by using a design in which the capillary number and relative droplet length are kept constant. This is possible in non-planar devices and can for instance be achieved by keeping the width of the channel constant while reducing the height of the channel with a factor 2 after each generation. Even with such a device, the limitation in the number of splitting generations still exists. For example, with a feed channel of size $1000\text{x}1024\,\mu\text{m}^2$, after 10 generations (1024 outlets), the size of the channel will be $1000\text{x}1\,\mu\text{m}^2$. Fabrication of such a high aspect ratio channel with acceptable accuracy will be extremely difficult.

6.2 Research opportunities

We conclude this thesis by highlighting some opportunities for future research.

Debate on the transition line between breakup and non-breakup regime It has been shown in literature that the transition line between the breaking and the non-breaking regime depends on the capillary number *Ca*, the ratio between the initial droplet length and the channel width l/w, the viscosity ratio $\lambda = \hat{\mu}/\mu$, and the aspect ratio of the T-junction (this thesis).

Link et al. [11] used a Rayleigh-Plateau argument to develop a semi-analytical model to predict the transition line between the breakup and the non-breakup regime according to: $Ca_{\text{crit}} \sim \epsilon(1/\epsilon^{2/3} - 1)^2$ where $\epsilon = l/\pi w$. According to their model, droplets that are longer than their circumference always break. Their model was confirmed by their experimental data. However, their experiments were performed for relatively large *Ca* ($Ca > 5 \times 10^{-2}$). For smaller *Ca* ($10^{-4} < Ca < 10^{-2}$), later experiments by Jullien et al. [12] and Fu et al. [13] showed that the model significantly deviates for low *Ca*. Additionally, these experiments falsified Link's hypothesis that droplets that are longer than their circumference always break. Their experiments suggested another upper limit of the droplet length beyond which a droplet will also always break, as

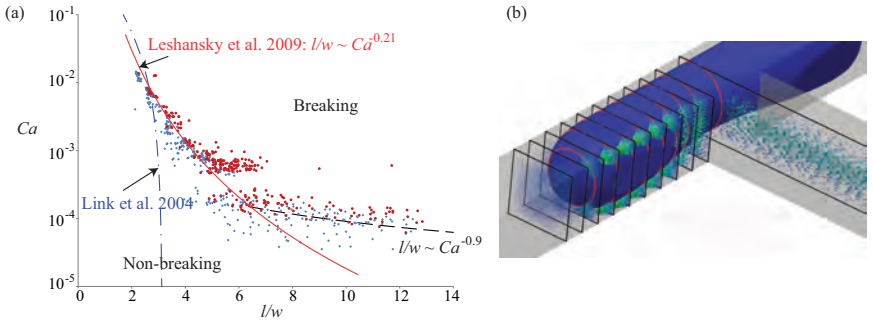

Figure 6.1 (a) Breakup phase diagram of droplets in a T-junction of $h = w = 300\,\mu\text{m}$. The symbols show our preliminary experimental data (red symbols are breaking droplet and blue symbols are non-breaking droplets). The dash-dot line shows the model by Link et al. [11]. The red solid line shows the model by Leshansky and Pismen [14]. The dashed line shows a fitted line $l_0/w \sim Ca_{\text{crit}}^{-0.9}$ to our experimental data for $l_0/w > 6$. (b) Snapshot of droplet shape and the flow passing via the corners of the channel.

discussed below.

An alternative model was proposed by Leshansky and Pismen [14]. They used a 2D model where the Rayleigh-Plateau instability is not operative. Their predicted transition line between breakup and non-breakup takes the form $Ca_{\text{crit}} = a(l/w)^b$, with $b = -1/0.21$. Even though their model cannot fully capture three-dimensional characteristics of the breakup process, it shows good agreement with our experimental data (see figure 6.1(a)) and those by others [12,13] for moderate and high capillary numbers ($10^{-4} < Ca < 10^{-2}$). Jullien et al. [12] argued that two breakup regimes can be distinguished: (a) the "non-obstructed" regime for relatively large Ca corresponding to short droplets ($l/w < 3.5$), and (b) "obstructed" regime for small Ca. The distinction between these two regimes is based on the presence of a *visible* gap between the droplet and the channel walls during the breakup process. For the "non-obstructed" regime, they find good agreement between Leshansky's model and their experimental data, but they claim that Leshansky's model does not hold for the "obstructed" regime. More precisely, Jullien et al. [12] argued based on a 2D topview image that long droplets that seem to fully obstruct the channel always break as the continuous fluid cannot flow around the droplet. This sharply contrast with the model by Leshansky, which predicts a critical Ca for all values of l/w. To support their hypothesis, Jullien et al. [12] performed experiments with two sets of working fluids. Although their result seems to support their claim, there is still no clear evidence that Leshansky's model does not work and the "obstructed" droplets always break. The distinction between the "non-obstructed" and the "obstructed" regime is also questionable, because it is well-known that non-wetting droplets can never fully obstruct the channel with a polygonal cross section [15,16].

Finally, the validity of Leshansky's model at low *Ca* is questionable, because the 2D model by Leshansky ignores the fact that the continuous flow is able to flow around the droplet through the gutters along the corners of the channel as shown in figure 6.1(*b*). As shown in chapter 4, the flow through the gutters increases with decreasing *Ca*. It is hence to be expected that the 2D model by Leshansky and Pismen [14], which does not take into account the gutter flow, can not be applied for the breakup of droplets at low *Ca*. Indeed, our preliminary data shown in the phase map in figure 6.1(*a*) show a significant deviation from the scaling exponent of $b=-1/0.21$ for $Ca<10^{-4}$. Extending Leshansky's model to this new regime or developing a new model is hence an interesting extension of the work presented in this thesis. Care should be taken to incorporate the effect of the viscosity ratio and the aspect ratio of the T-junction to obtain a fully predictive model without fitting constants. Such a model would be highly useful for the flow in porous media, which is typically governed by very low values of *Ca*.

Breakup of droplets in high-aspect-ratio junctions In this thesis, we focussed on droplet breakup in microchannels with an aspect ratio h/w smaller than 1. This choice is motivated by the fact that almost all microchannels used in experimental work have an aspect ratio below unity. Breakup in channels with larger aspect ratios is largely unexplored. Extending the analysis to larger aspect ratios will for instance facilitate a further scale-up of the current bubble-splitting distributor, because scale-up may require the use of junctions with $h/w>1$. Our preliminary simulation on the breakup of droplets in a T-junction with $h/w=2$ shows a change in the breakup behavior. We observed that instead of being squeezed in the direction of the flow as shown in chapters 3 and 4, the droplet interface is squeezed in the direction perpendicular to the flow (see figure 6.2(*a*)). This behavior can be explained by considering the pressure distribution around a droplet which has just fully departed from the feed channel. The pressure drops across the interface along the direction of the flow and perpendicular to the flow are $p_d-p_{out1}=2\gamma/h$ and $p_d-p_{out2}=2\gamma/w$, respectively, where p_d is the pressure inside the droplet and p_{out1} and p_{out2} are pressure at the points depicted in figure 6.2(*b*). The pressure difference $p_{out1}-p_{out2}$ will be $2\gamma(1/w-1/h)$. For $h/w>1$, p_{out1} is larger than p_{out2} such that the the injected flow will go through the side channels and stretches the droplet in the direction of the side channels.

Figure 6.2(*c*) shows the evolution of the two neck thicknesses d/w and d_h/h in time for $h/w=2$ and 0.5. The evolution of d_h/h for $h/w=2$ is qualitatively similar to that of d/w for $h/w=0.5$ in the sense that two phases are observed during breakup: squeezing and rapid pinching. This suggests that the mechanism of droplet breakup in channels with $h/w>1$ might be similar to that in channel with $h/w<1$. Stop-flow simulations, as presented in chapter 3, will be useful to validate this speculation. It is also interesting to address the question why the curves do not collapse and why a larger breakup time is observed in the channels with the largest aspect ratio. Investigating the influence of the high aspect ratio on the breakup phase diagram is another interesting

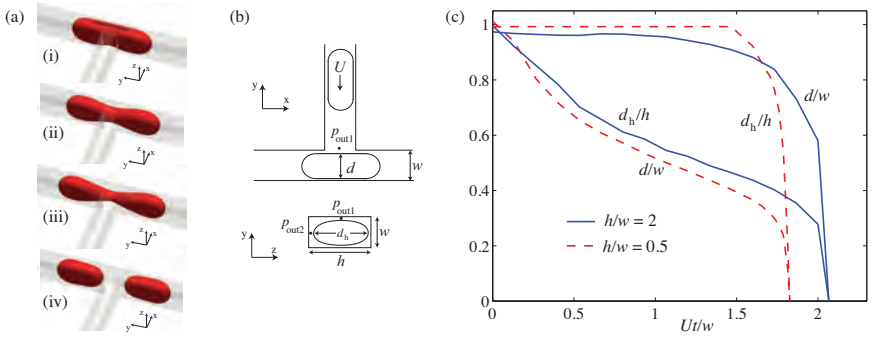

Figure 6.2 (a) Snapshots of droplet shape during the breakup in channel with aspect ration of $h/w=2$. (b) Schematic shape of the droplet fully departed from the feed channel. (c) Plots of d/w and d_h/h versus the breakup time Ut/w for $h/w=2$ (solid line) and 0.5 (dashed line).

question to be resolved.

Self-similar breakup: scaling exponents Eggers and Villermaux [17] reported that the variation of the neck thickness d/w of a droplet in time t in the final stage of the breakup has the form $d/w \sim (t_{break}-t)^{\alpha}$. The exponent α is said to depend on the viscosity ratio λ. For small λ, the exponent α is said to have a value of $1/2$ and the thread is symmetric around the pinching point. For large λ, the exponent α is said to have a value of 1 and the thread is highly asymmetric. In our simulations, however, we have observed that the exponent α tends to 1, and the shape of the thread remains symmetric for all considered viscosity ratios ($0.001<\lambda<10$). The smallest neck sizes that we can resolve with the VOF method are still relatively large such that we might not observe the change of α as well as the final shape of the thread as λ changes. It would be interesting to perform simulations with interface tracking methods such as MMIT to be able to accurately resolve the neck change in the final stage of the breakup. Such results can validate the observation in this thesis and provide a more solid conclusion on the exponent of the pinching rate.

Bibliography

[1] P. Garstecki, M. J. Fuerstman, H. A. Stone, and G. M. Whitesides. Formation of droplets and bubbles in a microfluidic T-junction - scaling and mechanism of break-up. *Lab Chip*, 6:437–446, 2006.

[2] V. van Steijn, C. R. Kleijn, and M. T. Kreutzer. Flows around confined bubbles and their importance in triggering pinch-off. *Phys. Rev. Lett.*, 103:214501, Nov 2009.

[3] B. Dollet, W. van Hoeve, J.-P. Raven, P. Marmottant, and M. Versluis. Role of the channel geometry on the bubble pinch-off in flow-focusing devices. *Phys. Rev. Lett.*, 100:034504, Jan 2008.

[4] W. van Hoeve, B. Dollet, M. Versluis, and D. Lohse. Microbubble formation and pinch-off scaling exponent in flow-focusing devices. *Phys. Fluids*, 23(9):092001, 2011.

[5] A. Carlson, M. Do-Quang, and G. Amberg. Droplet dynamics in a bifurcating channel. *Int. J. Multiphase Flow*, 36(5):397–405, 2010.

[6] D.J.E. Harvie, M.R. Davidson, and M. Rudman. An analysis of parasitic current generation in Volume of Fluid simulations. *Appl. Math. Model.*, 30(10):1056 – 1066, 2006.

[7] M. Sussman and E. G. Puckett. A coupled level set and volume-of-fluid method for computing 3d and axisymmetric incompressible two-phase flows. *J. Comp. Phys.*, 162(2):301 – 337, 2000.

[8] S. Quan, D. P. Schmidt, J. Hua, and J. Lou. A numerical study of the relaxation and breakup of an elongated drop in a viscous liquid. *J. Fluid Mech.*, 640:235–264, 11 2009.

[9] Z. Tukovíc and H. Jasak. A moving mesh finite volume interface tracking method for surface tension dominated interfacial fluid flow. *Comp. Fluid.*, 55(0):70 – 84, 2012.

[10] M. Suo and P. Griffith. Two-phase flow in capillary tubes. *J. Basic Eng.*, 86(3):576–582, 1964.

[11] D. Link, S. Anna, D. Weitz, and H. Stone. Geometrically mediated breakup of drops in microfluidic devices. *Phys. Rev. Lett.*, 92(5), 2004.

[12] M. C. Jullien, M. J. Tsang Mui Ching, C. Cohen, L. Menetrier, and P. Tabeling. Droplet breakup in microfluidic T-junctions at small capillary numbers. *Phys. Fluids*, 21(7):072001, 2009.

[13] T. Fu, M. Youguang, D. Funfschilling, and H. Z. Li. Dynamics of bubble breakup in a microfluidic T-junction divergence. *Chem. Eng. Sci.*, 66:4184ï£¡4195, 2011.

[14] A. M. Leshansky and L. M. Pismen. Breakup of drops in a microfluidic T junction. *Phys. Fluids*, 21 (2):023303, 2009.

[15] H. Wong, C. J. Radke, and S. Morris. The motion of long bubbles in polygonal capillaries. Part 1. Thin films. *J. Fluid Mech.*, 292:71–94, 1995.

[16] V. S. Ajaev and G.M. Homsy. Modeling shapes and dynamics of confined bubbles. *Annu. Rev. Fluid Mech.*, 38(1):277–307, 2006.

[17] J. Eggers and E. Villermaux. Physics of liquid jets. *Rep. Prog. Phys.*, 71(3):036601, 2008.

Appendices

A-1 Derivation of Eqn. 5.2

Consider a stream of n bubbles fed to a single T-junction. These incoming bubbles have a length l_i. The average, standard deviation, and coefficient of variation are calculate according to

$$\bar{l}_{\text{in}} = \frac{1}{n}\sum_{i=1}^{n} l_i \tag{A-1}$$

$$\sigma_{\text{in}} = \sqrt{\frac{1}{n}\sum_{i=1}^{n}\left(l_i - \bar{l}_{\text{in}}\right)^2} \tag{A-2}$$

$$CV_{\text{in}} = \frac{\sigma_{\text{in}}}{\bar{l}_{\text{in}}} \tag{A-3}$$

Suppose that $n-m$ bubbles break symmetrically and m bubbles do not break. We now calculate the average, $\bar{l}_{\text{out}}$, for the $2(n-m)+m$ bubbles leaving the two exits of the T-junction.

$$\begin{aligned}\bar{l}_{\text{out}} &= \frac{1}{2(n-m)+m}\left[\sum_{i=1}^{n-m} l_i/2 + \sum_{i=1}^{n-m} l_i/2 + \sum_{i=1}^{m} l_i\right] \\ &= \frac{1}{2(n-m)+m}\left[\sum_{i=1}^{n} l_i - \sum_{i=1}^{m} l_i + \sum_{i=1}^{m} l_i\right] \\ &= \frac{n}{2(n-m)+m}\bar{l}_{\text{in}}\end{aligned} \tag{A-4}$$

To simplify the writing and the later analysis, we now calculate the square of the

standard deviation, σ^2_{out}, rather than the standard deviation itself

$$\sigma^2_{\text{out}} = \frac{1}{2(n-m)+m}\left[\sum_{i=1}^{n-m}\left(l_i/2-\bar{l}_{\text{out}}\right)^2+\sum_{i=1}^{n-m}\left(l_i/2-\bar{l}_{\text{out}}\right)^2+\sum_{i=1}^{m}\left(l_i-\bar{l}_{\text{out}}\right)^2\right] \tag{A-5}$$

Straightforward manipulation of the math gives

$$\sigma^2_{\text{out}} = \frac{n\bar{l}^2_{\text{in}}}{2n-m}\left[\frac{1}{2}\left(1+CV^2_{\text{in}}\right)+\frac{m}{2n}\left(\left(\frac{\bar{l}_{\text{m}}}{\bar{l}_{\text{in}}}\right)^2+\left(\frac{\sigma_m}{\bar{l}_{\text{in}}}\right)^2\right)-\frac{n}{2n-m}\right] \tag{A-6}$$

with $\bar{l}_{\text{m}}=(1/m)\sum_{i=1}^{m} l_i$ and $\sigma_m=\sqrt{(1/m)\sum_{i=1}^{m}\left(l_i-\bar{l}_{\text{m}}\right)^2}$. For m sufficiently large, $\bar{l}_{\text{m}}=\bar{l}_{\text{in}}$ and $\sigma_m=\sigma_{\text{in}}$. We then find

$$\sigma^2_{\text{out}} = \frac{n\bar{l}^2_{\text{in}}}{2n-m}\left[\frac{1}{2}\left(1+CV^2_{\text{in}}\right)+\frac{m}{2n}\left(1+CV^2_{\text{in}}\right)-\frac{n}{2n-m}\right] \tag{A-7}$$

Using the definition of the breakup fraction $\eta=(n-m)/n$ and the coefficient of variation of the bubbles leaving the two exits further simplification of Eqn. (A-7) yields Eqn. 5.2.

A-2 Derivation of Eqn. 5.4

In the exit arm of height $h-u(h)$, bubbles flow with a velocity $v-u(v)$, have a length $l_b-u(l_b)$, while their distance apart is $l_s-u(l_s)$. This arm contains $n+u(n)$ bubbles and slugs. Using Eqn. 5.3, we find for the pressure drop over this arm

$$\begin{aligned}\Delta p = (n+u(n))\,\frac{12\mu_L\left(l_s-u(l_s)\right)}{1-0.63\frac{h}{w}\left(1-\frac{u(h)}{h}\right)}\frac{1}{h^2}\frac{1}{\left(1-\frac{u(h)}{h}\right)^2}v\left(1-\frac{u(v)}{v}\right)+\\ (n+u(n))\,C\gamma\left(\frac{2}{w}+\frac{2}{h}\frac{1}{1-\frac{u(h)}{h}}\right)(3Ca)^{2/3}\left(1-\frac{u(v)}{v}\right)^{2/3}\end{aligned} \tag{A-8}$$

Similarly, we find for the pressure drop over the arm of height $h+u(h)$

$$\begin{aligned}\Delta p = (n-u(n))\,\frac{12\mu\left(l_s+u(l_s)\right)}{1-0.63\frac{h}{w}\left(1+\frac{u(h)}{h}\right)}\frac{1}{h^2}\frac{1}{\left(1+\frac{u(h)}{h}\right)^2}v\left(1+\frac{u(v)}{v}\right)+\\ (n-u(n))\,C\gamma\left(\frac{2}{w}+\frac{2}{h}\frac{1}{1+\frac{u(h)}{h}}\right)(3Ca)^{2/3}\left(1+\frac{u(v)}{v}\right)^{2/3}\end{aligned} \tag{A-9}$$

Equating the two pressure drops gives

$$\left(1+\frac{u(n)}{n}\right) n\frac{12\mu l_s\left(1-u(l_s)/l_s\right)}{1-0.63\frac{h}{w}\left(1-\frac{u(h)}{h}\right)}\frac{1}{h^2}\frac{1}{\left(1-\frac{u(h)}{h}\right)^2}v\left(1-\frac{u(v)}{v}\right)+$$
$$\left(1+\frac{u(n)}{n}\right) nC\gamma\left(\frac{2}{w}+\frac{2}{h}\frac{1}{1-\frac{u(h)}{h}}\right)(3Ca)^{2/3}\left(1-\frac{u(v)}{v}\right)^{2/3}=$$
$$\left(1-\frac{u(n)}{n}\right) n\frac{12\mu l_s\left(1+u(l_s)/l_s\right)}{1-0.63\frac{h}{w}\left(1+\frac{u(h)}{h}\right)}\frac{1}{h^2}\frac{1}{\left(1+\frac{u(h)}{h}\right)^2}v\left(1+\frac{u(v)}{v}\right)+$$
$$\left(1-\frac{u(n)}{n}\right) nC\gamma\left(\frac{2}{w}+\frac{2}{h}\frac{1}{1+\frac{u(h)}{h}}\right)(3Ca)^{2/3}\left(1+\frac{u(v)}{v}\right)^{2/3} \quad \text{(A-10)}$$

The first and second arm respectively contain $n+u(n)$ and $n-u(n)$ bubble and slugs. Since both arms are of equal length, we find

$$(n+u(n))\left(l_b-u(l_b)+l_s-u(l_s)\right)=(n-u(n))\left(l_b+u(l_b)+l_s+u(l_s)\right) \quad \text{(A-11)}$$

We furthermore use that the bubbles and slugs split according to $(v+u(v))/(v-u(v))=(l_b+u(l_b))/(l_b-u(l_b))=(l_s+u(l_s))/(l_s-u(l_s))$. Using these relations together with Eqn. (A-4), we find the following relation between the inaccuracies

$$\frac{u(n)}{n}=\frac{u(l_s)}{l_s}=\frac{u(l_b)}{l_b}=\frac{u(v)}{v} \quad \text{(A-12)}$$

Using these relations to eliminate $u(n)$ and $u(l_s)$ from Eqn. (A-3) yields

$$n\frac{12\mu l_s}{1-0.63\frac{h}{w}\left(1-\frac{u(h)}{h}\right)}\frac{1}{h^2}\frac{1}{\left(1-\frac{u(h)}{h}\right)^2}v\left(1-\frac{u(v)}{v}\right)\left(1+\frac{u(v)}{v}\right)\left(1-\frac{u(v)}{v}\right)+$$
$$nC\gamma\left(\frac{2}{w}+\frac{2}{h}\frac{1}{1-\frac{u(h)}{h}}\right)(3Ca)^{2/3}\left(1+\frac{u(v)}{v}\right)\left(1-\frac{u(v)}{v}\right)^{2/3}=$$
$$n\frac{12\mu l_s}{1-0.63\frac{h}{w}\left(1+\frac{u(h)}{h}\right)}\frac{1}{h^2}\frac{1}{\left(1+\frac{u(h)}{h}\right)^2}v\left(1+\frac{u(v)}{v}\right)\left(1-\frac{u(v)}{v}\right)\left(1+\frac{u(v)}{v}\right)+$$
$$nC\gamma\left(\frac{2}{w}+\frac{2}{h}\frac{1}{1+\frac{u(h)}{h}}\right)(3Ca)^{2/3}\left(1-\frac{u(v)}{v}\right)\left(1+\frac{u(v)}{v}\right)^{2/3} \quad \text{(A-13)}$$

This equation can be further simplified by linearizing the equation under the assump-

tion that $u(v)/v \ll 1$ and introducing the following constant

$$C_1 = \frac{12}{1-0.63\frac{h}{w}\left[1+\frac{u(h)}{h}\right]}\frac{w^2}{h^2}\left[1+\frac{u(h)}{h}\right]^{-2}$$
$$C_2 = 2C\left(1+\frac{w}{h}\left[1+\frac{u(h)}{h}\right]^{-1}\right)3^{2/3}$$
$$C_3 = \frac{12}{1-0.63\frac{h}{w}\left[1-\frac{u(h)}{h}\right]}\frac{w^2}{h^2}\left[1-\frac{u(h)}{h}\right]^{-2}$$
$$C_4 = 2C\left(1+\frac{w}{h}\left[1-\frac{u(h)}{h}\right]^{-1}\right)3^{2/3}$$

to obtain

$$\frac{l_s}{w}Ca^{1/3}C_3\left(1-\frac{u(v)}{v}\right)+C_4\left(1+\frac{u(v)}{3v}\right)=\frac{l_s}{w}Ca^{1/3}C_1\left(1+\frac{u(v)}{v}\right)+C_2\left(1-\frac{u(v)}{3v}\right) \tag{A-14}$$

Solving for $u(v)/v$ finally yields Eqn. 5.4.

A-3 Derivation of Eqn. 5.5

We first consider a single T-junction to which n bubbles are fed. These incoming bubbles have a length l_i. The average, standard deviation, and coefficient of variation are calculate according to Eqn. (A-1 - A-3).

Suppose that all bubbles break asymmetrically in two daughter droplets, one of length $(1-x)l_i/2$ and the other of length $(1+x)l_i/2$, with $x = u(v)/v$ the relative velocity difference between the two arms. The average, $\bar{l}_{\text{out}}$, of the outgoing $2n$ bubbles of course equals

$$\bar{l}_{\text{out}} = \frac{1}{2n}\left[\sum_{i=1}^{n}(1-x)l_i/2+\sum_{i=1}^{n}(1+x)l_i/2\right] = \frac{\bar{l}_{\text{in}}}{2} \tag{A-15}$$

To simplify the writing and the later analysis, we now calculate the square of the standard deviation, σ^2_{out}, rather than the standard deviation itself

$$\begin{aligned}\sigma_{\text{out}}^2 &= \frac{1}{2n}\left[\sum_{i=1}^{n}\left((1-x)l_i/2-\bar{l}_{\text{in}}/2\right)^2+\sum_{i=1}^{n}\left((1+x)l_i/2-\bar{l}_{\text{in}}/2\right)^2\right]\\ &= \frac{1}{8n}\sum_{i=1}^{n}\left(2l_i^2-4l_i\bar{l}_{\text{in}}+2\bar{l}_{\text{in}}^2+2l_i^2x^2\right)\\ &= \frac{1}{4n}\left[\sum_{i=1}^{n}\left(l_i-\bar{l}_{\text{in}}\right)^2+\sum_{i=1}^{n}l_i^2x^2\right]\\ &= \frac{\sigma_{\text{in}}^2}{4}+\frac{x^2}{4}\frac{1}{n}\sum_{i=1}^{n}l_i^2 \end{aligned} \tag{A-16}$$

Using the standard rule $\frac{1}{n}\sum_{i=1}^{n}a_i^2=\sigma_a^2+\bar{a}^2$, we find

$$\sigma_{\text{out}}^2=\frac{\sigma_{\text{in}}^2}{4}+\frac{x^2}{4}\left(\sigma_{\text{in}}^2+\bar{l}_{\text{in}}^2\right)=\frac{\sigma_{\text{in}}^2}{4}\left(1+x^2\right)+x^2\frac{\bar{l}_{\text{in}}^2}{4} \tag{A-17}$$

We hence find for the coefficient of variation of the outcoming stream of bubbles

$$\begin{aligned}CV_{\text{out}}^2 &= \frac{\sigma_{\text{out}}^2}{\bar{l}_{\text{out}}^2}=\frac{\frac{\sigma_{\text{in}}^2}{4}\left(1+x^2\right)+x^2\frac{\bar{l}_{\text{in}}^2}{4}}{\frac{\bar{l}_{\text{in}}^2}{4}}=CV_{\text{in}}^2\left(1+x^2\right)+x^2\\ &= \left(1+x^2\right)\left(CV_{\text{in}}^2+1\right)-1 \end{aligned} \tag{A-18}$$

Rearranging this expression finally yields for a single T-junction

$$\frac{CV_{\text{out}}^2+1}{CV_{\text{in}}^2+1}=1+x^2 \tag{A-19}$$

For a two-generation device, with a relative velocity difference, x_1, at the first T-junction, and a relative velocity difference, x_2, at the two T-junctions in the second generation, extension of the above analysis is straightforward. For such a device, the coefficient of variation of the bubbles leaving the four exit arms equals

$$\frac{CV_{\text{out}}^2+1}{CV_{\text{in}}^2+1}=\left(1+x_1^2\right)\left(1+x_2^2\right) \tag{A-20}$$

Extending this analysis to a k-generation device yields Eqn. 5.5.

A-4 Derivation of constant in Eqn. 5.6

For a fixed-relative width design, the width of the channels decreases with a factor of $2^{1/2}$ after each subsequent junction. While l_s/w is the same at each junction, the corresponding capillary number decreases according to $Ca_{i+1} = Ca_i w_i/2w_{i+1} = 2^{-1/2} Ca_i$. Hence $(l_{s1}/w_1)Ca_1^{1/3} = (l_{s0}/w_0)Ca_0^{1/3}2^{-1/6}$. Similarly $(l_{s2}/w_2)Ca_2^{1/3} = (l_{s1}/w_1)Ca_1^{1/3}2^{-1/6} = (l_{s0}/w_0)Ca_0^{1/3}2^{-2/3}$. The last generation in our devices forms an exception to this rule, as we did not decrease the width of the exit channels ($w_3 = w_2$). For the last generation, $l_{s3} = l_{s2}w_3/2w_2$ such that $l_{s3}/w_3 = l_{s2}/2w_2 = l_{s0}/2w_0$. Similarly we find for the capillary number $Ca_3 = Ca_2 w_3/2w_2 = Ca_2/2 = Ca_0/4$. Hence, $(l_{s3}/w_3)Ca_3^{1/3} = Ca_i 2^{-5/6}$. This simple analysis shows how we derived the values for α_1, α_2, and α_3 that go into Eqn. 5.6.

A-5 Derivation of Eqn. 5.7

Using Kirchhoff's and refering to Fig. 5.3, the following eight relations can be derived $V_2 = q_l R_l$, $V_3 = q_r R_r$, $V_2 - V_3 = q_b R_b$, $V_1 - V_2 = q_{bl} R_{bl}$, $V_1 - V_3 = q_{br} R_{br}$, $q = q_r + q_l$, $q = q_{bl} + q_{br}$, and $q_{bl} = q_b + q_l$. Solving this set of equations yields

$$\frac{q_{br}}{q_{bl}} = \frac{R_{bl} + R_r \frac{R_b}{R_b + R_l + R_r}}{R_{br} + R_l \frac{R_b}{R_b + R_l + R_r}} \tag{A-21}$$

Using this relation together with the expression for the relative velocity difference $u(v)/v = (q_{br} - q_{bl})/(q_{br} + q_{bl})$ yields Eqn. 5.7.

List of publications

Journal publications

[1] D. A. Hoang, L. M. Portela, C. R. Kleijn, M. T. Kreutzer, and V. van Steijn. Dynamics of droplet breakup in a T-junction. *Journal of Fluid Mechanics*, 717:R4, 2013. doi: 10.1017/jfm.2013.18.

[2] D. A. Hoang, V. van Steijn, L. M. Portela, M. T. Kreutzer, and C. R. Kleijn. Benchmark numerical simulations of segmented two-phase flows in microchannels using the Volume of Fluid method. *Computers & Fluids*, 86:28 – 36, 2013. doi: 10.1016/j.compfluid.2013.06.024.

[3] D. A. Hoang, C. Haringa, L. M. Portela, M. T. Kreutzer, C. R. Kleijn, and V. van Steijn. Design and characterization of bubble-splitting distributor for scaled-out multiphase microreactors. *Chemical Engineering Journal*, Accepted, In press, 2013. doi: 10.1016/j.cej.2013.08.066.

[4] D. A. Hoang, V. van Steijn, L. M. Portela, M. T. Kreutzer, and C. R. Kleijn. Critical behavior of droplet breakup in T-junction microchannel. *Journal of Fluid Mechanics*, In preparation.

Publications in conference proceedings

[1] D. A. Hoang, V. van Steijn, L. M. Portela, M. T. Kreutzer, and C. R. Kleijn. Modeling of low-capillary number segmented flows in microchannels using OpenFOAM. *AIP Conference Proceedings*, 1479(1): 86–89, 2012. doi: 10.1063/1.4756069.

[2] D. A. Hoang, V. van Steijn, L. M. Portela, M. T. Kreutzer, and C. R. Kleijn. On the dynamics of microdroplet breakup in T-junctions. In: Stéphane Colin, Gian Luca Morini and , Jürgen J. Brandner (eds.), *Proceedings of the* 3^{rd} *European Conference on Microfluidics* December 3-5, 2012, Heidelberg, Societé Hydraulique de France, Paris, ISBN 978-2-906831-93-3, Article number 172

[3] D. A. Hoang, V. van Steijn, L. M. Portela, M. T. Kreutzer, and C. R. Kleijn. Numerical studies on the formation of bubbles in T-junction microchannels. 7^{th} *OpenFOAM Workshop*, Darmstadt, Germany, 2012.

[4] D. A. Hoang, V. van Steijn, L. M. Portela, M. T. Kreutzer, and C. R. Kleijn. Breakup dynamics of bubbles/droplets in a microfluidic T-junction. *AIChE Annual Meeting*, Minneapolis, MN, USA, 2011.

[5] D. A. Hoang, V. van Steijn, L. M. Portela, M. T. Kreutzer, and C. R. Kleijn. Numerical study on droplet breakup in a microfluidic T-junction. In C. Spitas (ed.), *Proceedings of the* 22^{nd} *International Symposium on Transport Phenomena*, Delft, Netherlands, ISBN: 9789081820806, Article number 82

[6] D. A. Hoang, V. van Steijn, L. M. Portela, M. T. Kreutzer, and C. R. Kleijn. In: Stéphane Colin and Gian Luca Morini (eds.), *Proceedings of the* 2^{nd} *European Conference on Microfluidics* December 8-10, 2010, Societé Hydraulique de France, ISBN 978-2-906831-85-8, Article number 59

Acknowledgements

Four and a half years for a PhD, many people asked me how could I survive and have sufficient energy to complete such a long journey. It is simply because that I did not do it alone but with the help from many people. Therefore I would like to use this part to thank those who have supported and encouraged me during my PhD.

I have been fortunate to have the opportunity to work with my supervisors, Prof. Chris Kleijn, Prof. Michiel Kreutzer, Dr. Luis Portela and Dr. Volkert van Steijn. We all together built a good team, whose members complemented each other perfectly well. I have always admired their passion and enthusiasm for science and the attitude to be the best of the best. Chris, your support and friendship have been invaluable on both scientific and personal level, for which I am extremely grateful. You have always been a catalyst who ensured everything went fast and smoothly. Michiel has constantly provided insightful and thorough questions that pushed my capability to its border. His great enthusiasm and creativity have motivated me and brought my research to the next level. Luis has brought to our meetings several ideas and his critical attitude has helped improving our work a lot. I will never forget the time we walked back to the Leeghwaterstraat discussing both scientific and personal problems. I also very appreciate Volkert for his scientific advices, and many insightful discussions and suggestions. He has always been available to answer any of my questions. I would like to also thank all members of my committee and all professors in PPE and TP for their scientific advices.

I would like to acknowledge the financial support of STW and IROP for my project. Many thanks to other project partners - Dr. Albert van der Padt from Friesland Campina, Prof. Jaap Schouten, Dr. Xander Nijhuis, Dr. Ma'moun Al-Rawashdeh from TU Eindhoven and Prof. Karin Schroën from Wageningen University - for many fruitful discussions and their continuous interest in my research.

I would like to thank the IT administrators, Erwin de Beus and Peter Bloom, who ensured our computer systems work properly. Amanda van der Vlist and Angela de Ceuninck van Capelle at the Multiscale Physics Department, as well as Anita van

Haren at the Transport Phenomena Group have made my life in the Netherlands much easier with their help in administrative work. Special thanks to Elly Hilkhuijsen at the Product & Process Engineering Group for her support in scheduling my progress meetings. The technical support from Jaap van Raamt and Evert Wagner in setting up my experiments is highly appreciated. I also thank Barbara Kampa and Dr. Pouyan Boukany for their advices in performing the experiments.

During my PhD project, I have worked in two research groups, TP (formerly Multiscale Physics) and PPE, with several great and fun colleagues. Many thanks to them for a pleasureble and lively working environment that motivated me to go to the office every single day in the last four years; this was important especially in the Dutch winter. I had a great time learning how to write a good paper and how to do research properly during group meetings and journal clubs. I will miss all the activities and wonderful BBQs we had together in the last four years. A special thanks to my office mates - Usama Kadri, Anton Gryzlov, Reza Malekzadeh, Galileu de Olivera, Xiaogang Yang, Dries van Nimwegen, Rajat Bhardwaj, Anton Kidess, Bernhard Righolt, Michiel Musterd, Laurens van Campen and Wenjie Jin - for being my second family; I thank them for the jokes, movies, dinners and sport outings we enjoyed together. My special thanks to Michiel Musterd for his help in translating my Summary and Propositions into Dutch and advices in microchip fabrication and cleanroom training. I feel grateful to my students, Frank Lous, Sander Pluimers and Cees Haringa for their extremely useful analytical and experimental data.

I felt grateful to the VCIDs (Vietnamese community in Delft), with whom I can enjoy talking Vietnamese and cooking Vietnamese food; more importantly with them I never felt that I were living too far from Viet Nam. I thank them for all the Lunar New Year parties, oyster-catching trips, football and badminton matches we had together. I would also like to thank people of the Anfieldroad 83, David Boras, Angelina Sánchez, Sumanta Bhattacharya, Inken Wohlers and Thomas Metzler, for all hangovers in the Waterhole and never-ending house parties. We had an amazing trip to the Christmas market in Germany with great Gluehwein and unforgettably moral stories from Sumanta.

A deep gratitude to my mom, dad and sister for their unconditional love and moraleboosting. They were the ones who encouraged me to pursue the PhD and have continuously supported me and have been there for me when times were tough. They have worked and sacrificed so much to ensure that I could completely focus on this book. There are no words to express my love to them and without them I would never have come this far.

Last but not least, uncountable thanks to Quynh Anh, my fiancée, for her constant love, care and stimulation. Four years ago, I met a lovely girl in the Sport Center of TU Delft and she showed me how great the Netherlands is and how cheerful the life here is. From that moment, she has always been with me in any circumstances, has

cooked tons of wonderful food and has warmed up my life in the Dutch winters. Her contribution to this thesis is as much as mine.

Delft, Duong Anh Hoang

Curriculum Vitae

Duong Anh Hoang was born on December 28th, 1983 in Quang Tri, Viet Nam. In 2006, he completed his B.Sc. degree, majoring in Aeronautical Engineering at Ho Chi Minh University of Technology in Viet Nam. He then moved to South Korea to pursue the M.Sc. program in Aeronautical Engineering at Gyeongsang National University. He obtained the M.Sc. degree in 2008, with the thesis focusing on the development of a moving grid code and a FEM solver for rarefied gas flow. From 2009, he started working at the Department of Multiscale Physics, Faculty of Applied Sciences, Delft University of Technology, The Netherlands as a PhD researcher. In his third year, due to the reorganization, he moved to Transport Phenomena group, Department of Chemical Engineering, Delft University of Technology. His research focuses on the breakup, formation and transportation of bubbles and droplets in a network of microchannels.